STIMULI-RESPONSIVE VALVING MECHANISMS FOR PAPER-BASED DIAGNOSTICS

by

Elizabeth Anne Phillips

A Dissertation

Submitted to the Faculty of Purdue University

In Partial Fulfillment of the Requirements for the degree of

Doctor of Philosophy
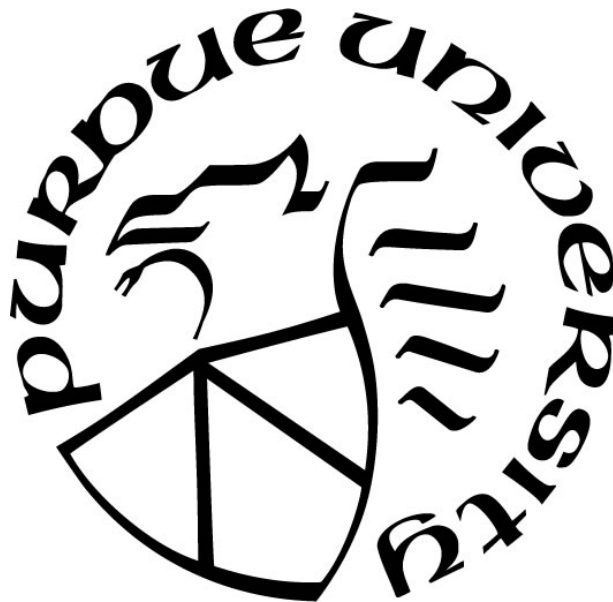
Weldon School of Biomedical Engineering

West Lafayette, Indiana

May 2020

.

THE PURDUE UNIVERSITY GRADUATE SCHOOL
STATEMENT OF COMMITTEE APPROVAL

Dr. Jacqueline Linnes, Chair

Weldon School of Biomedical Engineering

Dr. Ramses Martinez

Weldon School of Biomedical Engineering

Dr. Kevin Nichols

Intellectual Ventures

Dr. Luis Solorio

Weldon School of Biomedical Engineering

Approved by:

Dr. George Wodicka

Dedicated to my parents for their unwavering support and encouragement

ACKNOWLEDGMENTS

This document is the result of years of support and guidance by many wonderful people. First and foremost, I want to thank my advisor, Dr. Jacqueline Linnes, for the opportunity to join her lab. Jackie has an infectious curiosity and enthusiasm for science that makes even a frustrating day in the lab feel like an accomplishment. She led by example, teaching me how to set realistic goals and not be discouraged by the inevitable challenges I would encounter during my PhD. She gave me the freedom to explore my research, professional, and personal interests. I am continually inspired by her desire and ability to positively impact the world and am thankful to have her as a mentor throughout my career.

Thank you to my thesis committee members, Dr. Ramses Martinez, Dr. Luis Solorio, and Dr. Kevin Nichols. Dr. Ramses Martinez challenged me to consider the real-world implications of my research approaches and connected me with resources in his lab to better characterize paper fluidics. Dr. Luis Solorio always had an open door and was eager to brainstorm alternative directions in my responsive hydrogel research. Dr. Kevin Nichols was immediately open to mentoring me from across the country, encouraged me to rigorously validate my results, and frequently pointed me towards research and professional resources.

I am also grateful for Kevin's invitation to intern at Global Good where I also met Dr. Samantha Byrnes. Their mentorship motivated me to explore non-academic settings to continue diagnostics research and development. I very much appreciate the opportunity to collaborate with Dr. Andrew Ellington and Dr. Sanchita Bhadra of UT Austin to more specifically capture nucleic acids. Thanks also to Dr. Hadley Sikes of MIT for encouraging me to always have both short and long-term projects in my research pipeline and for cheering on my career development from afar.

I would like to acknowledge all of the faculty and staff at Purdue who have supported me. Dr. Tamara Kinzer-Ursem eagerly guided my experimental methods when I was troubleshooting polymerization and conjugation methods and cultivated my long-term research aspirations. I have valued Dr. Kaisa Ejendal's example as a meticulous, grounded, and cheerful scientist who can bounce effortlessly between conversations about DNA amplification and baking. I hope I can always work alongside someone with such optimism and impeccable fashion taste. Tammy Siemers worked tirelessly to coordinate industry trips to Seattle and Boston, professional development seminars and workshops, and individual career development milestones, for which I

am very grateful. Similarly, Sandy May, Jo Gelfand, Kitty Cooper, Pamela Lamb, Linda Doyle, and Carla Brady are the bedrocks of the Weldon School and I am thankful for their frequent support in all academic and department matters. Outside of our department, I would like to acknowledge Sean of the Purdue Writing Lab, for showing me how to do a reverse outline and critically evaluate my writing. And I am thankful for the Office of Technology Commercialization for teaching me about intellectual property and filing patent applications.

For my first and last year at Purdue, I was financially supported by the Shah Family Global Innovation Lab to do research and to meet with our collaborator, Dr. Fabian Esamai in Kenya. The Lab also supported my involvement with a community of globally minded researchers through travel grants and symposiums. I am also grateful to the travel support and life sciences community fostered by PI4D. Thanks to additional travel grants from the Graduate Student Government, the College of Engineering, Joe Bourland, and the Women's Initiative Committee of AIChE, I was able to attend scientific conferences in Italy, Taiwan, and Pittsburgh. I am also incredibly grateful for three years of financial support from the NSF Graduate Research Fellowship.

I never expected my labmates to become my roommates, neighbors, and lifelong friends. So, thank you to all of the members of the Linnes Lab for their collaboration, humor, and moral support, especially Taylor, Divya, Orlando, Kay, Emilie, Ashlee, Laud Anthony, Somayeh, and Mindy. May the newest lab members always appreciate your feedback, friendship, and lab snacks. I also had the privilege of mentoring several undergraduates, including Emilie, Tori, Greg, Siyu, and Laura. I am especially grateful to my roommates, Kay and Carmen, who exemplify resilience and never failed to brighten my Wednesday night with roomie-dinner. And I am thankful to have such truly wonderful friends as Taylor, Divya, Andrea, and Rachel who were always game for a weekend away or a Sunday potluck brunch. Thank you to my cat, Henrietta, for keeping my lap and keyboard warm while I wrote this and many other documents. I credit all typos to her.

Thank you to my parents, Lisa and Dan Phillips, my sister, Emily Phillips, my grandparents, Carol and Guy McGiboney, and all of my extended family. They instilled in me a perseverance to understand the world around me and a confidence that I have their love and support wherever I end up. I always try to make them proud.

Finally, thank you to my husband, Dr. Matt Pharris, for keeping an open seat next to him on the first day of orientation and loving me ever since. He never fails to put a smile on my face, and I am forever grateful to have him as my partner in life.

TABLE OF CONTENTS

LIST OF TABLES

LIST OF FIGURES

LIST OF ABBREVIATIONS

CHA	catalytic hairpin assembly
Chr1	chromatography paper
dsDNA	double stranded DNA
dSLR	digital single lens reflex
FAM	6-carboxyfluorescein
hCG	human chorionic gonadotropin hormone
HLB	hydrophilic-lipophilic balance
IR	infrared
LAMP	loop mediated isothermal amplification
LFIA	lateral flow immunoassay
LNA	locked nucleic acid
MB	methylene blue
microRAAD	microfluidic rapid and autonomous analysis device
µPAD	microfluidic paper analytical device
NAA	nucleic acid analogue
NALF	nucleic acid lateral flow assay
NC	nitrocellulose
PDMS	polydimethylsiloxane
PEG	polyethylene glycol
PES	polyether sulfone
PIV	particle image velocimetry
POCT	point-of-care testing
RT-LAMP	reverse transcription combined with LAMP
SC	succinimidyl carbonate (NHS ester)
SD-LAMP	strand displacement combined with LAMP
SEM	scanning electron microscope
ssDNA	single stranded DNA
TE	Tris-EDTA buffer
TBE	Tris/Borate/EDTA buffer
TEMED	tetramethylethylenediamine

ABSTRACT

Rapid identification of disease-causing pathogens at the point-of-care enables immediate treatment and infection control. However, existing rapid diagnostic devices fail to detect the low concentrations of pathogens present in the early stages of infection, causing delayed and even incorrect treatment. A delay in antibiotic treatment of as few as 24 hours after infection onset will drastically decrease a patient's chance of survival. The transport of a patient's sample to a centralized testing laboratory can contribute hours to this delay. For instance, the most sensitive assay, nucleic acid detection, can only be performed at centralized laboratories. The multistep sample preparation and costly instrumentation required to analyze samples has prohibited nucleic acid detection assays from reaching the point-of-care. There remains a critical need to bring rapid and sensitive pathogen identification technologies out of the laboratory to ensure effective treatment.

Paper-based devices have emerged as a portable platform for nucleic acid detection but are limited by their imperfect control of reagent incubation and false positive results. Here, I have developed mechanisms to specifically and automatically detect the nucleic acids of pathogens on paper-based devices. First, I characterize wax-ink valves that enable controlled incubation and delivery of reagents through device stages. Next, I implement toe-hold mediated strand displacement reactions to increase the specificity of nucleic acid detection with paper-based devices. Lastly, I functionalize polymers with nucleic acid probes and explore their potential integration into paper-based devices as bio-responsive valves. I demonstrate how such novel valving mechanisms enable the automatic and multi-step analysis of bacteria and viruses on paper-based platforms, improving the detection of infectious diseases at patients' point-of-care.

1. INTRODUCTION

1.1. Need for point-of-care diagnostics

1.1.1. Global infectious disease burden

Despite tremendous advances in healthcare and medication availability, treatable infectious diseases remain a substantial burden in developing countries. Over half of deaths in low-income regions are caused by preventable conditions like infectious diseases, nutritional deficiencies, and maternal and childbirth complications. While such conditions cause less than 7% of deaths in high-income countries,[1] the financial toll of infectious disease should not go unnoticed. Among all disease categories, the cost of treating infectious diseases has increased the most in the United States during the 2000s.[2] In low-income countries, the financial burden is deadly.

Lacking modern diagnostic laboratories with consistent electrical services, running water, and trained personnel, healthcare providers in low-resource settings treat based largely on clinical observations.[3] Infectious diseases can cause very non-specific symptoms making it difficult for providers to identify the cause of an illness and provide evidence-based treatment. Early identification of a disease-causing pathogen is critical to providing appropriate treatment and improving patients' outcomes.[4]

1.1.2. Biomarkers of infectious diseases

Biomarkers enable the identification of infectious diseases and can inform the efficacy of therapies. While any physiological measurement that predicts a patients' disease state can be considered a biomarker, the most effective biomarkers are present in patient samples collected with minimal invasion (e.g. capillary blood and urine) and have been clinically validated to provide specific and sensitive diagnostic results. A vast variety of small molecules including proteins, peptides, carbohydrates, metabolites, exosomes, and nucleic acids have been classified in databases and reviewed elsewhere for their clinical utility.[5,6] Proteins, such as pathogens' surface antigens and immune response antibodies, are among the most commonly detected biomarkers for diagnosing infectious diseases. However, low prevalence of protein-based biomarkers, particularly in early stages of infection, can cause false-negative detection results.[7] To provide more reliable

early detection, other biomarkers have been increasingly explored for clinical utility. Pathogens' nucleic acids are one such biomarker that have been shown to provide early identification of an infecting pathogen, largely due to our ability to amplify them to detectable levels through polymerase chain reactions or isothermal amplification techniques. Furthermore, analysis of nucleic acids can indicate treatment resistance and provide invaluable epidemiology insight to inform outbreak control.[8]

1.2. Existing point-of-care diagnostics for infectious diseases

1.2.1. Commercially available platforms

Clinical detection of infectious disease biomarkers can be performed by benchtop assays, commonly in a central testing laboratory, or at a patient's bed-side and point-of-care. In contrast to the multi-day turnaround time for central laboratory testing, point-of-care testing (POCT) permits diseases to be diagnosed and monitored at the bed-side for immediate clinical management. Often small and simple in appearance, POCT devices intricately integrate sophisticated biochemical, microfluidic, and electrical technology. Coincident advances in biochemical understanding, microelectronics, and manufacturing processes during the mid- and late-1900s facilitated the miniaturization and portability of disease detection assays. One of the first commercially successful devices to miniaturize clinical chemistry blood assays, the handheld iSTAT (Abbott), is now found in more than a third of US hospitals.[9] Cepheid is currently launching its GeneXpert Omni to deliver rapid molecular diagnostics to the point-of-care. Due to their utility and resource saving potential, molecular POCT devices drove a $4 billion market in 2011 increasing to $7 billion by 2015, with infectious disease testing growing the fastest.[10]

In-use POCT devices can be largely categorized into 1) hand-held devices requiring disposable cartridges like the iSTAT or Epoc critical care testing systems and 2) disposable test strips like rapid pregnancy or strep tests and blood glucose strips. Many of these strip tests are accompanied by a re-usable digital reader to perform photometric analysis of test band intensity or to perform electrochemical detection. Most of these devices have been reviewed elsewhere for their clinical utility.[10,11] Notably, most existing POCT devices are based on technology developed decades ago and have only improved incrementally to yield greater sensitivity, usability, or target versatility. Several of these device platforms, particularly rapid pregnancy tests and blood glucose

sensors, have been modified for detection of infectious disease biomarkers. But, POCT devices with fundamentally different detection mechanisms have rarely transitioned from research and development labs into the market.

1.2.2. Emerging platforms

Fabrication techniques that enabled miniaturization of electronics coincidentally enabled miniaturization of laboratory instrumentation and assays. Combined with advancements in biochemical detection methods, a multitude of lab-on-chip assays have been developed for rapid POCT including immunoassays,[12,13] enzyme assays,[14] nucleic acid amplification and detection,[15–18] and whole cell analysis.[19,20] While these microfluidic devices non-invasively analyze small volume samples, their global usage, particularly in low-resource settings, has been hindered by expensive instrumentation requirements and high costs of consumable assay cartridges.[21]

Similarly capable of analyzing small volume samples are emerging paper fluidic or analytical devices. In contrast to lab-on-chip devices, large-scale manufacturing using roll-to-roll and converting processes permits paper fluidic diagnostics' low cost.[22] Furthermore, many paper fluidic devices utilize a visible signal transduction mechanism for instrument-free detection. As will be discussed in more detail in **Section 1.2.3**, emerging paper fluidic devices differentiate themselves from the existing dipstick and lateral flow immunoassays (i.e. rapid pregnancy tests) by utilizing advanced fluidic control mechanisms and alternative target capture mechanisms to enable more sensitive detection. Furthermore, several sample-to-answer (also referred to as "integrated") paper fluidic devices have been reported that streamline the bedside detection of nucleic acids from infectious pathogens such as influenza A,[23,24] *Salmonella typhimurium,*[25] and *Staphylococcus aureus.*[26] While no paper fluidic devices have reached commercialization, a recent market review predicts that paper diagnostics will reach an $8.35 billion market size by 2022 given increasing R&D and medical market demand.[27]

1.2.3. Paper as a low-cost diagnostic assay substrate

Paper has been an attractive substrate for biological and chemical assays for centuries given its low cost, ease of fabrication, stability, and hydrophilic functionality. A matrix of fibers or polymers, paper's well-defined pore structure enables capillary driven liquid transport without the

need for external, costly instrumentation. Paper chromatography in the late 1800s demonstrated paper's utility as a chemical assay substrate but its usage as a biological substrate (i.e. nitrocellulose membrane in protein and nucleic acid blotting assays) in the 1950s was instrumental for its translation into medical technology. First commercialized in the 1980s' rapid pregnancy test lateral flow immunoassay (LFIA), impregnation of enzymes and capture molecules into multiple porous membranes most advanced paper as a POCT substrate.

1.2.4. Principles of paper fluidic diagnostics

As with all biosensor platforms, paper fluidic diagnostics contain components to accomplish three tasks: 1) fluid transport, 2) bio-recognition, and 3) signal transduction. The following three sections discuss these components in the context of paper fluidics for nucleic acid detection, relevant to this thesis, but it is helpful to understand how these are performed in the most common of paper fluidic devices, the LFIA. LFIAs typically consist of four consecutively overlapping papers and membranes impregnated with assay reagents (Figure 1.1). Despite their apparent simplicity, LFIAs require significant material engineering of the substrate, additives, detection labels, and capture molecules. A low volume liquid sample (tens to low-hundreds of microliters) is applied to the sample region of the strip and wicks through the device, delivering a result within 10-30 minutes. Upon wetting the sample pad, embedded surfactant and protein is rehydrated into the sample to facilitate downstream wetting and assay blocking. Capillary forces expel the liquid into the second pad, the conjugate pad, pretreated with reporter conjugated labels such as visible gold nanoparticles, fluorescent dyes, or enzymes. Rehydrated, the reporter conjugates will bind to its target biomarker present in the sample. The mobile phase continues wicking through the third pad, a test membrane, containing immobilized lines of capture molecules, such as antibodies. The test line binds preferentially to the sample's biomarker to sandwich the biomarker with the reporter at the test line, detectable by the visible, fluorescent, or electrochemical accumulation of nanoparticles. Immediately downstream of the test line a positive control line of capture molecules bind excess reporter conjugate and confirm successful passage of rehydrated conjugates through the test region. Finally, the most hydrophilic paper composes the fourth pad and serves to absorb the entire mobile phase. Typically complete in 10-30 minutes, a user easily interprets the assay results by counting the number of lines of accumulated nanoparticles where 1 or 2 lines constitute a negative or positive result respectively.[28,29]

19
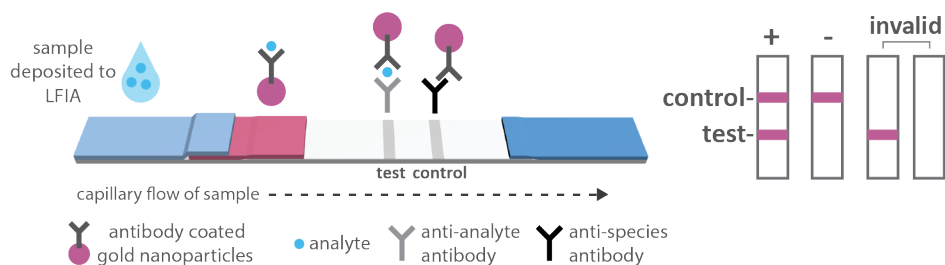
Figure 1.1 Typical lateral flow immunoassay platform and readout.

Several literature reviews detail the progress and limitations of LFIAs pertaining to paper composition and additives, capture molecules, the multiplexed detection of several disease biomarkers, and signal amplification.[30] While LFIAs typically provide a qualitative output of analyte presence, semi-quantitative outputs have been achieved by assessing test band intensity[31] (usually with instrumentation) and by engineering consecutive test bands to capture an increasing fraction of analyte (for instrument-free quantitation).[32] Most limiting to LFIA clinical impact is insensitivity for many biomarkers, particularly nucleic acids, that can only be overcome by pre-amplification steps that require additional sample preparation. For instance, nucleic acid lateral flow (NALF) assays more sensitively detect biomarkers by amplifying nucleic acids prior to lateral flow detection, but can be adversely affected by cellular contaminants like red blood cells and non-specific amplification products. To minimize user involvement, pre-amplification and sample preparation steps have been integrated into paper substrates, transforming LFIAs into more general paper fluidic platforms.

1.2.5. Flow control in paper fluidics

Translation of molecular diagnostics assays, such as sample filtration and nucleic acid amplification, onto paper fluidic platforms requires controlled delivery of fluids and reagents through reaction zones to satisfy necessary binding kinetics. Mechanisms to direct and redirect fluid flow have been a primary research focus for the past ten years.[33–36] Also referred to as microfluidic paper-based analytical devices (μPADs), paper-fluidics have improved, but not yet achieved, the precisely timed delivery of liquids that is characteristic of lab-on-chip assays.

Paper-fluidic devices will only be an appropriate alternative to their greatest competitor, lab-on-chip assay platforms, when greater fluidic control can be achieved within the membranes. The sophisticated fluid transport including mixing, separating, and timed delivery of liquids performed

20

in lab-on-chip devices can be achieved by incorporating three fundamental elements: pumps, routers, and valves. Rather than actively pump fluid through open channels, paper-fluidic devices leverage the inherent wicking ability of porous materials to transport fluid through multiple reagent zones. By eliminating the external pumping mechanism that microfluidic devices typically require, paper-fluidic devices are a much more portable alternative. Routers directing flow through channels can be defined by hydrophobic barriers made from polydimethylsiloxane (PDMS), tape, and/or wax-ink.[37–39] Valves that obstruct and control the release of fluid remain the most challenging element to incorporate into paper-based devices.[30,40] (Detailed discussion in **Chapter 2**)

With improved valving mechanisms, more sophisticated, multi-step bioassays can be integrated into paper fluidic devices. Nucleic acid amplification is one such assay that, with integration into paper fluidic devices, would greatly improve the detection sensitivity of infectious pathogens.

1.2.6. Nucleic acid detection on paper

Several reviews highlight recent advancements in facilitating nucleic acid detection on paper substrates.[41,42] Most popular among these advancements is to integrate nucleic acid amplification with down-stream LFIAs. A variety of capture methods exist depending on whether the amplicon is single-stranded(ss) or double-stranded(ds).[43] SS-amplicon can be directly captured by oligonucleotides immobilized onto the test strip but requires significant optimization of the probe immobilization strategy and hybridization kinetics so are not common.[44,45] Alternatively, ss-amplicon is often hybridized after amplification to a biotin, BSA, or hapten[46] labeled capture probe and a reporter probe labeled with visualization nanoparticles, but often requires an additional heating step for probe hybridization. The hybridized product can then be captured by an anti-label antibody on the LFIA. Similarly, labeled primers can incorporate a biotin and a second label, such as fluorescein isothiocyanate, into ds-amplicon or ss-amplicon. The labeled amplicon is subsequently captured by an anti-label antibody and an avidin coated nanoparticle completes the sandwich for visualization.

While many previously published methods demonstrate amplicon detection by labeling primers for capture on a low-cost LFIA they risk capture of primer dimers and spurious amplicons.[24,47,48] The false positive results endemic to these non-specific signal transduction

methods are typically mitigated by redesigning the primer sets or reducing reaction time, which also decreases assay sensitivity. Alternatively, target specific detection of nucleic acid amplicons can be achieved with hybridization of incorporated primers,[49] polymerase-mediated strand displacement of duplexed primers,[50] or toehold-mediated strand displacement events,[51] but all have required an excited fluorophore and fluorescent reader for signal transduction. Du et al. alleviated the need for a lab-based fluorescent reader by coupling target-specific strand exchange reactions to a home-pregnancy test, an inexpensive and ubiquitous LFIA strip, for visual detection.[52] However, multiple additional user steps and reagents to complete this signal transduction complicated the detection and could increase interpretation error.

Strand exchange reactions, also known as strand displacement reactions, remain an underexplored mechanism for specific capture of nucleic acid amplification products. Instrumental to specific capture are short complementary single-stranded domain 'toeholds' that initiate strand displacement and branch migration reactions. Scida et al. demonstrated the detection of DNA by competitively hybridizing ssDNA analyte and quencher-labeled ssDNA to a fluorophore-labeled ssDNA probe on a flow-through μPAD.[53] A solution of ssDNA analyte wicked through chromatography paper layers with wax-defined reservoirs of pre-dried quencher and fluorophore-labeled ssDNA. A toehold extension on the fluorophore-labeled ssDNA allowed the ssDNA analyte to outcompete and displace any quencher-labeled ssDNA, detectable by fluorescent intensity.[53] Allen et al. improved the quantitative detection of DNA utilizing a similar strand displacement mechanism but in a lateral wicking format on paper.[54] To amplify the fluorescent signal, Allen et al. combined the toehold mechanism with a catalytic hairpin assembly (CHA) mechanism previously developed by Yin and Pierce.[55] In CHA mechanisms, two partially complementary DNA hairpins are kinetically unable to hybridize until a catalyzing ssDNA binds to one hairpin's toehold extension, causing hairpin unfolding and interaction. In Allen et al.'s device, the analyte ssDNA catalyzed hairpin hybridizations; the signal of one analyte ssDNA amplified to many hairpin complexes that outcompeted quencher-labeled ssDNA binding to fluorophore-labeled ssDNA. The CHA mechanism enabled a three-fold greater fluorescent signal equitable to a limit of detection on the order of hundreds of nanomolar, still too low for clinical impact.

As described in Chin et al., the paucity of nucleic acids in clinical samples necessitates their amplification for ultimate detection.[11] Allen et al. achieved sensitive detection by amplifying

ssDNA by LAMP and using the loop shaped amplicons to open a synthetic hairpin DNA that serves as the previously described CHA catalyst.[54] Problematically, the number of binding interactions and complimentary sequences to be optimized complicates the application of this to other DNA targets. The Collins group has similarly utilized hairpins with toehold extensions for rapid detection of Zika and Ebola virus RNA on paper substrates with an initial RNA amplification step.[56,57] Instead of catalyzing hairpin assembly, analyte RNA binds to the toehold and opens an RNA hairpin coined a toehold switch. Ensconced in the RNA hairpin is a ribosome binding site and start codon for downstream regulation of LacZ enzyme; opening of the hairpin by the target RNA activates gene regulation and is visualized on paper by the conversion of a yellow substrate to a purple product. Most limiting to the Collins' clinical impact is the need to isolate target RNA from sample contaminates and the 3 hour diagnostic test incubation period which prevents it from informing bedside clinical management decisions. Nevertheless, a combination of nucleic acid amplification and strand displacement specificity is a promising mechanism to detect pathogens on paper fluidic platforms.

1.2.7. Signal transduction in paper assays

Traditional paper-based detection mechanisms rely on colorimetric, fluorescent and electrochemical changes. While often more sensitive, fluorescent and electrochemical transduction methods require accompanying electronic readers that increase the cost of the diagnostic and the complexity of use. Colorimetric, such as by the accumulation of gold or latex nanoparticles in LFIA, is the preferred method for point-of-care applications because it does not require additional detection instrumentation. Elain Fu and Lathwal *et al*. have reviewed a number of different equipment-free, colorimetric detection mechanisms on paper-based assays.[58,59] Notably, the traditional colorimetric readout, hue, is one of the most challenging visible changes to discern which causes many colorimetric tests to be difficult to interpret.[60] Many researchers have shifted from intensity and hue-based readouts to distance-based readouts such as the Henry group's metal[61] and glucose[62] sensors and the Yang group's hydrogel integrated glucose sensors.[63] Tian et al has more comprehensively reviewed distance-based POCT devices and highlights the potential of such devices to provide an instrument-free, quantitative readout by correlating flow distance to sample concentration.[64] Quantitative readouts would greatly improve disease management by informing disease progression and the efficacy of therapy.[65] Unfortunately, most

existing distance-based methods require excessive reagents (i.e. the entire paper strip is coated with capture molecules or enzyme) and increase the ultimate cost of the device.

1.2.8. Signal transduction mediated by flow control

Combining paper fluidic components' functionality can potentially reduce overall device cost and complexity. Distance-based signal transduction is one such mechanism that can combine transport with biorecognition. For instance, Tian et al. reported a paper analytical device in which the biorecognition molecule (an aptamer) is bound to an invertase-DNA conjugate reporter molecule and sepharose beads physically trapped in pores.[66] Binding of the target to the aptamer triggers the release and flow of the reporter through the pores to a downstream detection strip. Like many distance-based methods, however, this mechanism requires the downstream strip to be coated with enzymes and substrate for color development.

Several distance-based detection mechanisms have been reported that do not require modification or pre-treatment of the downstream detection strip. For instance, Wang et al. leveraged the unique interfacial interaction of SYBR Green dye with cellulose paper when the dye is intercalated into varying concentrations of dsDNA amplification product.[67] As discussed previously though, the need for a fluorescent reader may outweigh the quantitative output provided by this mechanism. Visually detectable is Roy et al's magnetic bead aggregation system; in the presence of long strands of dsDNA magnetic particles aggregate in the pores of paper yielding a visible, albeit qualitative, spot.[68] A visually detectable and quantifiable flow regulator has been reported by Wei et al which leverages target-responsive DNA hydrogels to detect varying aptamer binding targets.[69] Sample is applied to a vertical flow device containing layers of papers pre-treated with DNA-hydrogel components. In the absence of the target, the aptamer crosslinks the hydrogel, preventing liquid and reporter dye from flowing into a detection strip. In the presence of the target, the target preferentially binds to the aptamer, prevents hydrogel formation, and permits migration of the dye into the detection strip. While they demonstrated successful detection of several small molecules (i.e. cocaine, adenosine, and lead), there remains an opportunity to explore such combined biorecognition and flow modulation techniques for pathogen detection.

1.3. Thesis overview: characterization of stimuli-responsive valving mechanisms

Low sensitivity to infectious disease biomarkers continues to plague existing point-of-care devices, leading to false negative results and delayed treatment. The Linnes Lab has recognized nucleic acids as viable biomarkers of early infection because they can be rapidly amplified from low concentrations for detection.[70] The implementation of nucleic acid amplification assays outside of laboratories requires minimizing user steps. As discussed in **1.2.2 Emerging platforms**, significant efforts are being made toward developing sample-to-answer paper fluidic devices that streamline sample preparation steps like nucleic acid pre-amplification. Most challenging to these devices has been the ability to constrain the sample to isolated regions of the device for sustained reaction times. As discussed in **1.2.5 Flow control in paper fluidics**, existing valving mechanisms are either unable to restrict flow for sufficient amplification time, cause irregular flow past the opened valve, and/or require additives that could hinder nucleic acid amplification reactions. Since a nucleic acid amplification assay would require a heating source, I proposed using a heating source to actuate valves composed of wax-ink, a material commonly used to define hydrophobic barriers in paper fluidic devices.[71] In **Chapter 2**, I characterize the wax-ink valves printed into varying paper fluidic membranes by their heating requirements, actuation time, and fluid release and identify tuning parameters for their incorporation into paper fluidic devices. In **Chapter 3**, I describe a multiphysics model of the wax-ink valves to explore sources of heat loss that cause non-uniform melting of the wax-ink valves. In **Chapter 4**, I implement wax-ink valves into an existing LFIA and in a lab-developed sample-to-answer nucleic acid detection device.

Isothermal nucleic acid amplification methods such as loop-mediated isothermal amplification (LAMP) can efficiently amplify targets at a single temperature from even complex patient[72,73] and environmental sample matrices,[74] alleviating the need for expensive thermocycling equipment typically required for amplification. Despite minimal instrumentation required to amplify a pathogenic gene target via LAMP, additional instrumentation is typically required to both sensitively and specifically visualize amplicons which limits the usage of LAMP outside of a laboratory. The conventional, low-cost visualization strategy of LAMP amplification products is to tag two of the six primers for post-amplification capture on a LFIA. However, I and other researchers have observed false positive LFIA results that can only be resolved by time-consuming primer redesign. I proposed that the specificity of toe-hold mediated strand displacement reactions be leveraged to more specifically tag amplification targets and minimize the capture of primer

dimers and spurious amplification products. Replacing one of the tagged loop primers with a strand displacement probe has been demonstrated by the Ellington Lab at University of Texas at Austin to improve specific, fluorescent detection of LAMP products.[51] In **Chapter 5**, I describe the results of collaborating with the Ellington Lab to design strand displacement probes for improved detection of bacterial pathogens on LFIAs and tested the reaction performance in the presence of human and environmental sample simulants. This more specific strategy eases the development of amplification assays for translation outside of laboratories by reducing the re-design time of primer sets.

Lastly, I proposed creating a bio-responsive valve that combines the nucleic acid specificity achieved by strand displacement reactions with the flow control achieved with printed valves. Several groups have demonstrated that DNA-hybrid hydrogels can be crosslinked by DNA-functionalized acrylamide and dissolved by toehold mediated strand displacement with a target DNA strand.[63,69,75–77] Furthermore, Yang et al. have demonstrated that such hydrogel formation can be utilized to provide a distance-based readout of the DNA target's concentration.[69] However, this hydrogel system has not been created in a format conducive to roll-to-roll manufacturing scale-up nor has it been tested with DNA targets in a paper substrate. In **Chapter 6**, I describe strategies for embedding DNA-hybrid hydrogels into test strips to function as bio-responsive valves. I character the valve's composition, response kinetics, and fluid release in a paper substrate to detect nucleic acid targets in a paper fluidic device. These studies provide a framework for more specifically detecting infectious pathogens outside of the laboratory on low-cost and instrument-free paper-fluidic diagnostic devices.

2. CHARACTERIZATION OF FLUID FLOW THROUGH THERMALLY ACTUATED WAX VALVES PRINTED INTO POROUS MEMBRANES

Parts of this chapter are reproduced from Ref. 78 with permission from the Royal Society of Chemistry.

2.1. Rationale

The complexity of current paper-fluidic diagnostic devices is limited by their imperfect control of reagent incubation and delivery. Valves providing complete fluid obstruction and multiple actuation steps within a single paper-fluidic diagnostic would increase the range of diagnostic bioassays in these porous membranes. In this chapter, I explore the utility of wax-ink, a common material that has been used to define hydrophobic barriers in paper-fluidic diagnostics,[38] to both obstruct and control the release of fluid in porous membranes.

Valves enabling the precise and appropriately timed delivery of fluid are key to performing multistep assays on paper fluidic devices. The simplest way to vary the flow rate and delivery time of reagents is to control the geometry of the channels such as their length and width.[40,79,80] A second way to alter flow rate is to add additional material to the paper channel. Printer toner that typically obstructs fluid flow can be laser printed with lower density to permit fluid passage at slower flow rates.[81] Similarly, the addition of paraffin wax of varying quantity has been used to create internal device 'timers'.[82] The addition of highly resistive cellulose-based shunts[83] and dissolvable sucrose and pullulan film barriers,[84–86] also permit a slow, controlled release of fluid. Pre-embedded surfactants have been used to accelerate the flow of liquid through pores and thus enable sequential flow of liquids with delay and trigger valves.[87] However, these dissolvable materials can potentially affect downstream assay performance though and have not yet been applied to many bioassays.[86] While the previous mechanisms to accelerate and decelerate the flow of liquid can potentially enable multistep bioassays, few fluidic valve mechanisms exist that can fully obstruct the flow of liquid until its desired release.

A valve mechanism that completely obstructs fluid flow for a sustained amount of time and requires minimal user involvement has been difficult to engineer thus far. A compressed sponge actuator exists that completely stops liquid passage but is user actuated by additional fluid to expand the sponge.[40] A magnetic valve exists that fully obstructs reagent flow, but is limited to a maximum of approximately thirty minutes, as determined by the length of its timing channel.[88]

27

Short incubation times are sufficient for some ELISA and chemical assays, however, longer incubation time would extend the use of paper-fluidic devices to more sensitive nucleic acid amplification assays and even cell-based assays. While integrated devices exist that enable challenging sample preparation and nucleic acid amplification assays with sustained incubation periods, these devices require a user to either press,[37] fold,[89] tear[90,91] or slide[92,93] device components. Devices with multiple user involvement steps limit the number of assays that can be performed and introduce potential user error, motivating the development of automatic valve mechanisms.[40] Lafleur et al. demonstrated automated actuation of beeswax striped onto membranes that blocked fluid flow until heated.[26] Additionally, an automatic electrowetting valve can fully obstruct the flow of liquid using multiple electrodes printed on the membrane[94] but, like the previously described valve mechanisms, can only be actuated one time. Both of these automated valve mechanisms suffer from potentially complicated fabrication and/or increased device footprint to enable multiple reagent release. Current valve mechanisms to completely obstruct fluid flow are limited to single use, mostly short actuation times (on the order of seconds to minutes), and require complicated fabrication and/or user involvement.[30]

Composed of paraffin wax and pigment, wax-ink is a potential thermo-responsive material that could serve as a valve that fully obstructs fluid flow without affecting downstream chemistries. In this chapter, I explore wax-ink valves' utility by rapidly printing them onto varying porous membranes with a standard, desktop Xerox printer. Since the wax-ink prints onto the surface of the porous membranes, printed membranes can be heated to melt the wax into the depth of the membrane and block fluid flow through the porous channels,[33] creating a 'closed' valve. I expect subsequent, local heating will melt the wax again and 'open' the valves. Valves will be actuated by a thin-film heater while solutions of colored dye are wicked through the strips of prepared membranes for characterization of the flow past the valves. By time-lapse imaging the fluid flow, I characterize the valves by their heating requirements, actuation time, and fluid release and identify several tuning parameters including valve width, geometry, and surfactant addition.

2.2. Materials and Methods

2.2.1. Valve Fabrication

Open valves were prepared by printing solid wax-ink containing pigment and paraffin wax (Black ColorQube ink, Xerox) onto nitrocellulose (NC) and cellulose (Chr1) membranes (FF120HP & Chr1, GE Healthcare) using a Xerox ColorQube 8570. The membranes were cut into 4 mm by 20 mm strips on a Silver Bullet vinyl cutter (Silver Bullet Cutters). Closed wax valves were first prepared in the same manner as the open valves. Membranes were then heated for one (NC) or twelve (Chr1) minutes at 80ºC in a table-top oven and cut into 4 mm by 20 mm strips. Partially closed valves were heated in 15 second increments and manually cut with a razor blade into strips for imaging.

2.2.2. Valve Actuation

Valves were characterized by heating on a 28 Ω, 10 W/in^2 density polyimide thin-film heater (Cole-Parmer) using a 1550 B&K Precision Power Supply, and local temperature was recorded in real-time using a temperature data logger with a T-type thermocouple. Previously prepared membrane strips were adhered to the thin-film heater by sandwiching double-sided pressure sensitive adhesive (3M) between the heater and the membranes. The thermocouple was taped to the top face of the thin-film heater in order to detect the local temperature at the valve. The temperature was logged every five seconds. Actuation of the valves (Figure 2.1) was observed by wicking 2% solutions of water-soluble colored dye (McCormick, Sparks, MD) through the membrane strips. Wax valves were actuated by applying current to the thin-film heater. A Canon EOS Rebel T3i camera imaged the fluid flow at five second time-lapse intervals.
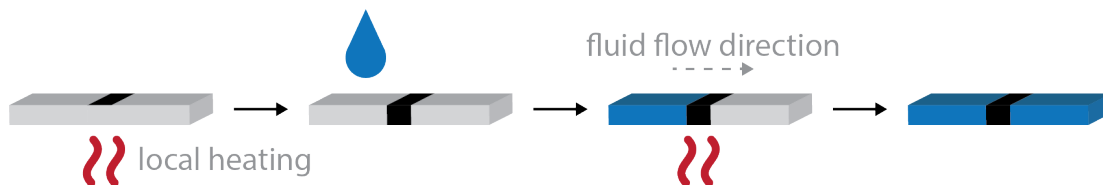
Figure 2.1 Schematic of wax-ink valve actuated by local heating.

2.2.3. Open-to-closed Valve Characterization

The penetration and distribution of wax in partially and fully closed valves (heated in an oven as described in **2.2.1 Valve Fabrication**) in nitrocellulose was visualized by imaging strips with a Epson V850 Pro scanner (Long Beach, CA) and a scanning electron microscope (3.0 spot size and 5kV probe current in high vacuum, FEI NOVA nanoSEM Field Emission) at 1000X magnification. Wax penetration was further visualized by imaging partially closed valve cross sections with a Canon EOS Rebel T7i camera with flash. The depth of penetration into the membrane was quantified by averaging the RGB mean grey value measured in ImageJ at 3 different regions across the valve width.

Open valves were closed in-situ by locally heating the valve. Twenty microliters of blue dye solution were applied upstream of an open valve and observed to flow past the valve. To determine the amount of time required for the wax-ink to permeate the wet membrane, 0.21 amperes was applied to the thin-film heater for 30-45 seconds. After an additional 30 seconds of incubation at room temperature, red dye solution was applied upstream of the actuated valve. Valve closure was confirmed by the absence of red fluid wicking past the valve.

2.2.4. Closed-to-Open Valve Characterization and Tuning

To determine the current required to actuate a closed-to-open valve, a 0.1 mm (NC) or 1 mm (Chr1) width closed wax valve was fabricated. Twenty microliters of blue solution were pipetted onto the membrane and observed for 20 minutes to ensure that no liquid wicked past the closed valve. The local temperature beneath the closed valve was then increased by applying 0.21 amperes to the thin-film heater for 2 minutes. The temperature at which the dye solution began to wick past the valve was recorded.

To meet the time constraints of varying assays, the amount of time required to open valves was determined for closed valves prepared with widths between 0.1 and 10 mm. Twenty microliters of blue solution were pipetted onto the membrane and observed for 20 minutes as described above. The local temperature beneath the closed valve was then increased by applying 0.21 amperes to the thin-film heater. The amount of heating time required for the sample to begin to flow past the valve was recorded. The valve was heated for an additional twenty seconds and the flow rate past the valve was determined by plotting distance wicked versus time.

30

To characterize the maximum fluid release through a valve, a 0.1 mm (NC) or 1 mm (Chr1) closed valve was heated for 25 (NC) or 14 (Chr1) seconds to initially open the valve and then an additional 15-30 seconds. Closed valves were fabricated as described in **2.2.1 Valve Fabrication** and adhered to a thin-film heater as described in **2.2.2 Valve Actuation**. Twenty microliters of blue solution were pipetted onto the membrane and observed for 20 minutes to ensure fully closed valves did not allow fluid leakage. The local temperature beneath the closed valve was then increased by applying 0.21 amperes to the thin-film heater. The flow rate past the valve was determined by plotting distance wicked versus time.

To characterize the effect of surfactant on valve opening, solutions of Tween-20, TritonX-100, and PEG 400 were deposited approximately 1 mm upstream of 0.1mm closed valves in NC. A lateral flow reagent dispenser (Claremont Biosciences, Upland, CA) was used to deposit the surfactant solutions at a rate of 2.33 µL/cm. Prepared membranes were cut into 4 mm by 20 mm strips. Twenty microliters of blue solution were pipetted onto the membrane and observed for 20 minutes to determine whether the surfactant caused fluid leakage past the valve.

2.2.5. Sequential Valve Actuation

To demonstrate the wax-ink valve's multiple actuation capability, a 0.1 mm open valve was printed onto nitrocellulose membrane. Twenty microliters of blue solution were pipetted onto the membrane and observed to wick past the open-valve. The local temperature beneath the open valve was then increased by applying 0.21 amperes to the thin-film heater for 30 seconds. Once the valve reached ambient temperature, twenty microliters of red solution were pipetted onto the membrane and flow was observed to stop at the then closed valve. The valve was actuated once more by opening the closed valve with 0.21 amperes applied to the thin-film heater for 20 seconds. The red food coloring was then observed to wick past the valve and the flow rate past the valve was determined by plotting the distance wicked versus time.

To demonstrate wax-ink valve's actuation in series, six 1-mm closed valves were printed onto a cellulose membrane strip. Twenty microliters of blue solution were pipetted onto the membrane and observed to stop at the first valve. The local temperature beneath the first valve was then increased by applying 0.21 amperes to the thin-film heater for 15 seconds to release solution through the valve. The solution was observed to stop at the next valve and imaged on an Epson

V850 Pro scanner (Long Beach, CA). Solution was similarly released through remaining valves by consecutively heating valves.

2.2.6. Alternative valve materials

To explore other valve materials and deposition methods, PureTemp 68x (PureTemp, Minneapolis, MN) was deposited onto NC and Chr1 with the lateral flow reagent dispenser used in **2.2.4 Closed-to-Open Valve Characterization and Tuning**. PureTemp 68x is solid at room temperature, so 0.022 g was dissolved in 2 mL of ethanol (190 proof). Dissolving the PureTemp 68x at a higher concentration caused clogging in the dispenser tubing. On 6" strips of NC and Chr1, 980 uL of solution was deposited onto the membrane (by running the dispenser over the same path multiple times) amounting to about 10.8 mg of PureTemp 68x deposited onto the 6" strip. Dispensing on shorter strips of membrane caused the valve to be much wider because of inadequate evaporation time between layers. Prepared membranes were cut into 4 mm by 20 mm strips. Twenty microliters of green solution were pipetted onto the membrane and observed for 20 minutes to check for leakage past the valve. The local temperature beneath the closed valve was then increased by applying 0.21 amperes to the thin-film heater. The amount of heating time required for the sample to begin to flow past the valve was recorded.

2.2.7. Statistical analysis

Microsoft Excel and GraphPad Prism (San Diego, CA) were used to calculate the standard error of repeated experiments. A Student's unpaired, two-sided t-test with a 95% confidence interval was used to compare the heating time to open a valve composed of wax-ink and PureTemp 68x phase change material.

2.3. Results and discussion

2.3.1. Valve Actuation

Thermally actuated wax-ink valves can be quickly incorporated into porous membrane networks for improved paper-fluidic control. Simply by varying the valve width and substrate, fluid flow through the valve can be customized for various assay needs. The printing resolution of the Xerox ColorQube defined the lower limit of the valves width; any black line designed thinner than 0.1 mm was automatically printed at 0.1 mm (Figure 2.2).
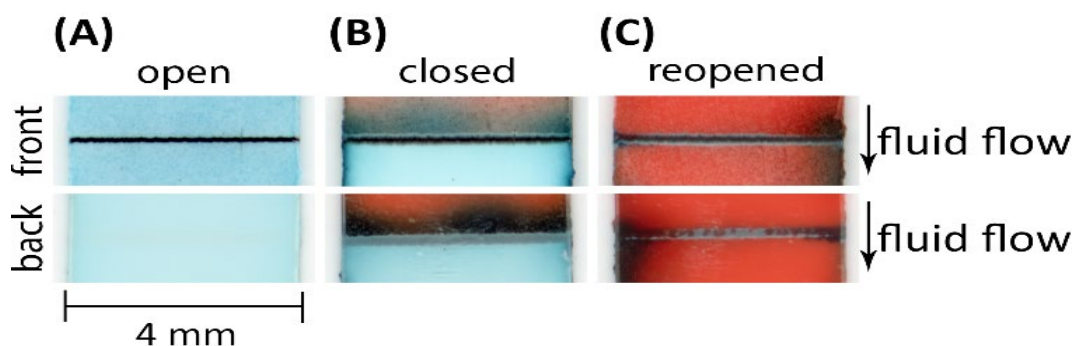
Figure 2.2 Wax-ink valve rapidly fabricated on nitrocellulose membrane is able to close and reopen.
(A) Initially open 0.1 mm valve with wax-ink on surface of the membrane does not block blue fluid passage. (B) Heated valve where wax-ink has permeated into the membrane blocking red fluid passage. (C) Re-heated valve opens again to allow red fluid to pass around the wax.

A 0.1 mm closed valve blocked liquid flow in NC for more than twenty minutes with no fluid leakage detected (Figure 2.2B). While I see no reason for valves to leak, when I tested for longer than twenty minutes, samples tended to evaporate making it impossible to determine whether fluid flow was prevented by the valve or by inadequate liquid. Notably, 1 mm was the lower limit of valve width on cellulose membrane; fiber length likely permits liquid to pass closed valves thinner than 1 mm.

2.3.2. Open-to-Closed Valve Characterization

As described by Martinez et al.,[33] wax ink printed into membranes can be heated to close the porous channels and block fluid flow. I imaged both native and printed nitrocellulose membrane

with a scanning electron microscope to confirm that the printing process did not substantially damage the pore structure of the membrane (Figure 2.3A&B). While the printing compressed the membrane to a thickness of about 76 μm (originally a 100 μm thick membrane), using a razor blade to cut the membrane into strips did not delaminate the membrane (Figure 2.3C). Cutting the membrane with a CO_2 laser (25% power, 100% speed, 500 PPI, VLS 3.5, Universal Laser Systems, Scottsdale, AZ) caused an angled edge and melts the wax at the edge (Figure A.1). Imaging the surface and edge of open, partially closed (heated 15 seconds), and fully closed (heated 60 seconds) valves demonstrates how the wax fills the pores of the membrane (Figure 2.3D-I).

Given the grey-scale imaging of SEM, it is difficult to differentiate the wax from the membrane and so I used a dSLR camera to better image the spread of wax when heated. As Figure 2.4 illustrates, an open valve does not fully penetrate the membrane. By calculating the mean grey value through the depth of the membrane, the wax seems to penetrate about half of the membrane Figure 2.4B. The SEM images (Figure 2.3D) indicate that the wax only penetrates about 15 μm of the membrane in an open valve; this discrepancy can be explained by 1) the lack of color in the SEM images that makes it difficult to discriminate the wax from the nitrocellulose membrane and 2) the distortion caused by not aligning the membrane edge perfectly normal to the dSLR lense. Nevertheless, the dSLR imaging indicates that, even after 60 seconds of heating to create a closed valve, the majority of the wax-ink remains in the top half of the membrane. Additionally, the wax-ink spreads into the depths of the membrane more than laterally. As the SEM images illustrate, the directionality of the pores likely facilitates the capillary flow of the wax-ink into the depth of the membrane.

Next, I tested valve closure in-situ by directing heat locally with a thin-film heater (rather than in an oven). Initially open valves actuated in-situ required at least 45 seconds of 0.21 amperes applied to the thin-film heater in order to close the valves when liquid was present (data not shown). Visual observation of the back face of the membrane confirmed that wax-ink permeated through the membrane (Figure 2.2B). Additionally, the lack of red dye flowing past the closed valve confirmed that the valve was fully actuated and closed.
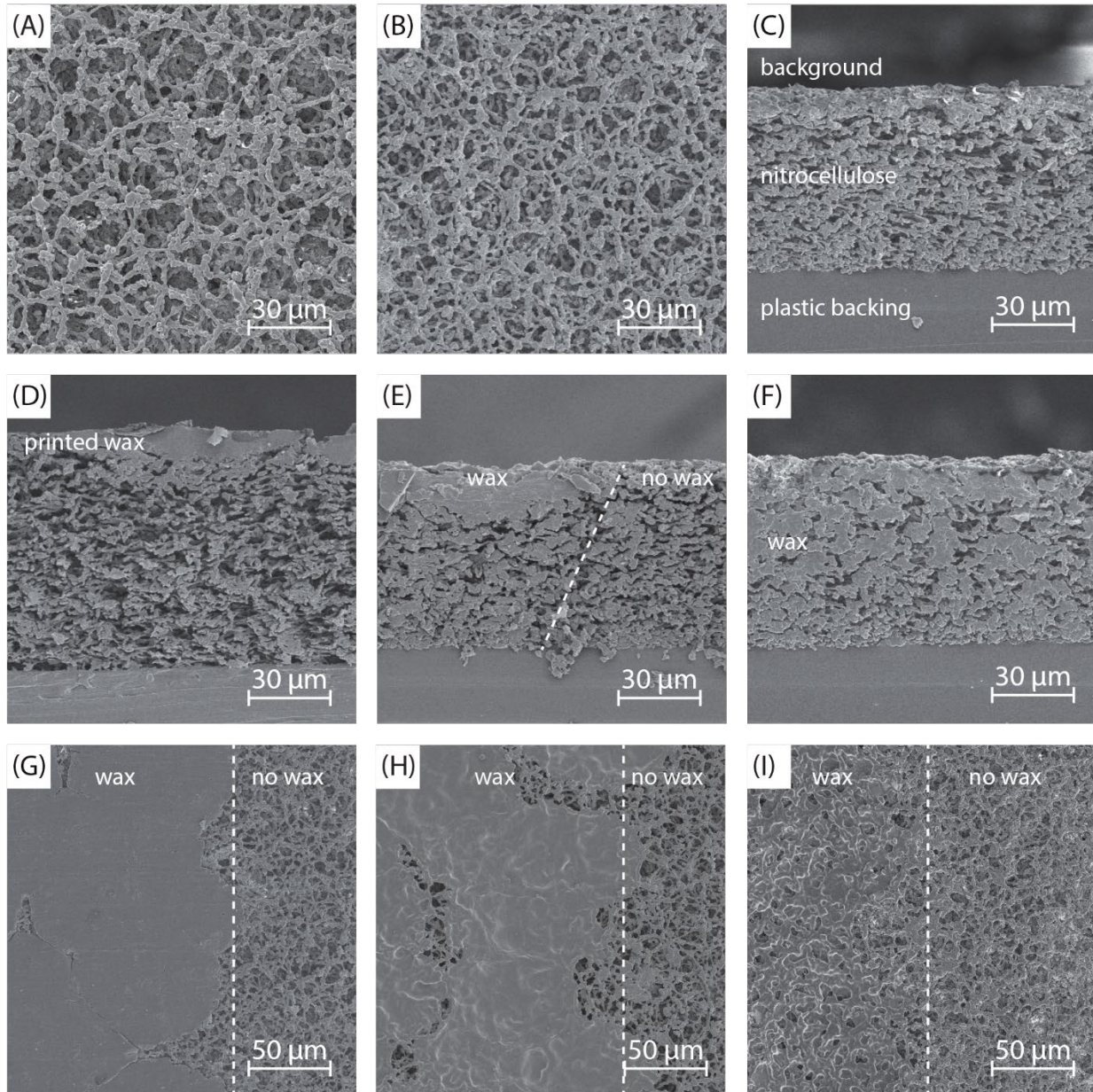
Figure 2.3 Scanning electron microscopy images of wax printed into nitrocellulose membrane.

(A) Surface of native nitrocellulose membrane compared to (B) surface of nitrocellulose membrane after printing through the Xerox ColorQube printer indicates that the printer causes negligible pore damage. (C) Edge of printed nitrocellulose membrane illustrates that printer compresses the membrane to about 76 µm thick (originally 100 µm). Cutting the nitrocellulose membrane does not cause delamination of the membrane from the plastic backing. (D) The edge of an "open valve" demonstrates that wax-ink only penetrates the membrane about 15 µm. (E) When heated for 15 seconds, the wax penetrates the membrane but when heated for (F) 60 seconds, the wax more fully fills the membrane pores. The wax on the surface of an (G) "open valve" penetrates the pores when heated for (H) 15 seconds but more completely when heated for (I) 60 seconds. Contrast adjusted in PhotoShop and ImageJ for image clarity.
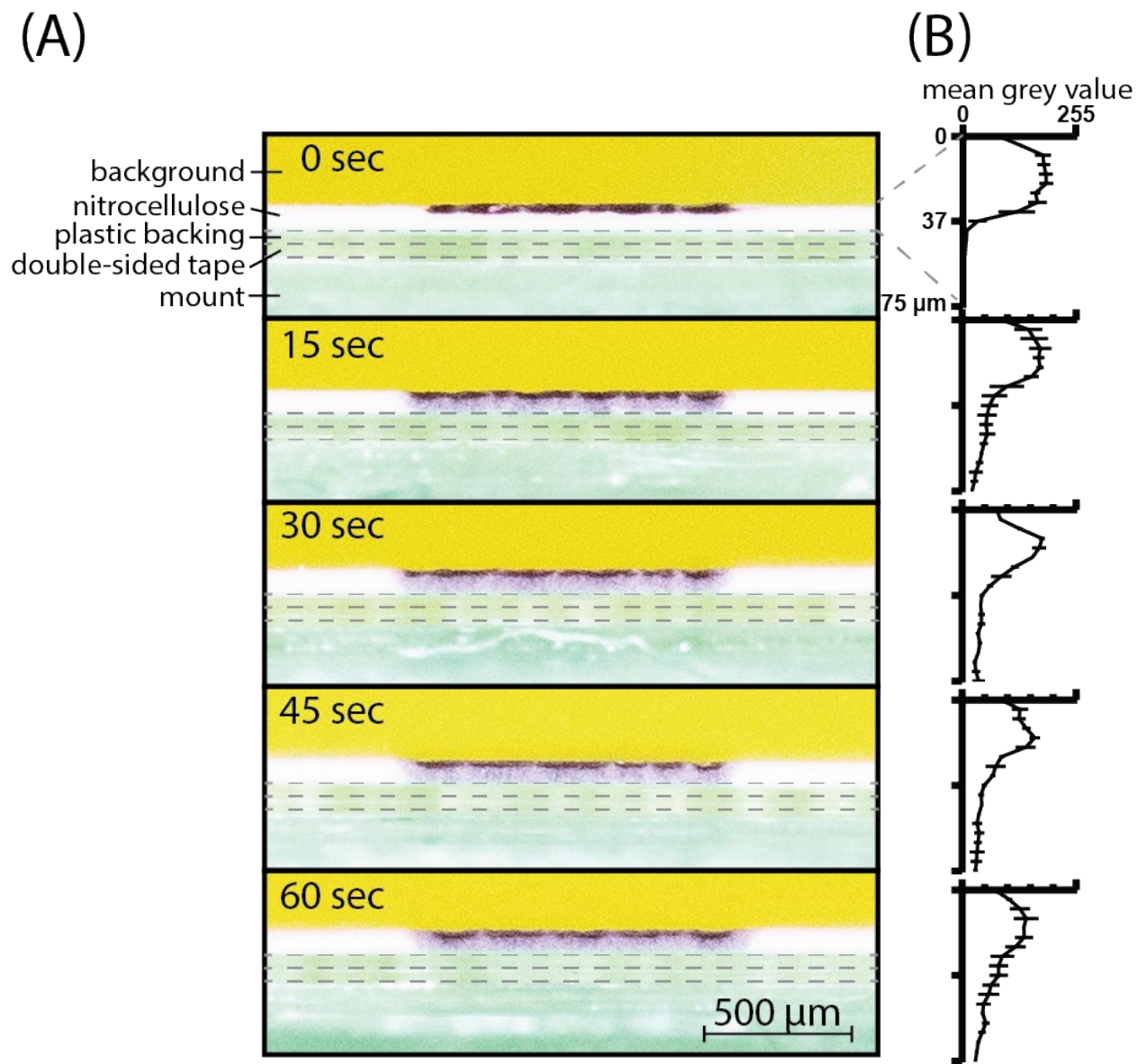
Figure 2.4 Distribution of wax-ink through partially closed valves.

(A) Images of edge of 0.1 mm valve printed onto nitrocellulose membrane and heated for 0 – 60 seconds demonstrate. (B) The mean grey value plotted against membrane depth. Error bars indicate standard error (n=3).

2.3.3. Closed-to-Open Valve Characterization and Tuning

A polyimide thin-film heater was utilized to characterize the opening of a closed valve and to determine the minimal heating (48 °C for 25 seconds on NC, 41°C for 15 seconds on Chr1, Figure 2.5A) required to actuate the valve (Figure 2.2C). The difference in actuation temperature between NC and Chr1 may be caused by NC's plastic backing that insulates the valve from the heater. As valve width increased, the amount of heating time required to open the valve was also increased (Figure 2.5B) and the fluid flow rate past the opened valve decreased. Valves wider than 1 mm (NC) and 10 mm (Chr1) were impassable (Figure 2.5C), presumably because the fluid pressure gradient created by the membrane capillarity was insufficient to displace the larger quantity of wax. A 4 mm valve was used to demonstrate the fluid front within the wax ink when the liquid was unable to flow through the valve. Similar flow patterns were observed in thinner valves on NC: wax-ink melts and flows with a concave profile (Figure 2.5C), permitting fluid to pass the edges of the valve until eventually developing a flat fluid front. Delamination at the edge of the membrane would normally explain this flow profile. However, since the SEM images did not show any delamination, I hypothesize that another factor, such as the heat distribution along the valve, causes the edge flow. Furthermore, when valves of varying geometry (linear, concave, and convex) were prepared in nitrocellulose membrane with wax-ink barriers (instead of being cut into strips), flow was observed to flow past the edges of linear and concave valvesFigure 2.6. Only convex valves had fluid pass through the midpoint of the valve which resulted in a much faster flow rate past the valve. The effect of valve geometry on heat transfer is explored more in Chapter 3.
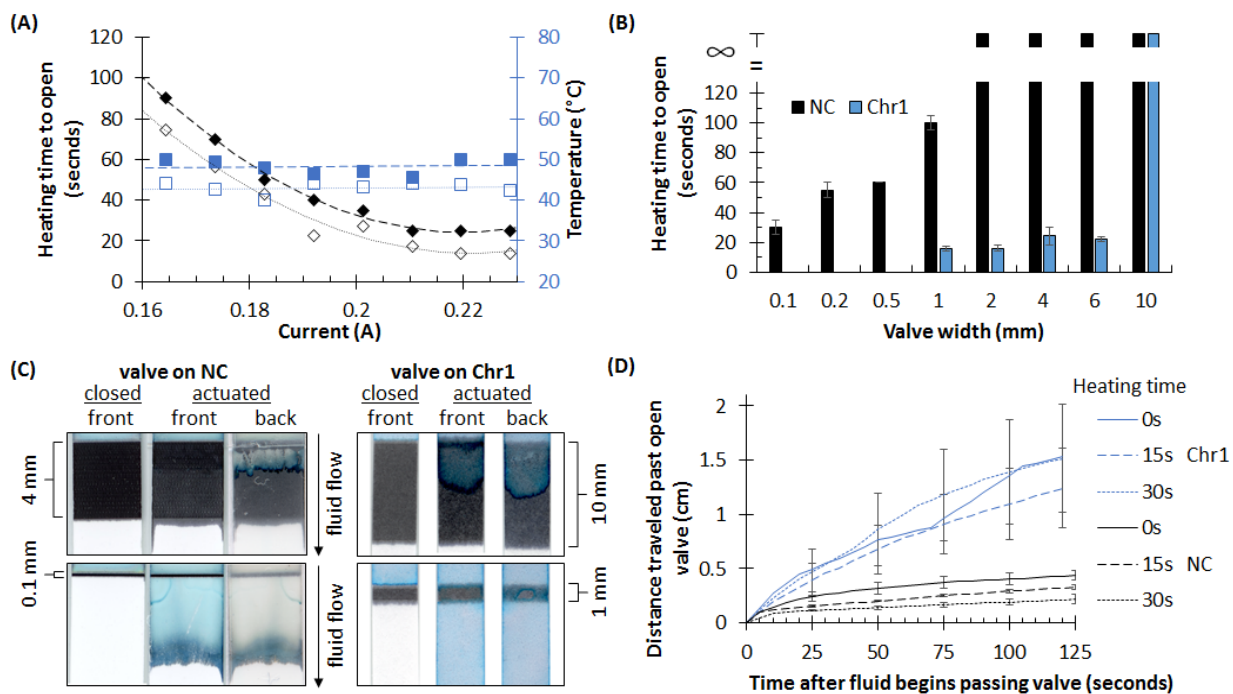
Figure 2.5 Valve Characterization.

(A) The length of time (diamonds) required to actuate valves decreases with increased current while the valve actuation temperature (squares) remained approximately 48°C (NC, closed symbol) and 41°C (Chr1, open symbol). (B) The length of heating time required to release fluid through a valve increased with valve width, however, valves greater than 1 mm (NC) and 10 mm (Chr1) wide are impassible (n = 3). (C) Representative images of fluid flow in the NC and Chr1 membranes showing minimum valve widths that allowed flow (0.1, 1 mm) and that were too wide to allow fluid to pass (4, 10 mm). (D) Additional heating of a 0.1 mm (NC) and 1 mm (Chr1) valve does not increase the amount of fluid to pass through the valve. More fluid can wick through open valves on Chr1 than NC but with greater variance (n = 3). Error bars indicate standard error.
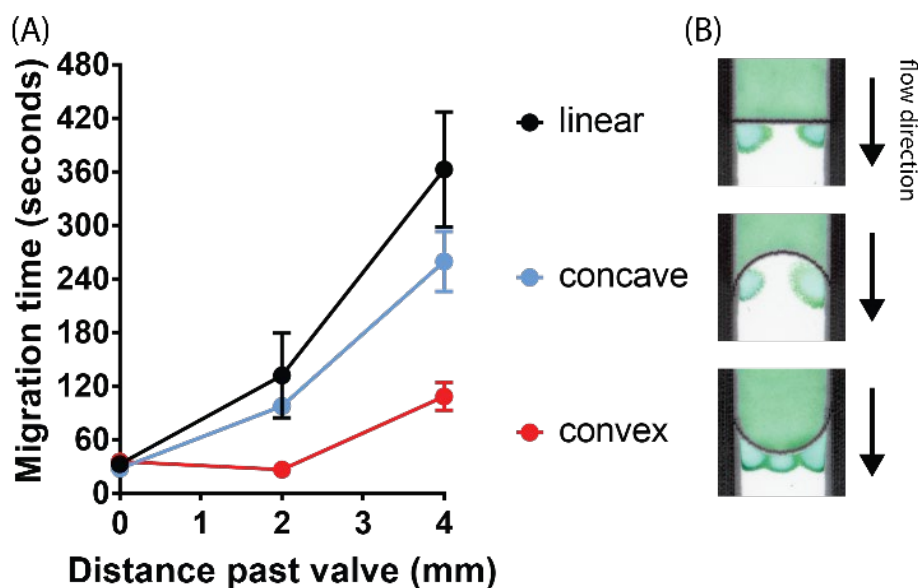
Figure 2.6 Effect of valve geometry on flow rate past opened valve.

(A) The flow of liquid past linear valves is slower than past concave and convex valves. n=3; error bars indicate standard error (B) Only convex valves were observed to have flow past the midpoint of the valve. Both linear and concave valves had flow only along the edge of the valve.

If a greater fluid flow rate is required than the 0.1 mm linear valve in NC enables, then the density of the valve might be printable in grey-scale much as Ouyang, *et al.* accomplished with their passive, toner-based valves.[81] However, in my hands, closed wax valves printed in grey-scale could not prevent fluid flow for as long as the black-wax valves due to inconsistent spacing between the printed wax-ink dots of the valve and thus incomplete valve closure during heating (Figure 2.7). To achieve a grey line, the printer uses halftone to increase the space between printed dots. The more grey the valve (the lower the black or K value in CMYK color mode), the greater the spacing between wax-ink dots. As (Figure 2.7A) illustrates, as the K value decreases, the leakage of fluid past the valve increases. Though none of the 0.1 mm valves tested with K values less than 100 were able to block fluid flow, by printing a wider valve in grey-scale, the fluid release could likely be tuned.
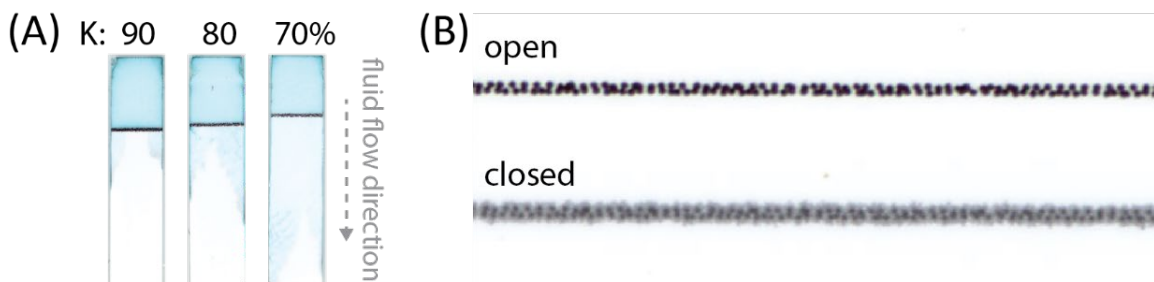
Figure 2.7 Closed wax valves prepared in grey scale.

(A) Closed valves (0.1 mm in nitrocellulose) prepared with decreasing K value (black value in CMYK color mode) leak fluid before actuation. (B) The spacing between dots of the 0.1 mm valve (90% K) is observably inconsistent before it is "closed".

To increase fluid release through closed-to-opened valves, I both decreased valve width to the minimum resolution in each membrane and attempted to increase the length of time that the valve was heated following the initial time required to open the valve (Figure 2.5D). Hypothesizing that additional heating would permit complete, vertical heat transfer into the valve, a 0.1 mm (NC) and 1 mm (Chr1) valve were heated for an additional 15 and 30 seconds but was found to decrease the total liquid released. The thin-film heater used had a greater surface area than the valve, and therefore the membrane and fluid surrounding the valve also increased in temperature. The surrounding liquid tended to evaporate, which then decreased both the hydraulic pressure and the total amount of liquid available to wick through the membrane. However, Chr1 was found to release much more liquid than in NC but with greater variance, presumably due to fiber length variance.

Hypothesizing that surfactants could also increase the fluid release through closed-to-opened valves, I first tested whether surfactant deposited upstream of a closed valve would cause premature leakage past 0.1 mm (NC) valves. As shown in Table 2.1, when high concentrations (0.045-0.09 v/v%) of Tween-20 and PEG 400 were deposited upstream of the valve, fluid passed the valve less than 20 minutes after depositing the sample. However, none of the tested solutions of TritonX-100 caused leakage past the closed valves during the observed time. It is unsurprising that Tween-20 caused a leakage given that it has a greater hydrophilic-lipophilic balance (HLB) than TritonX-100 (16.7 vs. 13.5). Since PEG 400 has a much lower HLB of 11.4 I would have not expected it to cause premature leakage. But given the concentration effect of leakage, this experiment would need to be repeated to confirm there was not an error preparing the dilutions.

Next, I tested whether Triton X-100 could increase the fluid release through an opened valve (Figure 2.8). As expected, solutions of 1.8% Triton X-100 deposited upstream of 0.1 mm valves permitted more fluid to release past an opened valve than valves with 0.9% Triton X-100 deposited upstream. These results indicate an opportunity to use surfactants to further tune fluid release past a valve.
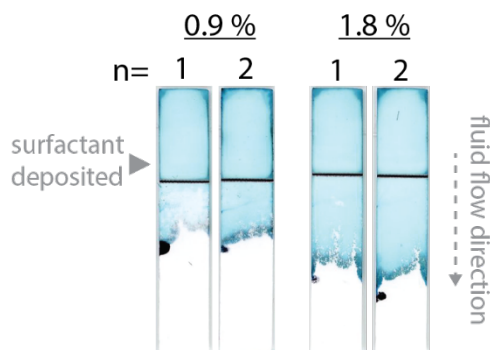
Figure 2.8 Effect of surfactant on fluid release past a valve.

Increasing the concentration of Triton X-100 deposited upstream of a 0.1 mm valve in nitrocellulose membrane causes more fluid to release past the actuated valve.

Table 2.1 Effect of surfactant on closed valve leakage. (n=2)

Surfactant	Deposited concentration (v/v%)	Leaked within 20 minutes?
Tween-20	0.02	N
	0.045	Y
	0.09	Y
TritonX-100	0.02	N
	0.045	N
	0.09	N
PEG 400	0.02	N
	0.045	Y
	0.09	Y

2.3.4. Sequential Valve Actuation

Starting with a valve that was initially open on NC, I heated the wax to close the valve, and then re-opened the valve by heating a second time. To my knowledge, this is the first demonstration of a reconfigurable valve allowing multiple actuation steps within a paperfluidic device. As opposed to previously existing single-use valves in porous membranes, multiple reagents can be released through a single valve as shown in Figure 2.9 and Figure A.2. While I was unable to demonstrate additional actuation beyond the two events shown, even the passage of two distinct solutions improves reaction complexity. Sequential fluid flow through a single valve permits a smaller device foot-print and lowers fabrication costs.
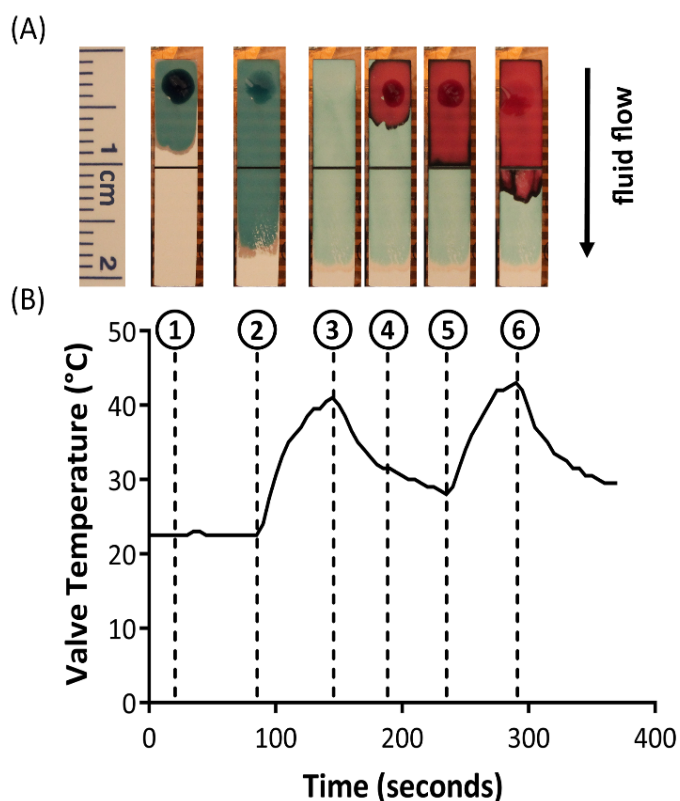
Figure 2.9 Multiple Actuation of a Single Valve.

(A) Images and (B) Temperature profile of valve on NC. At (1), blue liquid is added to the membrane and flows through the open valve (2). (3) Upon heating, the valve closes. At (4), red liquid is added to the membrane as the valve cools. In (5), this liquid is blocked by the closed valve. When re-heated, the valve opens to allow the red fluid to pass (6).

Additional reaction complexity can be achieved by printing a series of valves on a single membrane strip, as demonstrated in Figure 2.10 using Chr1. Consecutive heating of valves permitted the release of liquid into seven discrete zones.
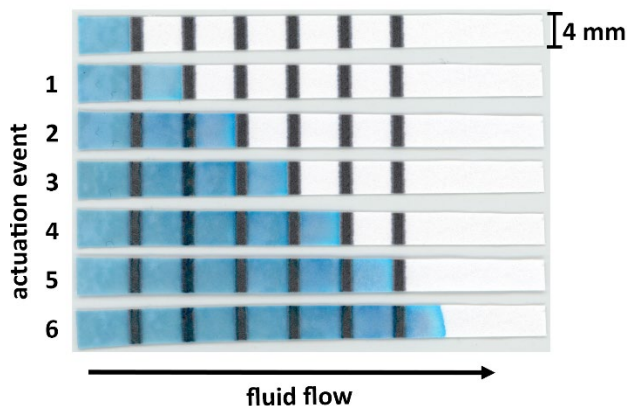
Figure 2.10 Sequential Valve Actuation.

Valves printed on Chr1 were consecutively heated to permit controlled, sequential release of liquid into discrete zones, independent of wicking speed. Time between valve heating was approximately 3 minutes.

2.3.5. Alternative valve materials

The relatively low actuation temperature of the wax-ink valves may prevent higher temperature reactions or assays from being performed adjacent to the valve. PureTemp 68x is a commercially available phase-change material that is rated to melt at 68ºC. Initially, I tried depositing the PureTemp 68x onto membrane with the Xerox ColorQube printer. Using PDMS, I created a mould of the solid-ink cartridge and prepared a custom solid-ink cartridge composed of PureTemp. However, when this custom cartridge was loaded into and heated by the ColorQube printer, the very low viscosity of the material at high temperatures (comparable to the viscosity of water) caused it to melt into the insides of the printer. I then tried loading PureTemp 68x into the cartridge of a lab-grade dot inkjet printer (Dimatix, FujiFilm). However, the cartridge heads clogged very easily and it was nearly impossible to dispense PureTemp 68x using the Dimatix. The most successful deposition method was to dissolve PureTemp 68x with ethanol and deposit layers using a lateral flow reagents dispenser. Using this deposition method, I was able to create approximately 1 mm closed valves in both nitrocellulose and cellulose membrane that could constrain liquid from passing for at least 20 minutes. Despite the PureTemp 68x having a higher

melting temperature than wax-ink, much less time was required to actuate the valve (Figure 2.11). The lower viscosity of melted PureTemp 68x likely creates less resistance for a sample to wick past. I was unable to create an open valve that could be in-situ closed. If a different solvent could be identified to prepare a higher concentration of PureTemp 68x solution, then it may be easier to deposit a single layer on the surface of the membrane.
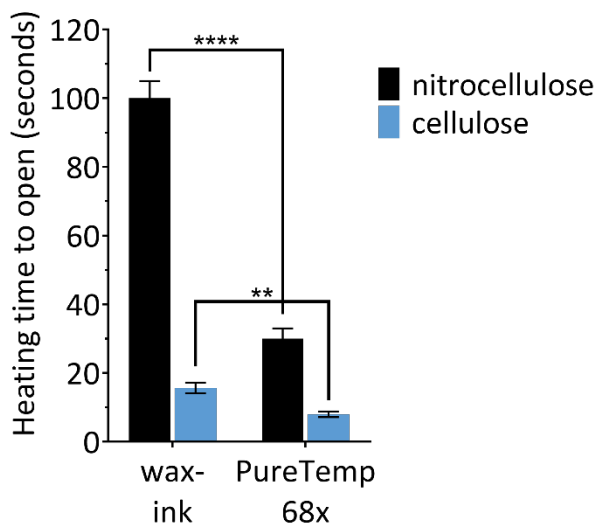
Figure 2.11 Dependence of valve material on actuation time.

Valves prepared with PureTemp require less heating time to open than wax-ink valves in both nitrocellulose and chromatography membranes. n=3; ** indicates $p \leq 0.01$ and **** indicates $p \leq 0.0001$.

2.4. Future Directions

In this chapter, I demonstrated that wax-ink can be deposited into membranes to constrain liquid to discrete zones for controlled release when heated. By adjusting several parameters, such as width, heating time, and material, the release of liquid past the valves can be tuned. However, there remain several opportunities to better characterize the valves' opening and closing. Imaging with an SEM and a dSLR provided insight into the wax distribution of closed and partially closed valves. While the SEM can discriminate individual pores, it was difficult to differentiate the wax-ink from the porous membrane and therefore difficult to fully characterize the distribution of the wax within the membrane. Other techniques that can discriminate individual pores may permit a better characterization of wax distribution. For instance, particle image velocimetry (PIV) can be used to analyse the flow of tracer particles within microfluidic channels. When velocity fields of

a time-series experiment are overlayed, micro-features such as pores can be identified. PIV therefore may be able to better elucidate the wax distribution of a closed valve within porous membranes than SEM.

The opacity of the wax also made it difficult to visualize its behaviour and flow when a valve was being opened. Imaging valves after they had been heated only provided an end-point measurement of wax flow when a valve was opened (i.e. a concave flow profile with wax traveling furthest along the edges of the membrane). By embedding fluorescent particles within the wax, the valve could be better visualized and characterized by fluorescent microscopy while the valve is opening, instead of just at the end time-point. By using confocal microscopy, it may be possible to visualize the flow of the wax through the depth and better understand why, for instance, liquid samples tend to flow past the valve along the bottom face of the membrane. Fluorescence microscopy could also better elucidate the flow of liquid samples through the valve by adding tracer particles into the sample. The tracer particle flow behaviour could be analysed by PIV or by SEM to confirm whether the sample travels through fissures in the valve, as Downs and colleagues recently demonstrated when analysing wax valves in fabric-based devices.[95,96]

To embed fluorescent particles into the wax, a non-proprietary wax-ink cartridge would need to be used. Furthermore, as discussed in section 2.3.5, the melting temperature of the wax-ink used in this study may restrict higher-temperature assays and reactions from being performed adjacent to a closed valve. To my knowledge, only wax-ink and beeswax[26] have been demonstrated to constrain and release liquid in paper membranes by thermal actuation. While I began to explore other phase change materials, such as PureTemp 68x, deposition remains a challenge that needs to be overcome to have better control over the quantity and distribution of material deposited. For instance, an inkjet printer with a heat-controlled cartridge would allow for greater deposition control. Likely, the ability of water to displace the melted, opened valve depends on valve material's attraction to the substrate and its resistance to flow. By depositing other materials, other parameters of the valve can be explored, such as the effect of its viscosity and surface tension on fluid passage.

2.5. Conclusion

I have demonstrated, to my knowledge, the first use of wax as more than a static barrier to fluid flow in porous membranes. Instead, the reconfigurable wax valves described in this chapter

45

allow both complete fluid obstruction and multiple actuation steps with a single membrane strip. I identified several tuning parameters including valve width, heating time, geometry, and material (both of the valve and the substrate it is deposited onto) that can modulate fluid release. Both macro-analysis (time-lapse imaging) and micro-analysis (scanning electron microscopy) were used to characterize the valve within the porous membranes. By employing other techniques such as tracer particle analysis and by studying other valve materials, we could better understand what other parameters effect fluid flow through thermally-actuated valves.

3. THERMAL CONDUCTIVITY ANALYSIS OF WAX-INK VALVES

3.1. Rationale

Many theoretical models have been created to predict and simulate the flow of liquid in paper diagnostic membranes.[97–100] Wax-ink has been printed and melted into membranes to create hydrophobic barriers that define fluidic channels; however, the only models created to describe the barrier fabrication have described the capillary flow of the wax-ink and not the influence of the heat transfer to melt the wax.[71,100] Few thermal analyses have been performed on paper diagnostic membranes because assays requiring heating within porous membranes are a recent development.[101] The few thermal analyses that have been reported focus on the heat source and not the heat transfer within the porous membrane.[102,103] Thermally-actuated valving mechanisms exist for traditional microfluidic devices, however, the thermal analyses of their actuation do not sufficiently describe the unique heat transfer within a porous membrane.[104]

The characterization studies of wax-ink valves performed in **Chapter 2** revealed an unexpected phenomenon: the flow of liquid past closed-to-open valves began at their edge. The flow front of liquid in an LFIA is typically uniform; a convex or concave flow front through nitrocellulose membrane is usually indicative of damage to the membrane such as delamination from the backing.[105] Since membranes without the valve permitted uniform flow and SEM imaging did not indicate membrane damage, it is more likely that the edge flow is caused by non-uniform opening of the valve. To explore factors that can cause non-uniform heating of the valve, I simulated the heat transfer into a valve embedded into 3D porous media. I identified two sources of heat loss (convective and evaporative) that contribute to a temperature gradient in the valve and explore the effect of valve geometry on heat transfer.

3.2. Materials and Methods

3.2.1. IR imaging of valve

When the linear valves described in **2.3.3 Closed-to-Open Valve Characterization and Tuning** were opened in-situ, fluid was consistently observed to flow first past the edges of the valve. To confirm that this edge flow was not caused by delamination at the edge of the strips or

some other artefact caused by cutting the strips, test strips were prepared with wax-ink barriers defining a flow channel. A 0.5 cm long, 1 mm wide valve with a 0.5 cm barrier of wax on either side of the channel was printed onto nitrocellulose. The membrane was then heated for one minute at 80ºC in a table-top oven to close the valve and create the hydrophobic barrier.

The membrane was adhered to a hot plate with double-sided tape (Figure 3.1). A 30 µL sample of water was applied upstream of the valve and the hot plate set to 80ºC. An infrared (IR) thermal imaging camera (A300 Series, FLIR Systems, Sweden) imaged the membrane until water was observed to pass the valve. The recorded temperature at selected time points was plotted in ImageJ for visualization.
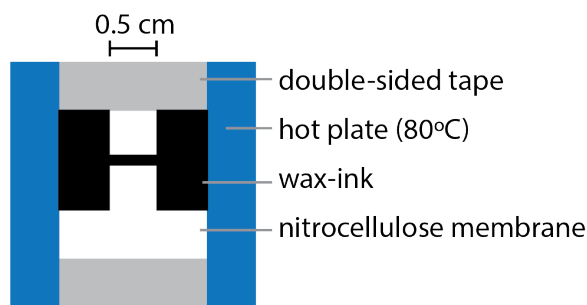
Figure 3.1 Schematic of valve to be imaged with an IR camera.

3.2.2. Heating orientation

In a brief collaboration with Brian Jun and Adib Ahmadzadegan of Purdue University, a dilution of 600 nm fluorescent tracer particles was deposited onto a nitrocellulose membrane with a 0.1 mm closed valve. While actuating the valve with a thin-film heater, as described in **2.2.2 Valve Actuation,** a 20x objective was used to image the flow of the particles through the valve. The thin-film heater was aligned such that the resistive heating elements were either perpendicular or aligned with the wax-valve (Figure 3.4A&B).

3.2.3. COMSOL simulation of wax-ink valve heating

In order to characterize the heating of valves, I created a multiphysics-based model of valves in porous media partially saturated with liquid water and water vapor (Figure 3.2). Evaluations of heated valves were produced using COMSOL Multiphysics 5.4 with the Heat Transfer, CFD, Microfluidics, and Subsurface Flow Modules and on a Dell Optiplex 980 (Intel Core i7 CPU processor running at 2.93 Ghz with 8 GB RAM). The 3D geometry was built in COMSOL (an

ellipse was imported from Adobe Illustrator to create concave and convex valve domains). A membrane test strip was modelled as a porous block with a layer (linear valve) or extruded geometry (concave and convex valves) surrounded by a block of dry air. A boundary heat source on the bottom face of the geometry simulated heating from a thin-film heater. The sources of heat loss were 1) a convective heat flux with ambient air in laminar flow simplified to only flow in the x-direction and 2) evaporative heat loss (based on the model "Evaporation in Porous Media with Large Evaporation Rates"[106]). Radiation effects were not included in the model because they were considered to be negligible as discussed in **3.2.5 Radiation Effects**. Model parameters are listed in Table 3.1.
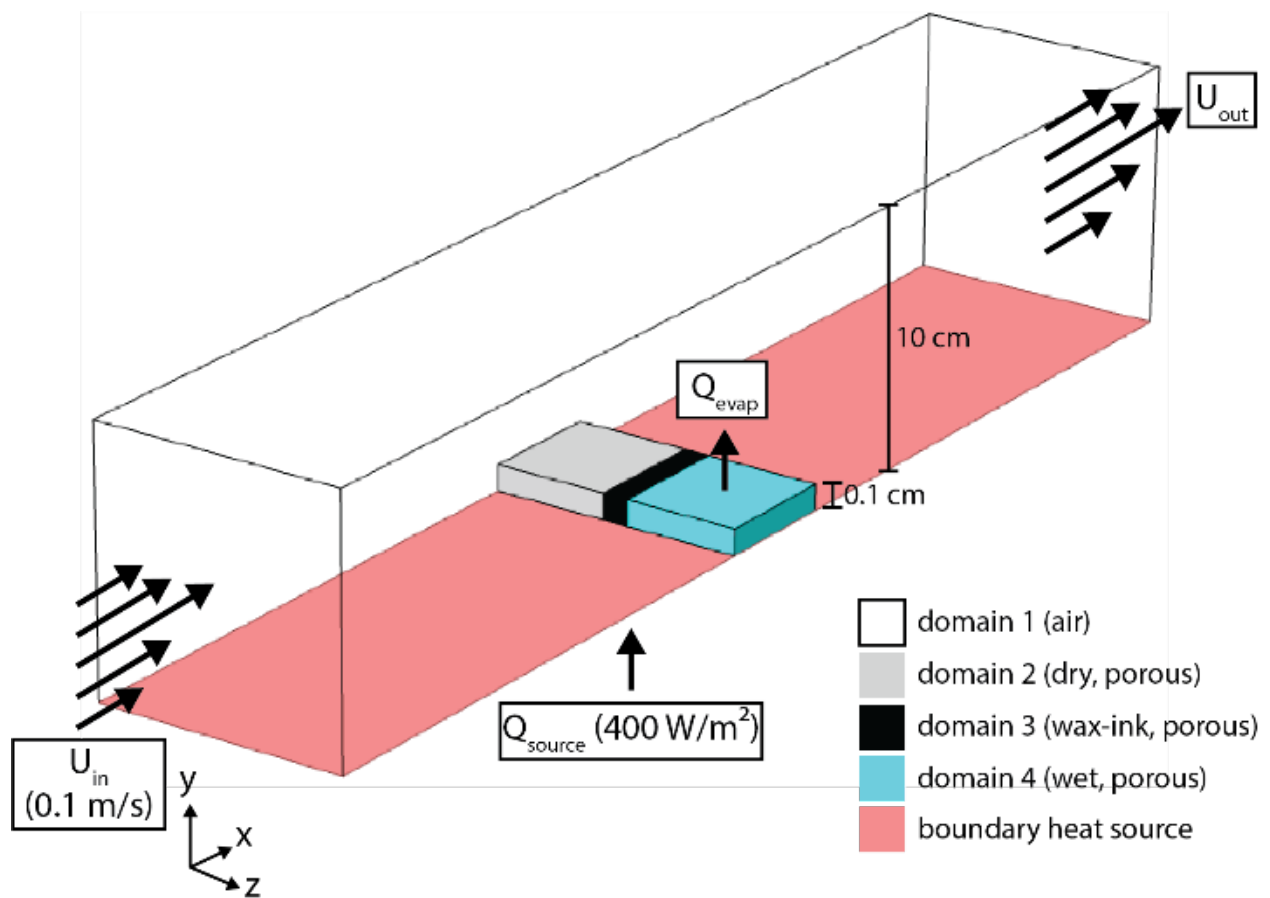
Figure 3.2 Schematic of model of heat transfer in wax valve in porous media.

A boundary heat source simulates a thin-film heater and heat loss is accounted for by convective heat flux of ambient air in laminar flow and evaporative heat loss.

.

Table 3.1 COMSOL parameters to simulate the heating of a wax valve.

Parameter	Value	Source
ambient pressure	1 atm	estimated
ambient temperature	293.15 K	estimated
free stream velocity	0.1 m/s	estimated
initial water saturation in domain 4	0.5	estimated
thermal conductivity of cellulose	0.09 W/(m*K)	[107]
porosity of cellulose	0.8	[99]
permeability of cellulose	$1 \times 10^{-15}\, \text{m}^2$	[99]
heat capacity of cellulose	1650 J/(kg*K)	[107]
density of cellulose	1528 kg/m^3	[99]
thermal conductivity of wax-ink	0.18 W/(m*K)	[108]
heat capacity of wax-ink	2250 J/(kg*K)	[108]
density of wax-ink	820 kg/m^3	[108]
boundary heat source	400 W/m^2	[103]

3.2.4. Governing equations

Briefly, heat transfer was coupled to laminar flow in the porous medium domain using the nonisothermal flow interface. This coupling is commonly used to describe slow flow environments and allows for the fluid density to fluctuate with temperature (as occurs in this model because of the multi-phase flow of water vapor and liquid water during evaporation).[106] The governing heat transfer equation includes convection and conduction (Equation 1):

$$\rho C_p \mathbf{u} \cdot \nabla T + \nabla \cdot \mathbf{q} = Q + Q_p + Q_{vd} \qquad \text{Equation 1}$$

where ρ describes the fluid density, c_p describes specific heat, u is velocity, T describes temperature, Q accounts for heat from the boundary source and latent heat of evaporation, Q_p accounts for work done by pressure changes caused by the compressible flow, Q_{vd} accounts for heat from viscous dissipation, and q is described by Equation 2:

$$\mathbf{q} = -k_{eff} \nabla T \qquad \text{Equation 2}$$

where k describes the thermal conductivity. Notably, the thermal conductivity in the porous domain (Equation 3)

$$k_{eff} = \theta_n k_n + (1 - \theta_n) k + k_{disp} \qquad \text{Equation 3}$$

is dependent on the solid volume fraction in the porous cellulose medium, θ_p, the thermal conductivity of the cellulose, k_p, the thermal conductivity of the wax-ink or water and water vapor, k, and thermal conductivity from dispersion in porous media, k_{disp}.

In the ambient air domain, there is only transport of moist air so the velocity is solved by the Navier-Stokes equation (Equation 4):

$$\rho \left(\frac{\partial \mathbf{u}}{\partial t} + \mathbf{u} \cdot \nabla \mathbf{u} \right) = \underbrace{-\nabla p}_{2} + \underbrace{\nabla \cdot (\mu(\nabla \mathbf{u} + (\nabla \mathbf{u})^T) - \frac{2}{3}\mu(\nabla \cdot \mathbf{u})\mathbf{I})}_{3} + \underbrace{\mathbf{F}}_{4}$$

$$\underbrace{\phantom{\rho \left(\frac{\partial \mathbf{u}}{\partial t} + \mathbf{u} \cdot \nabla \mathbf{u} \right)}}_{1}$$

Equation 4

where u is velocity, p is pressure, ρ is density, μ is fluid dynamic viscosity accounting for 1) intertial forces, 2) pressure forces, 3) viscous forces. This is solved with the continuity equation $\nabla \cdot (\rho \mathbf{u}) = 0$.

Within the porous domain, there is two-phase flow of water vapor and liquid water. The Brinkman equation is used to solve for the velocity of the vapor and Darcy's Law is used to solve for the velocity of liquid water. The Brinkman equation, an extension of Darcy's Law, is appropriate to use for the gaseous vapor phase because it more accurately describes fast-flow within a porous domain. Darcy's Law is appropriate for describing slow flow within porous domains, as is expected by the water within the porous membrane.[109]

3.2.5. Radiation effects

Radiation between two bodies, such as a thin-film heater and a test strip, can be modified from the Stefan-Boltzmann Law to $\Delta E = \epsilon_{eff}\, \sigma A F_{A \to B}(T_A^4 - T_B^4)$ where ΔE is the heat transfer rate, ϵ_{eff} is the emissivity, σ is the Stefan-Boltzmann constant, A is the surface area, F is the view factor, and T is the temperature of the bodies. Assuming the greatest energy transfer between two black bodies ($\epsilon_{eff} = 1$) and close proximity between the heater and the membrane (F=1), this equation can be simplified to $\Delta E = \sigma A(T_A^4 - T_B^4)$. Considering a test membrane of m^2 at an initial temperature of 20ºC, the maximum radiative energy transfer between the membrane and a heat source at 200ºC would be 0.012W. Compared to the 0.44 W estimated heat source of a thin-film heater used to actuate the valves, radiation can be neglected.

3.3. Results and discussion

3.3.1. IR imaging of valve

To confirm that edge flow past closed-to-open valves was not caused by delamination at the edge of strips, a nitrocellulose membrane was prepared with a closed valve and wax boundaries (Figure 3.1). Before applying a water sample, the ambient temperature was observed to be several degrees above the typical 20 ºC (Figure 3.3A) because of the hot plate not being sufficiently cooled from a previous experiment and because of material reflectance which obscures the IR camera's readings. When the water was deposited onto the membrane and the hot plate simultaneously turned on to 80 ºC, the temperature difference between the water and the surrounding membrane, wax, and hot plate was immediately evident (Figure 3.3B). This temperature difference was used to draw an initial water boundary that is overlaid on all plots (Figure 3.3A-E). The low resolution of the IR camera made it difficult to precisely identify the wax boundaries and the time steps were not indicated in the depicted plots because the hot plate took much longer to heat than the thin-film heater used during previous characterization studies. However, the same sample migration trends are observed. Water begins to travel along the edge of the membrane (Figure 3.3C) and then spreads into the wax (Figure 3.3D). And, consistent with trends observed in **2.3.3 Closed-to-Open Valve Characterization and Tuning**, water eventually flows through one edge of the wax valve (Figure 3.3E). Notably, the temperature of the wetted membrane upstream of the valve was always several degrees cooler than the surrounding wax and dry membrane regions. At the timepoint depicted in Figure 3.3D, more water was applied to the test strip because the initial sample evaporated. This evaporative heat loss could account for a temperature difference across the wax valve that causes the edge of the valve to melt first and is modeled in 3.3.3.
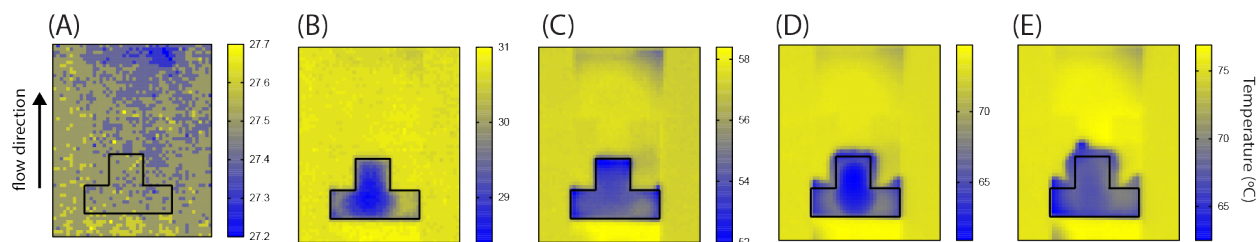
Figure 3.3 IR thermal plots of actuated wax-ink valve.

(A) Ambient temperature plot with sample region outline overlaid. (B) Water is constrained by strip edges and wax boundaries when initially deposited. (C) The water remains several degrees below the temperature of the wax even when the wax reaches ~ 56ºC and water is observed migrating along edges of membrane. (D) Water totally evaporated so more was applied to the center of sample region. (E) Water is observed to flow through one edge of the wax valve. The temperature preceding the valve and where the water is deposited is plotted in Figure A.1.

3.3.2. Heating orientation

In all characterization studies of Chapter 2 the wax valve was oriented parallel and directly above a resistive trace of a thin-film heater. When the wax valve was aligned perpendicular to the heating element traces, flow of fluorescent tracer particles through an actuated valve was observed to travel through fissures spaced and oriented directly above heating element traces (Figure 3.4). Likely, the wax directly above the heating element melts faster than the surrounding wax.
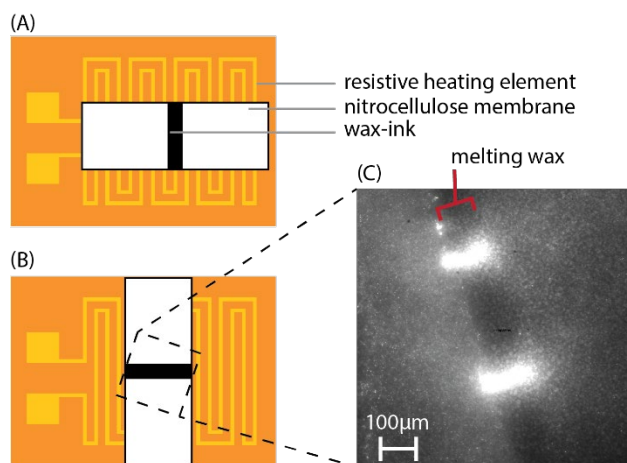
Figure 3.4 Wax valve alignment with thin-film heater.

Closed wax-ink valves were aligned (A) parallel and (B) perpendicular to resistive heating element. (C) Fluorescent tracer particles are observed to primarily flow through fissures in the valve directly above heater traces. Image courtesy of Brian Jun and Adib Ahmadzadegan.

3.3.3. COMSOL simulation of wax-ink valve heating

As illustrated in Figure 3.5, the temperature is several degrees hotter on the bottom face of the valve than the top face of the valve. This temperature difference is consistent with experimental results from 2.3.3; samples tended to flow through and past the valves faster along the bottom face of the membrane than along the top face of the membrane. The lower density of wax along the bottom face of the valve (Figure 2.4) likely provides less resistance to fluid passage. If the temperature is also higher at the bottom face, as the COMSOL results indicate, then more wax on the bottom face would be melted and similarly permit fluid passage. These effects combined can explain the greater flow along the bottom face of the membrane.

Due to convective heat transfer, there is a measurable difference in temperature along the length (x-axis) of the valve. I simplified the model to include a free stream velocity of 0.1 m/s in only one direction. In reality, there is multi-directional air flow. However, given the locations of HVAC vents in our laboratory, it is reasonable to assume a predominant air flow in one direction. For context, a laminar flow laboratory cabinet has a typical flow velocity of 0.2 - 0.6 m/s. Given the HVAC system in our laboratory, I assumed a comparable magnitude of air flow across the test membranes. When a laminar air flow is included in the model, the temperature of the wax at the edge (closest to the air inlet) of the membrane is several degrees higher than the wax at the midpoint of the valve (Figure 3.6A&B). As expected, when this air velocity is much higher (Figure 3.6C) the temperature of the wax never reaches its melting temperature and when the air velocity is much lower and nearly negligible, the wax heats rapidly. I included evaporative heat loss in the model because of the IR imaging results in **3.3.1 IR imaging of valve**. When evaporative heat loss is neglected from the model, the temperature difference between the middle and the edge of the wax valve increases slightly. As expected, the entire valve heats faster than when evaporative heat loss is neglected. The several degree temperature difference between the middle and edge of a heated valve is consistent with both the IR imaging results (Figure 3.3) and observations of flow past the edge of a valve (**2.3.3 Closed-to-Open Valve Characterization and Tuning**).
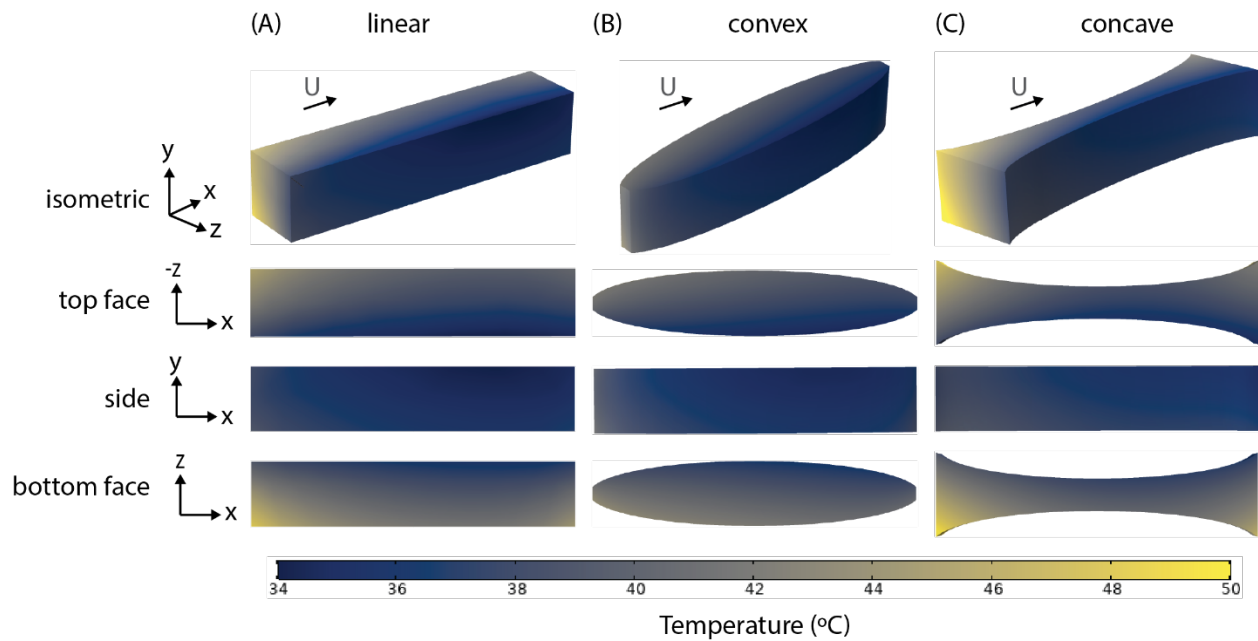
Figure 3.5 COMSOL simulation of valve heating.

Figures represent the valve domain of the model depicted in Figure 3.2 with varying valve geometries but constant volume (0.005 cm^3). After 120 seconds of simulated heating of the model, there is a several degree temperature gradient through the depth and length of (A) linear, (B) convex, and (C) concave shaped valves when convective and evaporative heat losses are included in the multiphysics model.
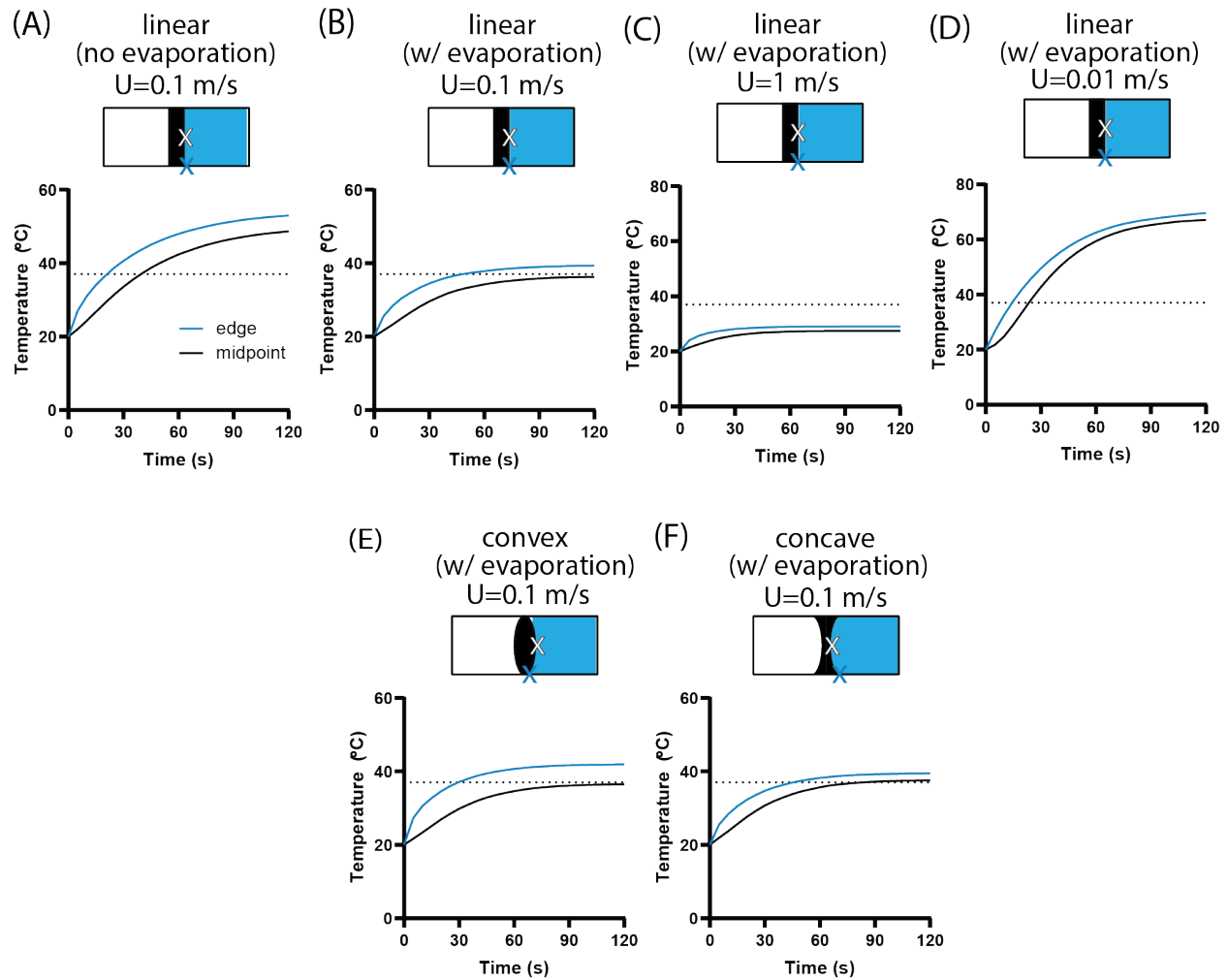
Figure 3.6 Simulated temperature difference between the midpoint and edge of wax valves.

The dotted line depicts the temperature when paraffin wax begins to melt. (A) When heat loss is only from convective heat transfer, there is a several degree difference in temperature between the edge and the middle of a linear valve on the bottom face. (B) When evaporative heat loss is included, the temperature difference reduces. (C) With greater convection, the wax never reaches the melting temperature. (D) With negligible convection, there is still a temperature difference between the middle and edge. (E) A convex valve has the greatest temperature difference while (F) a concave valve has the smallest temperature difference.

Interestingly, when both sources of heat loss are included, and the geometry of the valve is adjusted to either a concave or convex shape (with approximately the same volume as the linear valve), the temperature difference changes. As Figure 3.6E and F illustrates, the temperature difference between the edge and middle of a concave valve is approximately half that of a convex valve (2ºC and 4ºC, respectively). The experimental implication of this result is that the flow through a concave valve will likely yield a more even flow front than that of a convex valve. Moreover, the time to open a convex valve will likely be less than that of a linear or concave valve. Knowing that the time to open is influenced by the width of the valve (Figure 2.5), I plotted the temperature at the thinnest upstream region of the simulated valves (i.e. the edge of a linear and a convex valve and the middle of the concave valve). As Figure 3.7 illustrates, the thinnest region of a convex valve heats faster than that of a linear valve and a concave valve. The implication of this result is that a convex valve would likely open before a linear valve and a concave valve would take the longest to open.
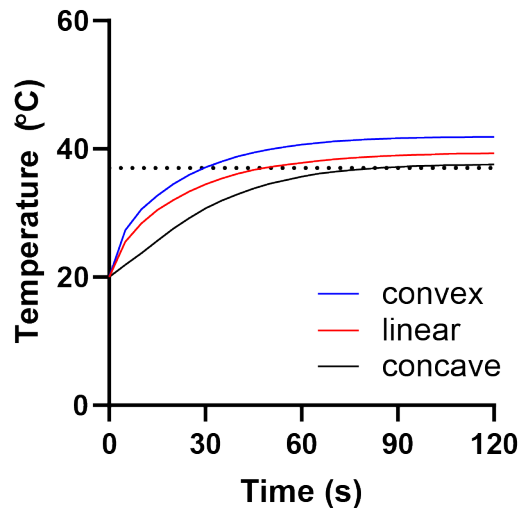
Figure 3.7 Simulated temperature at thinnest region of valve.

The thinnest regions of convex valves heat faster than linear and concave valves and would likely open first. Dotted line depicts temperature that paraffin wax begins to melt.

3.4. Future Directions

My model simplified several aspects of heated wax valves that can be addressed in the future. First, the ambient air flow stream is multi-directional. Even if the test strip is enclosed in a box, there will be natural convective air currents (much like in a cooking oven) that could influence the heat transfer. A future iteration of this model should account for more complex air flow. Additionally, I assumed a uniform heat source but both my preliminary results (demonstrating the influence of the orientation of a thin-film heater on valve opening, 3.3.2) and published results indicate that resistive heaters produce non-uniform heating.[103] By combining existing models of Joule-heating with my model, we could predict an orientation or resistive heater design that could yield the most uniform heat distribution through a valve.

I assumed a uniform distribution of wax through the depth of the membrane. However, my imaging results in Figure 2.4 indicate that there is less wax in the bottom face of the strip than on the surface. Assuming the pores along the bottom face are filled with air, which has a lower specific heat capacity than wax, then the temperature gradient through the depth of the valve will be greater than what my model demonstrated. In the future, a more accurate representation of the wax distribution in the pores could be modelled.

To improve the computation time of this model, the mesh should be adjusted. I defined a fine mesh at all domain boundaries and a free triangular mesh in the remaining domains. Adjusting the mesh to only be fine at boundaries between the wax and porous domains would speed up the computation.

The simulated heating of a wax valve indicates that the valve geometry will influence the time to open and the uniformity of heating. These results should be verified experimentally by preparing valves with linear, concave, and convex shapes and characterizing them as was done in **2.2.4 Closed-to-Open Valve Characterization and Tuning**. To explore implications of valve placement, the heat dissipation through the length of the membrane could be characterized. This would help inform where valves and heat sources should be located when performing heated assays adjacent to valves or when performing sequential actuation of multiple valves.

3.5. Conclusion

To identify factors that influence the non-uniform opening of a wax-ink valve, I created a 3D model that simulates the heating of a valve embedded into porous media. When imaging with an IR camera, I noted that evaporation caused a measurable temperature difference across the width of a nitrocellulose membrane. By including both evaporative and convective heat loss in a multiphysics model, I can discern a multi-degree temperature difference between the edge and middle of a simulated valve which can explain the non-uniform valve opening observed in Chapter 2. Minor adjustments to the valve, such as the geometry, could permit a more uniform flow past the valve. By continuing to finesse the model and explore other factors such as a non-uniform heat source or heat dispersion through the length of a test strip, the model could be used to predict the valve behaviour when implemented into a multi-step diagnostic test strip.

4. THERMALLY ACTUATED WAX VALVES FACILITATE IMPROVED PATHOGEN DETECTION ON LATERAL FLOW IMMUNOASSAYS

Parts of this chapter are reproduced from Ref. 110 and 111 with permission from the Royal Society of Chemistry.

4.1. Rationale

As discussed in **1.2.3 Paper as a low-cost diagnostic assay substrate**, LFIAs remain the most attractive rapid diagnostic platform but are limited by insensitivity for many biomarkers. Improving detection sensitivity requires improvement of the LFIA performance and/or pre-enrichment of the target. Bishop and colleagues recently analyzed opportunities to improve LFIA performance on a systems-level.[112] They aptly note that improvements to sample transport, reaction kinetics, or signal generation often degrade the attractive characteristics of LFIAs, such as minimal user steps and test autonomy. For instance, gold enhancement solutions have been demonstrated to improve LFIAs' positive test band intensities for easier detection but require the manual deposition of the enhancement solution at a precise time-point during the LFIA development.[79,93] The utility of such signal enhancement methods would be improved with automated delivery of reagents.

Even when LFIA assay improvements do retain usability characteristics, the sensitivity of the LFIA is fundamentally limited by the amount of analyte in a sample. Post-LFIA signal enhancement steps have been able to improve detection sensitivity 1000-fold,[113] although more commonly only 3- to 10-fold.[79,114] Conversely, pre-enrichment steps of analytes, such as nucleic acid amplification, can provide exponential improvement in sensitivity and could be combined with improvements in LFIA performance for even greater sensitivity. However, the complexity of manufacturing a device that both prepares a sample for nucleic acid amplification and performs the cyclical heating required for PCR often makes it prohibitively expensive for low-resource settings.[115] Moreover, the enriched sample usually has to be manually deposited to a LFIA, introducing user-error, assay complexity, and potential for cross-contamination with other samples. To address these shortcomings, recent efforts have been focused towards developing integrated sample-to-answer nucleic acid analysis devices that can be used by minimally-trained personnel.[116,117] While these integrated nucleic acid analysis devices minimize user steps and costs,

RNA remains a challenging target to analyze from whole blood samples because of blood's inhibition of both nucleic acid amplification assays and LFIAs.

In this chapter, I demonstrate how wax-ink valves facilitate improved pathogen detection on LFIAs and do not interfere with downstream assay performance. As an initial proof-of-concept of wax valves facilitating test autonomy, I modify a standard single-step LFIA into a multi-step LFIA that delivers gold enhancement solution semi-automatically to the test band. Next, I utilize multiple wax-ink valves to constrain nucleic acid amplification within a porous membrane and then automatically release the amplification products to a downstream LFIA for detection of HIV viruses in whole blood.

4.2. Materials and Methods

4.2.1. Integration with multi-step LFIA.

To demonstrate the application of this wax-ink valve in paper-based diagnostic assays, I modified a standard single-step LFIA into a multi-step LFIA that delivered gold enhancement solution to the test band. Commercial Rapid Bacteria Pool Water Test strips were modified from dip-strips into LFIAs by rehydrating the conjugates with 40 μl of DI water for 10 minutes. Rehydrated conjugates were deposited onto 4 by 10 mm strips of Fusion5 conjugate pad (GE Healthcare) and dried overnight in ambient conditions. The sample pad of the pool test strips was carefully removed and replaced with the fabricated conjugate pad. Fabricated LFIAs were further modified, as shown in Figure 4.1, by adhering a previously described 4 by 20 mm closed valve in nitrocellulose membrane downstream of the conjugate pad and perpendicular to the test membrane with pressure sensitive adhesive (Dura-Lar) and stacking a 4 by 10 mm strip of Fusion5 upstream of the valve. Lastly, the thin-film heater was adhered to the backside of the valve with pressure sensitive adhesive (double-sided Scotch tape, 3M) directly below the valve.
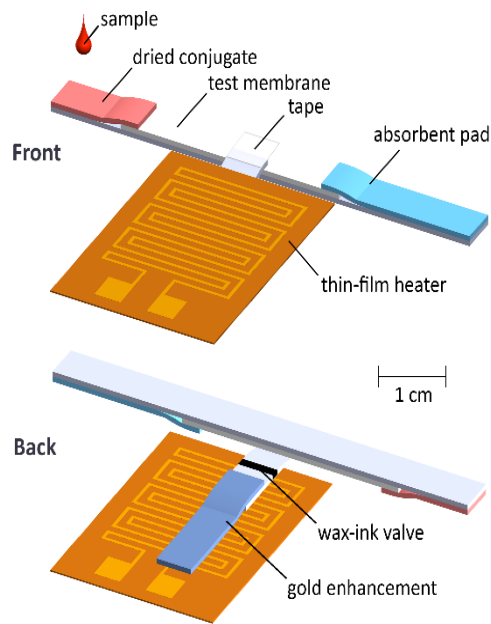
Figure 4.1 Schematic of a multistep assay enabled by integrating wax-ink valve into a traditional lateral flow immunoassay.

Forty microliters of *E. coli* culture diluted in DI water was pipetted onto the conjugate pad of the fabricated LFIA. Forty microliters of GoldEnhance LM solution (Nanoprobes) with 0.015% Tween-20 (Sigma-Aldrich) was simultaneously applied to the Fusion5 pad upstream of the closed valve. After 20 minutes of the *E. coli* sample wicking through the test strip, 0.21 amperes of current was applied to the thin-film heater for 50 seconds to open the valve and release the enhancement solution into the test strip. An additional set of tests strips was left at ambient conditions without actuating the valve and preventing the enhancement solution from wicking through the test strip. All test strips were scanned 40 minutes after initial sample application on an Epson V850 Pro scanner (Long Beach, CA). Test band intensities were analyzed with a custom MATLAB script.

4.2.2. Integration of nucleic acid amplification with LFIA.

To demonstrate the wax-ink valves' utility in assays requiring greater incubation time and sophistication than the previously described multi-step LFIA, I sought to integrate paper-based nucleic acid amplification with a detecting LFIA. With other members of the Linnes Lab, I designed a sample-to-answer device (Microfluidic Rapid and Autonomous Analysis Device (microRAAD)) for detection of HIV viral nucleic acid amplicons on a downstream LFIA. The microRAAD for HIV detection is composed of a reusable temperature control circuit and silver ink resistive heating elements (designed by Orlando Hoilett and Kristin Byers as described in [111]) and a single-use laminated microfluidic paper analytical device (μPAD), all contained in a plastic housing (Figure C.2). The base of the plastic housing was designed in SolidWorks and 3D printed on a Fortus 380c printer (Stratasys, Eden Prairie, MN). The 0.08" thick acrylic lid of the housing (model #11G0670A, Shape Products Menomonie, WI) and components of the single-use μPAD (Figure 4.2) were designed in Adobe Illustrator and cut with a CO_2 laser (VLS 3.5, Universal Laser Systems, Scottsdale, AZ) (settings listed in Table C.2). Valve strips were prepared by printing 1.25 mm wide lines of solid wax-ink (Black ColorQube ink, Xerox, Norwalk, CT) onto cellulose membranes (Chr1, GE Healthcare, Pittsburgh, PA) using a Xerox ColorQube 8570 (Norwalk, CT). Membranes were then heated for twelve minutes at 85°C in a table-top oven (VWR, Radnor, PA) and cut into strips with the laser cutter to create closed valve strips. Commercially available LFIAs were modified for microRAAD by cutting off the sample pad. PET squares were sterilized with 70% ethanol. Once prepared, all components were hand assembled (Table C.1 and Figure C.2) and laminated with pressure sensitive Self-Seal adhesive (GBC, Lake Zurich, IL) to minimize evaporation during the assay.
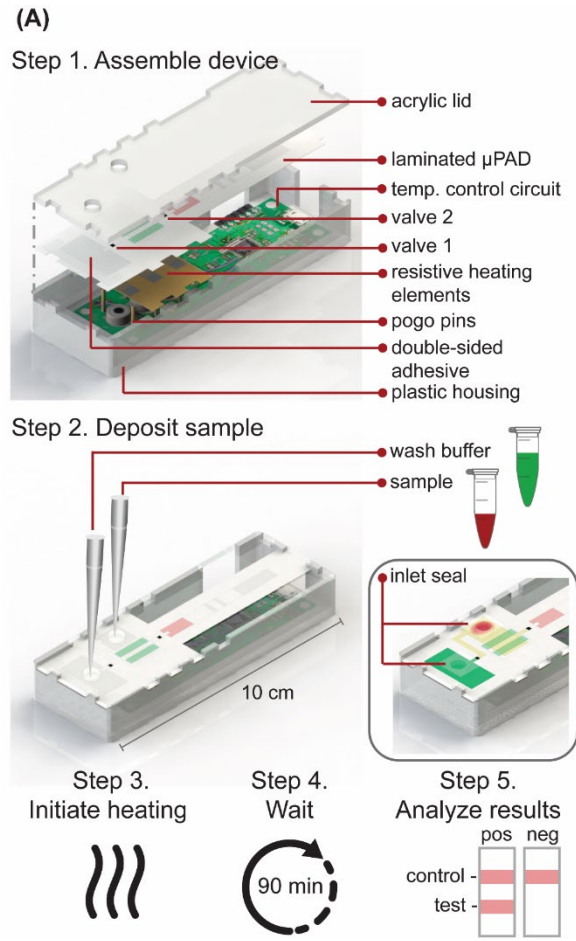
Figure 4.2 Schematic of microRAAD for HIV testing.

(A) In work flow, user 1) assembles consumable microfluidic paper-based analytical device (µPAD) into plastic housing with reusable resistive heating elements and temperature control circuit, 2) deposits sample and wash buffer into inlets and seals with tape to minimize evaporation, 3) initiates heating by connecting to phone, 4) waits 90 minutes for automated fluid delivery and sample incubation in µPAD, and 5) analyzes results of lateral flow immunoassay. (B) Photo of microRAAD connected to phone to power the temperature control circuit.

Seventy-five (75) μL of prepared RT-LAMP master mix (optimized by Kaisa Ejendal and Taylor Moehling as described in [111]) or rehydrating mixture containing HIV-1 virus (AccuSpan Linearity Panel, SeraCare Life Sciences, Milford, MA) (at a final concentration of 4×10^6 virus copies/mL of reaction volume) were loaded into the sample inlet of the μPAD and sealed with a 1x1 cm square of Self-Seal prior to assembling the μPAD into the plastic housing with the temperature control circuit. This method was used to minimize contamination between experiments, however, I also verified that the sample can be added to the sample inlet once the μPAD is assembled in the plastic housing, which is how I anticipate the device would be used at the point of care.
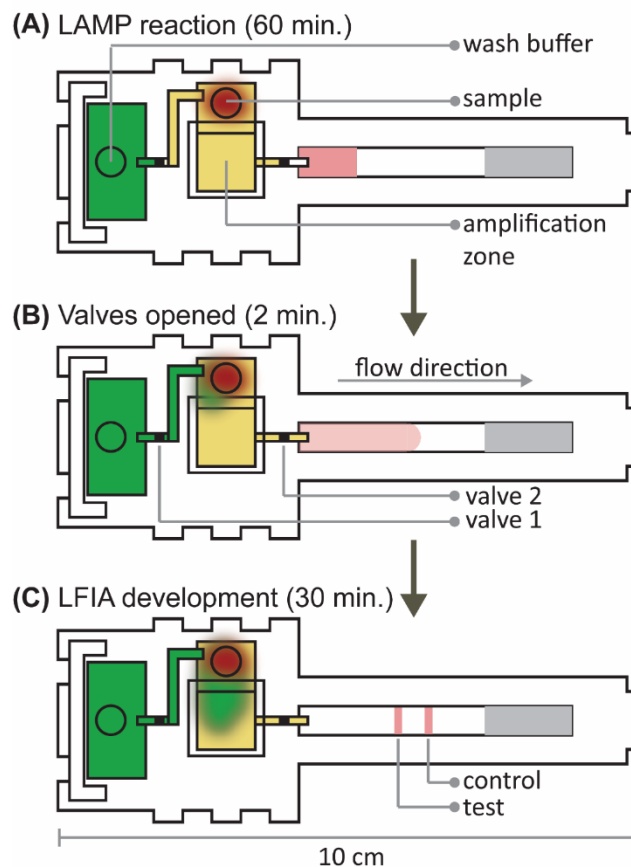
Figure 4.3 Schematic of fluid travel through microRAAD.

(A) The wash buffer (green) is constrained from flowing to the amplification zone and the sample (red blood cells and yellow plasma) is constrained from flowing to the LFIA by closed valves. (B) Upon thermally actuating the valves, wash buffer is released to the amplification zone and the RT-LAMP products migrate to the LFIA for (C) test band development.

The assembled microRAAD was then loaded with wash buffer and subjected to localized heating of the amplification zone and valves. When testing whole blood samples spiked with HIV-1 virus, 1.2 µL of 2.5×10^5 virus copies/µL HIV-1 was mixed with 12 µL of human whole blood collected in sodium citrate (Innovative Research, Novi, MI) and loaded into the sample inlet, followed by a 61.8 µL addition of rehydrating mixture (final concentration of 4×10^6 virus copies/mL of reaction volume). The loaded µPAD was then adhered to the acrylic lid with double-sided adhesive at the wash inlet. Resistive heating elements were adhered to the backside of the µPAD, aligned with the two valves and amplification zone, and faced such that the silver traces would contact the pogo pins of the temperature control circuit inside the plastic housing. Two plastic brackets were slid over the acrylic lid and plastic housing to ensure proper contact within microRAAD. Finally, 130 µL of green food coloring in water solution for visualization of flow were added to the wash inlet and sealed (Figure 4.2). Heating was initiated via the serial interface between the computer and the temperature control circuit: 1) 65 °C for the middle resistive heating element to allow amplification for 60 minutes and 2) 80 °C for the outer resistive heating elements to actuate the valves for 2 minutes. After 30 minutes of development (1.5 hours after initiating the amplification heating), the LFIA was imaged using a desktop scanner for analysis (Epson, Suwa, Japan).

4.3. Results and Discussion

4.3.1. Integration with multi-step LFIA.

Despite previously demonstrating that applying 0.21 amperes for 15 seconds was sufficient to release liquid through a closed 0.1 mm valve, no amount of heating was able to release gold enhancement solution alone through the 0.1 mm valve (data not shown). The surface tension of the gold enhancement solution was likely higher than that of the dyed water used in the characterization experiments. However, by adding 0.015% of Tween-20 to the gold enhancement solution, the closed 0.1 mm valve was able to both block enhancement solution passage for 20 minutes and, upon 0.21 amperes of current for 35 seconds, release the enhancement solution into the LFIA. Additives such as surfactants altered the valve characteristics, presumably by lowering the surface tension of the fluid flowing through the valve. This offers additional valve tunability beyond the valve width and heating time, but also requires that valves be further optimized for

reagent composition when applied to paper-based assays. Statistical analysis of the enhanced and standard LFIA test band intensities demonstrated that 2.2E5 *E. coli* cells were detectable on the LFIAs as compared to the respective negative control bands (Figure 4.3A-B). The enhanced strips were also detectable by eye with a statistically significant, 6-fold greater intensity than the standard strips with both 2.2E5 and 2.2E4 *E. coli* cells (Figure 4.3B). As seen in previously enhanced LFIAs,[79,93] the addition of gold enhancement solution increased intensity in the *E. coli* positive assays, but also increased background intensity. Additional optimization of the enhancement solution volume and timing could further improve the detection limit of the multistep LFIA. While the proof-of-concept required the user to turn on and off the power supply, the multistep assay could be easily modified into a fully automated, single-user step assay with the addition of a simple electronic timer. Nevertheless, the proof-of-concept demonstrated that a wax-ink valve can improve an existing LFIA into a tunable, semi-automated, multistep LFIA for enhanced detection.
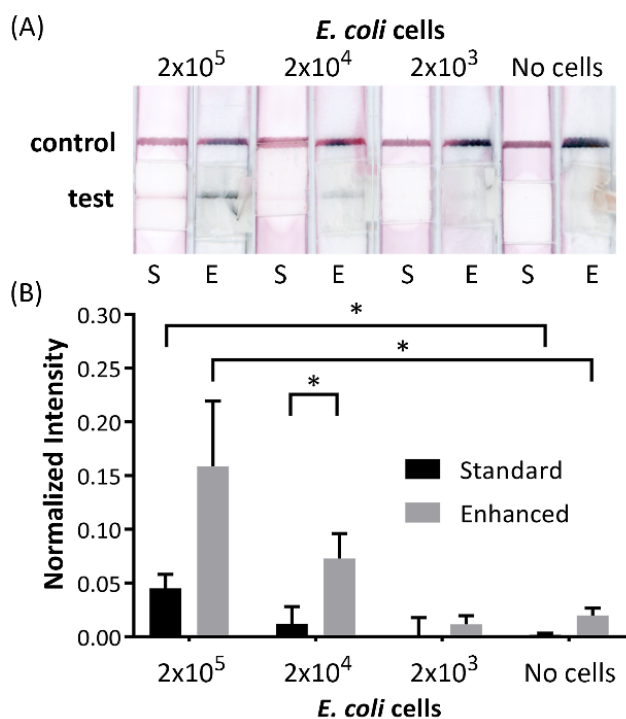
Figure 4.4 Valve enabled multistep assay.

(A) Images of valve enabled multi-step assay, as shown in Scheme 1. Gold enhancement of LFIA improves detection of *E.coli* cells compared to single-step LFIA. (B) Normalized intensity of test lines in (A). Gold enhancement of LFIA (E) improves visible signal intensity up to 6x as compared to standard LFIA (S). * indicates $p < 0.05$, n = 3

67

4.3.2. Integration of nucleic acid amplification with LFIA.

µPAD component selection

I selected several components of the µPAD by experimentally verifying their functionality described in product specifications (i.e. the LFIA captured FITC-tagged amplification products as specified and the glass fiber had a high wicking and release relate). I prepared valves in cellulose chromatography paper to leverage its fast flow rate and ensure a rapid sample analysis. I selected the MF1 blood separation membrane because it separated red blood cells from plasma in the least amount of membrane surface area as compared to other blood separation membranes and thus would ensure microRAAD's portability (Figure C.3 and Figure C.4). I selected PES for the nucleic acid amplification because I found it was the only membrane that did not inhibit LAMP (Figure C.5); its performance was similarly characterized by previous results in the literature[118] and further tested in the Linnes Lab.

To minimize evaporation of the sample during the assay incubation, I laminated the µPAD components with SelfSeal. The transparency of SelfSeal allowed us to observe the fluid migration and visually interpret LFIA results with minimal delamination during the nucleic acid amplification assay at the optimal amplification temperature of 65°C (Figure C.6). To ensure that no capillary flow leaks between the membranes and the SelfSeal, I verified that the flow rates of sealed and unsealed membranes were equivalent (data not shown). However, I did find SelfSeal, like many materials tested (Figure C.5), inhibited LAMP amplification. Therefore, I sandwiched the PES amplification membrane with squares of polyethylene terephthalate (PET), thus preventing the SelfSeal from contacting the PES, to ensure that amplification was not inhibited. In the future, a lamination product more robust to high temperatures and long-term storage should be used. As described next, the sample and wash volumes are critical for proper fluidic transport between assay zones; when the µPAD was not resealed immediately before being used, liquid would evaporate from the µPAD and prevent proper fluid transport. Given the plethora of PCR sealing tapes available in the market, I am confident a more adhesive material could be identified but the increased material cost should be considered.

Integration of microRAAD

I verified flow in microRAAD with 2% solutions of water soluble colored dye solutions (McCormick, Sparks, MD) deposited into the sample and wash inlets and then heated the amplification zone and valves. This initial testing indicated 130 µL of wash buffer and 75 µL of sample were required. With too little volume, there was an insufficient pressure gradient to drive flow past the opened valves, while too much volume caused the fluid to prematurely leak past the valves. The wash solution is necessary to sufficiently drive the RT-LAMP amplicons from the PES amplification zone into the LFIA for detection. Initial fluidic designs transported the wash solution directly to the PES, however, given the PES's small pore size and slow wetting, this caused frequent "short-circuiting" of the wash to the LFIA in which the wash solution would flow around the PES membrane and directly to the LFIA. By directing the wash through the MF1, rather than to the PES directly, I ensured that amplicons in the PES migrated to the LFIA before the wash (Figure 4.2 and Figure C.8). Moreover, I verified that no capillary leaks occurred between the membranes and lamination by confirming the flow rates of sealed and unsealed membranes were equivalent (data not shown).

As was the case in the multi-step enhanced LFIA, the surfactant presence in the nucleic acid amplification buffer (containing Tween-20 and TritonX-100) altered the valve characteristics and caused sample to prematurely flow past the 1 mm valves previously determined to block fluid. 1 mm valves leaked wash buffer, diluting the amplicons and potentially decreasing assay sensitivity. By increasing the valve widths to 1.25 mm, I verified that the valves constrained the wash buffer from the amplification zone. I had previously determined that only 41ºC is required to open wax-ink valves prepared in chromatography paper (**2.2.4 Closed-to-Open Valve Characterization and Tuning**), however, here I subjected the valves to 80ºC to accelerate the melting process and thereby increase the speed of valve opening. Upon initiation of valve heating, the green wash buffer flowed past valve 1 to the MF1 and the heated sample flowed past valve 2 into the LFIA portion of the µPAD. Within 5-10 minutes of the valves opening, test and control bands were consistently observed on the LFIAs and quantification, in Figure C.7, revealed strong test band intensities.

The 65ºC heating of the nucleic acid amplification region did cause evaporation of the sample to the inner surface of the laminating seal though no fluid was observed to pass the valves prematurely (colored dye solutions were used to confirm this observation). I believe that the 65ºC

heating diffused sufficiently to prevent premature valve opening. However, when the heating board malfunctioned and heated beyond 65ºC (sometimes as much as 100ºC), valves sometimes opened too early. Assays requiring higher heating (such as for cell lysis or enzyme deactivation) may require additional tuning of valve widths and spacing from heating regions. A combination of heating models in COMSOL and experimental validation could inform the optimal valve geometries and spacing for future assay needs. When the device functioned as designed, the LFIAs yielded visible test and control lines, indicating that solutions even as viscous and complex as long nucleic acid amplicons are able to pass the opened wax-ink valves (Figure 4.4).

To verify the amplification functionality of microRAAD, I initiated the automated detection using 21-day dried RT-LAMP reagents and rehydrating buffer containing HIV-1 virus osmotically lysed in water. Samples containing as few as 3×10^5 virus copies/reaction resulted in unequivocally positive test bands and samples containing no template (0) yielded negative test results (p-value < 0.05) (Figure 4.4B). The test band intensity at a concentration of 3×10^5 virus copies/reaction using the dried reagents in microRAAD was comparable to the test band intensity of the same concentration in a tube reaction with the dried reagents.

Finally, I performed the detection in the integrated microRAAD using 21-day dried amplification reagents and HIV-1 virus in whole blood. As expected and seen in Figure 4.4A, the red blood cells remained in the MF1 directly below the sample inlet while the remaining plasma and buffer solution with virus migrated to the PES for amplification. Following amplification, I visually observed positive test bands on the LFIAs within 5-10 minutes after valves opened. There was a statistically significant difference between the test band intensity of the 3×10^5 virus copies/reaction compared to the negative control (0) (p-value < 0.01) (Figure 4.4A and C). Notably, the sensitivity using microRAAD for HIV-1 viral detection in blood using dried reagents is comparable to the sensitivity of standard tube reactions with similar conditions. Previous groups have similarly reported only 5 to 10-fold reductions in sensitivity when translating manual assays into automated sample-to-answer devices.[24,116,119] Liu *et al.* designed a device to detect viral RNA from oral fluid samples in real time down to 12.5 virus copies/reaction, however, viral lysis is required before sample addition and is followed by four more manual steps prior to initiation of the RT-LAMP assay.[120] Damhorst *et al.* developed a microfluidic chip for blood cell lysis and modified a smartphone for real-time detection of HIV-1 virus with an LOD of 1.7×10^4 virus copies/reaction.[121] However, the user is required to transfer the lysed blood and freshly prepared

70

RT-LAMP reagents to the reaction chamber for amplification which opens possibilities for sample contamination and bloodborne pathogen transmission.[121] Even though this platform is 10-fold more sensitive than microRAAD, I believe that the full automation of microRAAD, which reduces sample handling and exposure to bloodborne pathogens, makes it an advantageous system for rapid HIV testing at the POC. This proof-of-concept demonstrates wax-ink valves' utility in translating traditional bench-top assays such as nucleic acid amplification into automated paper-based devices.
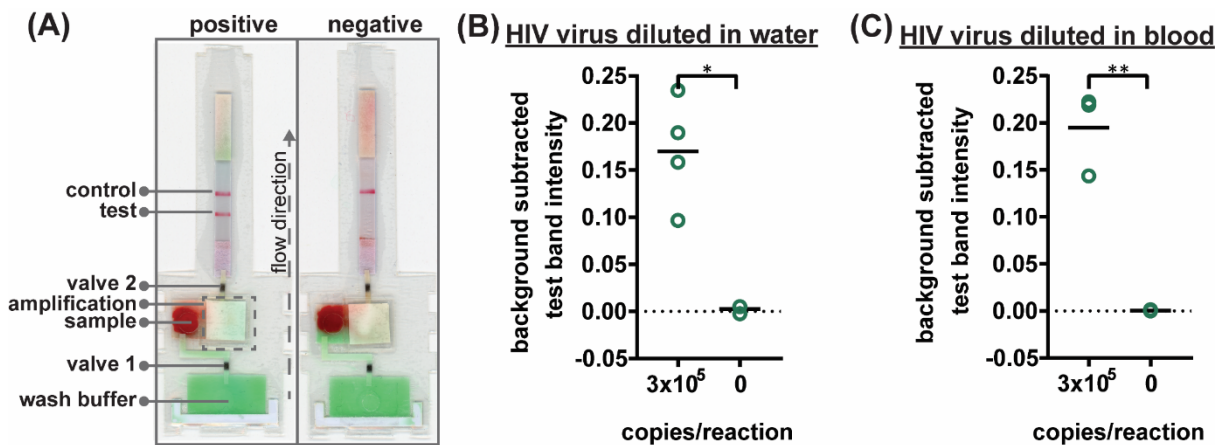
Figure 4.5 Detection of HIV virus diluted in whole blood on microRAAD with reagents dried for 21 days.

(A) Representative µPADs imaged 90 minutes after blood (with and without HIV virus) deposited into microRAAD's sample inlet. After capillary migration of HIV from sample inlet to amplification zone and subsequent heating, the valves are automatically heated, releasing solution to LFIA for detection. As few as 3 x 10^5 HIV (B) osmotically lysed virus copies in rehydrating mix alone or (C) intact virus in rehydrating mix with 12 µL of blood are detectable by microRAAD prepared with RT-LAMP reagents dried for 21 days. n=4 (B) and n=3 (C), replicates indicated by each circle; * indicates $p \leq 0.05$ and ** indicates $p \leq 0.01$.

4.4. Future Directions

The surface tension of the solution passing through the valves became a critical parameter that dictated whether the solution would pass through valves prematurely or never. Future experimental studies could correlate solution viscosity and surface tension to valve passage time and better inform future valve designs for other assay applications.

In the future, the spatial location of the valves relative to other heating regions should also be considered. While the heat from the nucleic acid amplification step in microRAAD apparently dissipated sufficiently, assay steps requiring higher heat may prematurely open wax valves. Extending the computational modeling performed in Chapter 3 to include the heat dissipation in various materials could inform optimal valve placement.

While some enhancement solution and nucleic acid amplification products passed through the opened valves of both applications, inadequate melting may have prevented efficient passage. Experimental studies, such as microscopy of simulant particles, could verify passage efficiency.

Lastly, diagnostic assays require rigorous stability testing before implementation and regulatory approval. An accelerated stability test at elevated humidity and temperature should be performed in the future to validate the robustness of stored valves. The composition of the valves makes them unlikely to degrade over time, however, they may be sensitive to mechanical stresses such as bending. Stress testing would inform optimal storage conditions and packaging of diagnostic assays containing these valves.

4.5. Conclusion

I have demonstrated the utility of wax valves for improving pathogen detection on LFIAs by leveraging their controlled fluid release to enhance the detection limit of a traditional LFIA and to facilitate a sample-to-answer nucleic acid detection device. These wax-ink valves enable increased complexity of fluid operations on paper platforms by permitting sustained reaction incubations times, requiring minimal user involvement, and maintaining low fabrication costs without obstructing downstream chemistries. Notably, both demonstrations required that the valves be modified from initial designs determined in Chapter 2. Nevertheless, in this chapter, I demonstrate the utility of wax valves to facilitate multi-step sample analysis with LFIA detection.

5. DEVELOPMENT OF TOE-HOLD MEDIATED STRAND DISPLACEMENT PROBES FOR DETECTING NUCLEIC ACID IN COMPLEX MATRICES

5.1. Rationale

Sensitive and specific detection of pathogens via nucleic acid amplification is currently constrained to laboratory settings and portable equipment with costly fluorescent detectors. Nucleic acid-detecting lateral flow immunoassay strips (LFIAs) offer a low-cost visual transduction strategy at points of need. Unfortunately, these LFIAs frequently detect amplification byproducts that can yield spurious results which can only be deciphered through statistical analysis. To improve users' instrument-free interpretation of paper-based diagnostics, I sought to improve the molecular capture mechanisms that more specifically detect amplification products.

Isothermal loop-mediated amplification (LAMP) is one method appropriate for the point-of-need because it rapidly amplifies dilute template DNA from crude samples and requires minimal equipment to perform. Primers are commonly tagged for post-amplification detection on LFIA's, risking capture of primer dimers and spurious amplicons.[24,47,48] The false positive results endemic to primer-based detection are typically mitigated by redesigning the primer sets or reducing reaction time, which also decreases assay sensitivity. Target specific detection of LAMP amplicons has been achieved with hybridization of incorporated primers,[49] polymerase-mediated strand displacement of duplexed primers,[50] or toehold-mediated strand displacement events,[51] but all have required an excited fluorophore and fluorescent reader for signal transduction. Du et al. have alleviated the need for a lab-based fluorescent reader by coupling target-specific strand exchange reactions to a home-pregnancy test, an inexpensive and ubiquitous lateral flow immunoassay (LFIA) strip, for visual detection.[52] However, multiple additional user steps and reagents to complete this signal transduction complicated the detection and could increase interpretation error. To minimize user steps, I aimed to leverage the specificity of a strand displacement probe to tag amplified nucleic acids in a one-pot reaction mixture.

To ensure that combining strand displacement with LAMP (SD-LAMP) yields LFIA test band intensities that are interpretable without additional instrumentation, I evaluated the unaided reading of LFIA results by human subjects. By defining test band intensities required for instrument-free interpretation, I can inform future LFIA design and indicate when LFIAs are or are not an appropriate detection assay.

As proof-of-concept, I integrated tagged strand displacement probes into LAMP assays for the detection of *Escherichia coli* and *Vibrio cholerae*. Given that complex sample matrices have been found to inhibit amplification assays such as PCR, I investigated whether pond water (a common matrix for both pathogens) or human blood (in the case of *E. coli* as a sepsis-causing pathogen) similarly limit the utility of SD-LAMP visualization on LFIAs. A mastermix of LAMP reagents, strand displacement probes, and bacteria were isothermally heated to simultaneously lyse bacteria and amplify and tag the target DNA. After an hour of heating, reaction products were deposited onto a commercial LFIA which yield colorimetric bands within 30 minutes to indicate the presence or absence of target DNA. The test band intensities were compared to the threshold intensity values determined by the human subject study to determine the efficacy of SD-LAMP. Demonstrating the rapid, sensitive, and accurate detection of pathogenic bacteria from complex sample matrices on paper test strips aids the control of waterborne and bloodborne infectious diseases.

5.2. Materials and Methods

5.2.1. Bacterial Cell Culture

E. coli strain DH5α (NEB, Ipswich, MA) and *V. cholerae* strain N16961 (generously donated by Dr. Afsar Ali at the University of Florida) were grown overnight at 37°C at 350rpm (Thermo Fisher, Waltham, MA) in lysogeny broth (LB) media. Cultures were diluted in LB media to an OD600 (Ultrospec 10, Biochrom, Cambourne, UK) of 1.0, representing 5.5×10^9 cells/mL of *E. coli* or 7.0×10^9 cells/mL of *V. cholerae* as determined by fluorescence microscopy of serially diluted cells or counting colony forming units of serially diluted cells, respectively.

5.2.2. Reagents

Oligonucleotide primers and probes targeting *E. coli malB* and *V. cholerae ctxA* genes (Table D.1) were ordered from Integrated DNA Technology (IDT, Coralville, IA) and are summarized in Table D.2. Oligonucleotides were resuspended in DNase/RNase-free DI water. Note that LF and LB primers are tagged with either 6-carboxyfluorescein (FAM) or biotin for capture on commercial lateral flow immunoassay strips. Local pond water was collected and then stored at 4°C until use. Citrated human whole-blood (cat. no. IPLA-WB1, Innovative Research, Novi, MI) was separated into plasma by centrifugation at 1,000 x g for 10 minutes at 4°C (Eppendorf Centrifuge 5424R, Hamburg, Germany). Whole blood was stored at 4°C and used within 2 weeks; plasma was stored at -20°C until use.

5.2.3. Standard LAMP Reaction of *E. coli*

Five microliters of *E. coli* culture diluted in LB media, pond water, or plasma was added to 20 µL reaction mixtures containing 0.3 µM each F3 and B3 primers, 2.4 µM each FIP and BIP primers, 1.2 µM each LF and LB primers, 1100 mM betaine, 1.4 mM dNTPs, 1x Isothermal Buffer, and 8U Bst 2.0 polymerase. Reactions were incubated at 65°C for 1 hour followed by a 1 minute 95°C denaturing step to prevent further amplification (7500 RT-PCR System, Applied Biosystems, Foster City, CA) and then kept at 4°C until analyzed.

5.2.4. Standard LAMP Reaction of *V. cholerae*

Five microliters of *V. cholerae* culture diluted in LB media or pond water was added to 20 µL reaction mixtures containing 0.2 µM each F3 and B3 primers, 1.6 µM each FIP, BIP, LF, and LB primers, 800 mM betaine, 1.4 mM dNTPs, 1x Isothermal Buffer, and 8U Bst 2.0 polymerase. Reactions were incubated at 65°C for 1 hour followed by a 1 minute 95°C denaturing step to prevent further amplification using the 7500 RT-PCR System (Applied Biosystems, Foster City, CA) and then kept at 4°C until analyzed.

5.2.5. SD-LAMP Probe Design

Strand displacement probes were designed with Dr. Sancheeta Bhadra of University of Texas at Austin to bind to the forward loop region of the *malB* and *ctxA* gene targets following previously

published design considerations,[51] in order to detect only the target amplification products (Table D.1). We aimed for a free energy change of -18 kcal/mol at the probes' duplex region, which constrained both probes' binding sites to the location of the forward loop primers. Probes were tagged with 6-FAM and pre-annealed to shorter complementary strands tagged with a quencher for real-time amplification verification (data not shown). All 3'-OH groups were blocked against polymerization by including a 3' inverted dT group. The short, single stranded regions in the FAM-labeled probe strands were designed to act as a toehold to initiate strand displacement (Figure 5.1A) and bind to the amplicon target. The tagged amplicon can then be visualized on an LFIA (Figure 5.1B).

5.2.6. SD-LAMP Reaction of *E. coli*

A stock solution of strand displacement probe was prepared by annealing 1 µM of FAM tagged oligonucleotide to 5 µM of quencher tagged oligonucleotide in Isothermal Buffer at 95°C for 1 minute followed by 0.1 °C/second cooling to room temperature. Five microliters of *E. coli* culture diluted in LB media, pond water, or plasma and 1.25 µL of prepared probe was added to 18.75 µL reaction mixtures containing 0.3 µM each F3 and B3 primers, 2.4 µM each FIP and BIP primers, 1.2 µM LB primers, 1100 mM betaine, 1.4 mM dNTPs, 1x Isothermal Buffer, and 8U Bst 2.0 polymerase. Reactions were incubated at 65°C for 1 hour followed by a 1 minute 95°C denaturing step to prevent further amplification and then kept at 4°C until analyzed.

5.2.7. SD-LAMP Reaction of *V. cholerae*

A stock solution of probe was prepared by annealing 1 µM of FAM tagged oligonucleotide to 5 µM of quencher tagged oligonucleotide in Isothermal Buffer at 95°C for 1 minute followed by 0.1 °C/second cooling to room temperature. Five microliters of *V. cholerae* culture diluted in LB media or pond water and 2.5 µL of prepared probe was added to 17.5 µL reaction mixtures containing 0.2 µM each F3 and B3 primers, 1.6 µM each FIP, BIP, and LB primers, 800 mM betaine, 1.4mM dNTPs, 1x Isothermal Buffer, and 8U Bst 2.0 polymerase. Reactions were incubated at 65°C for 1 hour followed by a 1 minute 95°C denaturing step to prevent further amplification and then kept at 4°C until analyzed.
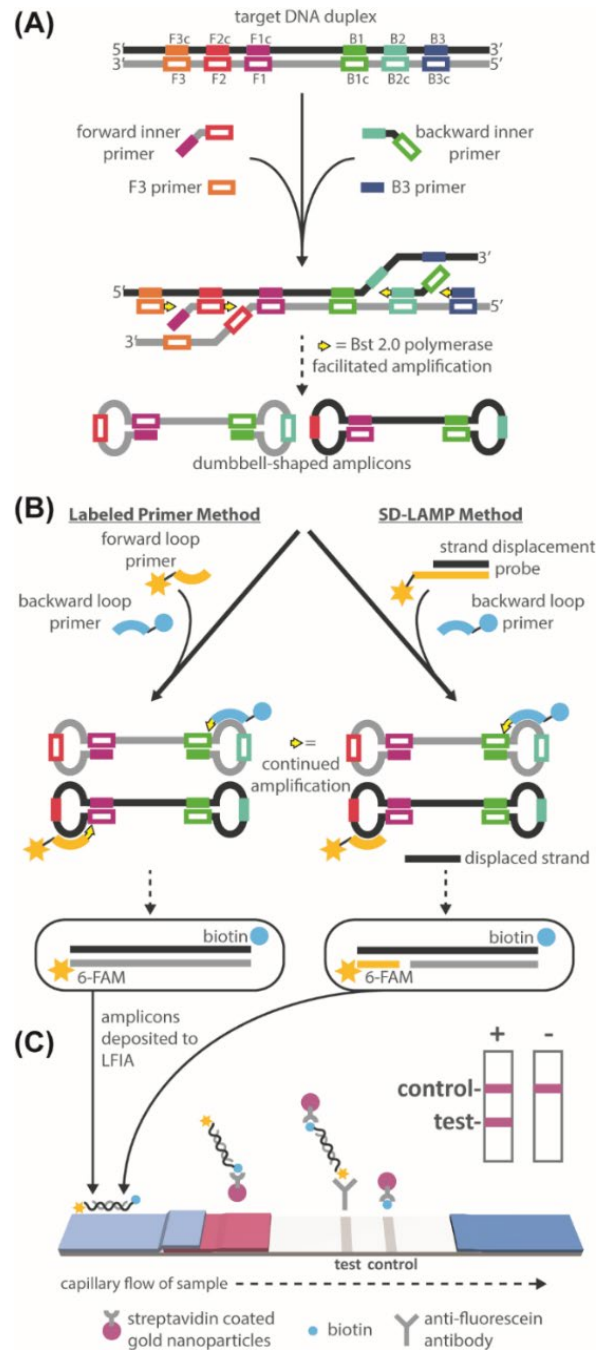
Figure 5.1 Schematic of standard LAMP and SD-LAMP reactions and their subsequent LFIA detection.

(A) The non-cyclic step of both reactions in which F3, B3, and inner primers bind to a double-stranded target sequence and polymerase generates dumbbell-shaped products. (B) Dumbbell-shaped products enter the cyclic amplification step during which loop primers accelerate amplification. Products can be labeled by either standard tagging of each loop primer or by SD-LAMP, which uses one labeled loop primer along with a tagged strand displacement probe that hybridizes to the amplicons' loop region. (C) Labeled amplicons visualized on a standard LFIA.

5.2.8. Gel Electrophoresis Characterization and LFIA Detection

Ten microliters of reaction mixtures were loaded with an additional 2 µL of 6x Purple Loading Dye (NEB, Ipswich, MA) into a 2% agarose gel containing ethidium bromide and were run at 100-115 V for 45 minutes. Ten microliters of FastDNA ladder was used as a size standard. The resulting gels were imaged with a 15 second exposure (c400, Azure Biosystems, Dublin, CA). Ten microliters of reaction mixtures were mixed with 40 µL of commercial LFIA wash buffer and pipetted onto a fluorescein capturing lateral flow immunoassay (cat. no. D003-03, USTAR Biotechnologies, Hangzhou, China). The FAM and biotin tagged nucleic acid amplification products are expected to complex with the streptavidin-conjugated nanoparticles present in the LFIA's conjugate pad. This complex flows downstream to the test lines where it will be captured by immobilized anti-fluorescein antibodies. Remaining streptavidin-conjugated nanoparticles will be captured by immobilized anti-streptavidin antibodies. The accumulation of visible nanoparticles at the test and control lines will therefore indicate a positive (2 lines) or negative (1 line) result.

5.2.9. Statistical Analysis and Quantification

All strips were scanned at least 30 minutes after initial sample application on an Epson V850 Pro scanner (Long Beach, CA) to allow tests to dry. Test band intensities were analyzed with a custom MATLAB script that averages the grey scale pixel intensity (to maximize signal-to-noise) and subtracts out average background signal 25 pixels below the test band. The resultant "background subtracted test line intensity" was then calculated as $I_{background\ subtracted} = \frac{I_{raw} - I_{background}}{0 - I_{background}}$ where 0 represents the lowest possible pixel intensity (i.e. black). Computationally, this yields a much greater dynamic range than physically possible given the saturation limitation of nanoparticles.[123] To determine the limit of detection of *E. coli* and *V. cholerae*, 4 test strip replicates from each solution's starting dilution were analyzed for statistical significance (Figure D.1, Figure D.2, Figure D.3, and Figure D.5 contain the replicate gels and LFIA strips). The test band intensities were compared to the averaged LFIA experimental negative control test band intensities using a Dunnett's test with an alpha set to 0.05.

5.2.10. Human Interpretation of LFIA Test Bands

To determine LFIA test bands' visible threshold for positive interpretation (independent of experimental negative control test band intensities), 18 volunteers between the ages of 18 and 44 years of age with no self-described vision impairments, were asked to evaluate 10 test strips of varying test band intensities (Figure 5.3), three times each and in varying lighting conditions (indoors, outdoors in sun, and outdoors in shade, amounting to 54 distinct observations). The evaluation study was performed in accordance to Purdue University's Human Research Protection Program. I performed a two-way ANOVA to evaluate confounding effects of test strip or and lighting conditions on test strip order. A Fisher's Exact Test was used to determine whether previous instruction on reading LFIAs (e.g. in a classroom or previous research setting) affected volunteers' interpretation.

5.3. Results and Discussion

5.3.1. Detection of Standard LAMP Amplicons on LFIAs.

My initial attempt to capture labeled LAMP amplicons on LFIA strips followed previously published methods for detection of other LAMP amplicon targets using labeled primers, but yielded both true positives that had only faint positive test bands as well as false positive results. I tagged the loop primers (forward loop primer with FAM; backward loop primer with biotin) of previously reported LAMP primers designed to amplify the *malB* gene of *E. coli* (Table D.1).[124] I heated the amplification reactions with serial dilutions of *E. coli* to simultaneously lyse the bacteria and amplify its DNA. After one hour of heating, I verified amplification by observing a characteristic ladder-like banding pattern in electrophoresis gels and deposited the reaction products onto LFIA strips. After 30 minutes, I expected to observe a pink test band, indicating a direct sandwich of the tagged amplicons between streptavidin coated gold nanoparticles and immobilized anti-fluorescein antibody at the LFIA's test line (Figure 5.1B). However, despite observing abundant amplification products by gel electrophoresis from reactions with as few as 275 *E. coli* cells, I observed only faintly positive test bands in the corresponding LFIA strips (Figure 5.2A). Only by quantitatively measuring the test band intensity of scanned strips and performing a Dunnett's multi-comparison test was I able to discern positive test bands of reactions with 275 *E. coli* cells from negative control reactions. Reliance on a computer algorithm to interpret the LFIAs would greatly limit their utility at points of need outside of a laboratory and. Therefore, I sought to improve the assay results for instrument-free interpretation.
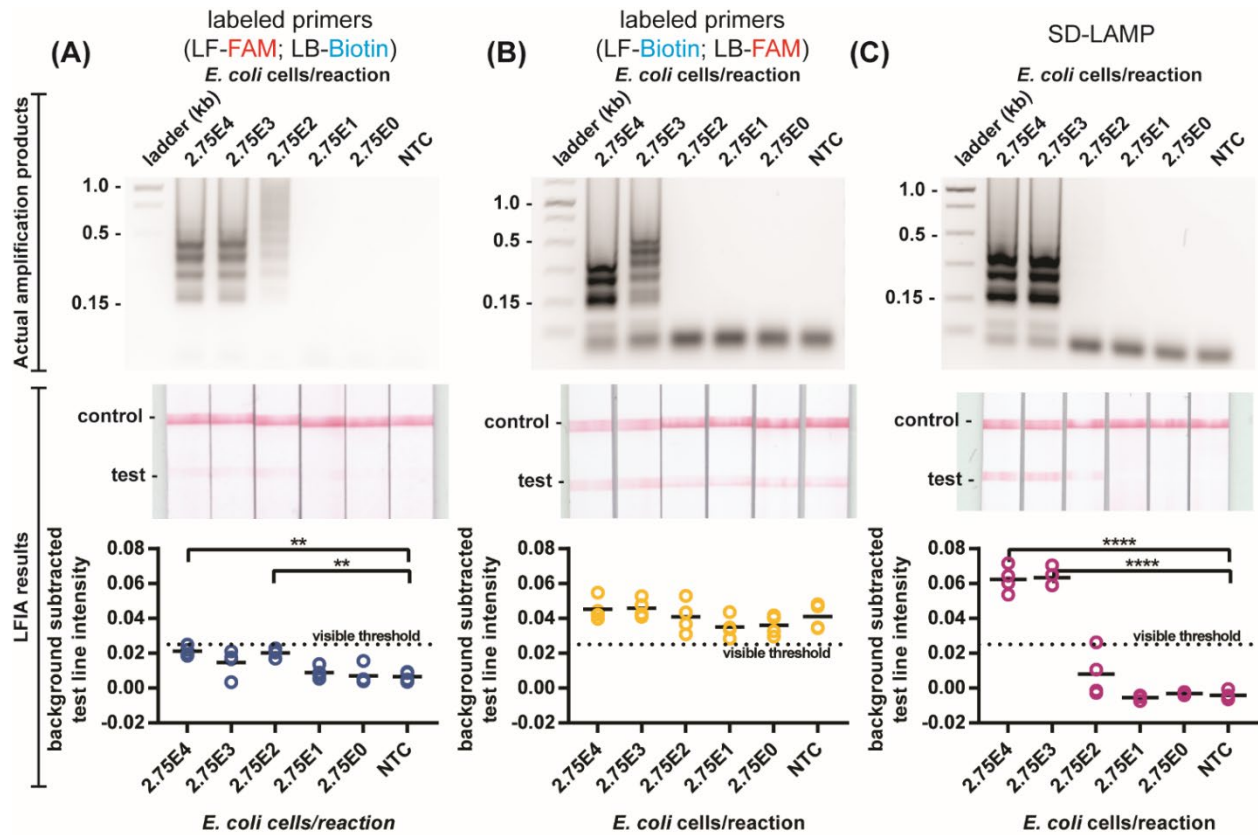
Figure 5.2 Detection of standard LAMP and SD-LAMP reactions in pure water.

Electrophoresis gels verifying amplification (top), LFIA test results (middle) and LFIA test line quantification (bottom). (A) Standard LAMP reaction products for *E. coli* labeled with primers (LF-FAM & LB-Biotin) yield LFIA results too faint for visual interpretation. (B) LAMP products labeled with reconfigured primers (LF-Biotin & LB-FAM) yield false positive LFIA results in low concentration samples and no template control (NTC) reactions. (C) Probed strand displacement LAMP reactions yield no false positive LFIA results for *E. coli*. n=4, replicates indicated by each circle. **** indicates $p \leq 0.0001$; ** indicates $p \leq 0.01$.

5.3.2. Human Subjects' Visual Interpretation of LFIAs.

To inform assay design specifications that would permit human interpretable LFIAs, I studied 18 human subjects' visual interpretation of LFIA strips. Half of the participants reported having previous instruction on how to read a lateral flow test (e.g. in a classroom or research setting) and the other half of participants reported having no previous instruction. All participants evaluated test strips and recorded whether they interpreted the LFIA to be positive, negative, or invalid when referencing a provided schematic (Figure S-9). A two-way ANOVA test confirmed that neither the order of test strip presentation nor the lighting conditions had confounding effects on test result interpretation. Test strips with a background-subtracted test band intensity above 0.020 were interpreted as positive more than 98% of the time by participants with and without previous instruction. However, just over half of participants repeatedly interpreted the next faintest test band (strip 4 in Figure 5.3 with a 0.013 background-subtracted intensity) as negative (Figure S-8), suggesting that there was a different visible threshold for a portion of participants. By using a Fisher's exact test to evaluate the effect of participants' previous instruction on their interpretation of test strip 4, I determined that users with prior instruction more frequently interpret this strip as positive while those without prior instruction interpreted the strip as negative (Table 5.1). For maximum usability by both trained and untrained LFIA readers, I therefore aimed for LFIAs to have a test band intensity of at least 0.020 for positive interpretation and well below 0.013 for negative interpretation.
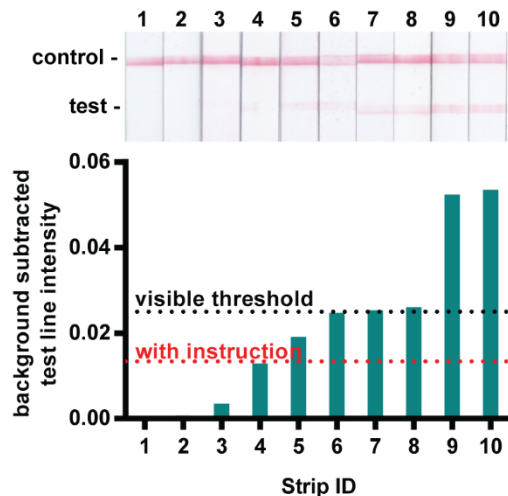

Figure 5.3 Ninety-eight percent of test strips with a background subtracted test intensity of 0.020 are interpreted as positive by unaided human subjects.

Table 5.1 Contingency table of 54 observations indicates a statistically significant interpretation of LFIA test when participant does or does not have previous instruction (p-value < 0.01).

	Interpret test strip 4 as positive	Interpret test strip 4 as negative	Total
Previous instruction	18	9	27
No previous instruction	7	20	27
Total	25	29	54

Noting that all of the LFIA test bands resulting from conventional *E. coli* LAMP reaction product capture were at, or below, the visible threshold of 0.020, I aimed to improve positive test band intensity. I hypothesized that steric hindrance had prevented efficient capture of the amplicons using LF-FAM and LB-biotin primers, and therefore repeated the amplification reactions with LF-biotin and LB-FAM primers (Figure 5.2B). The swapped primer tag configuration still yielded a limit of detection in agarose gels of 275 *E. coli* cells but resulted in positive test bands in all LFIAs, including negative controls. Not only were true positive LFIAs indistinguishable from negative control LFIAs by computer analysis, but all LFIAs would be interpreted positive by human eye. I and Taylor Moehling of the Linnes Lab observed similar non-specific capture of reaction products when performing a standard LAMP amplification of the *V. cholerae ctxA* gene using labeled primers (Figure 5.4A, Table S-1).[125]

5.3.3. Verification of *E. coli* primer tag effect on LFIA intensity.

To confirm that the difference in LFIA test line intensity was a result of the tag configuration (i.e. LF-FAM and LB-Biotin vs. LF-Biotin and LB-FAM) and not some other experimental or pipetting error, I prepared a single master mix of LAMP reagents without the tagged loop primers. I then split the master mix into two aliquots and added the two sets of tagged loop primers for amplification. The LAMP reactions with LF-FAM and LB-Biotin yielded LFIA test bands 4 times the intensity of LAMP reactions with LF-Biotin and LB-FAM, indicating a significant difference in steric hindrance between the two configurations (Figure D.7).

5.3.4. Modification of LAMP with Strand Displacement Probe

Suspecting that the false positive LFIA results were caused by LB and LF primer hybridization, as observed by other researchers,[51] I decided to replace the LF primer with a strand displacement probe tagged with FAM and perform SD-LAMP. The probe binds to the targeted loop region of the LAMP products by toehold-mediated strand exchange, a process that has been demonstrated to be exquisitely sequence specific due to the thermodynamic penalties of initiating branch migration.[126] Even single nucleotide mismatches prevent strand displacement of the probe. Since the probe does not prime amplification and spurious amplification products caused by LAMP primers' hybridization lack the probes' binding site, the probe is expected to hybridize with only true target amplification products. Therefore, no spurious SD-LAMP products are expected to contain both the biotin and FAM labels that facilitate capture on LFIAs and could otherwise cause false positive results. As expected,SD-LAMP reaction products from both *E. coli* and *V. cholerae* were deposited on LFIAs and yielded no false positive test bands. As seen in Figure 5.2C, positive test bands from as few as 2,750 *E. coli* cells are well above the visible threshold intensity. Moreover, LFIAs from negative control reactions display as true negatives. The order of magnitude decrease in sensitivity compared to the conventional LAMP reaction is likely a result of there being only 1 loop primer instead of the usual 2 that accelerate amplification.[127] In the *V. cholerae* LFIAs (Figure 5.4B) I did not observe a decrease in sensitivity and consistently visualized SD-LAMP product from as few as 350 cells (and several times as few as 3.5 *V. cholera cells*), likely because the primers bound more efficiently than the *malB* primers. However, as with SD-LAMP *E. coli* products, I observed only intense true positive LFIA test bands and no bands from true negative SD-LAMP *V. cholerae* products. Notably, the test band intensity (or lack thereof) resulting from SD-LAMP negative control reactions are narrowly distributed and well below the 0.013 threshold indicating that they can be easily interpreted as negative. Conversely, the test band intensities of negative control reactions using labeled primers were broadly distributed which caused user confusion during interpretation. Adding the strand displacement probes to the LAMP protocol is a simpler modification than redesigning primer sets or painstakingly optimizing reaction times. This essential modification mitigates spurious amplification and non-specific detection in easy-to-use LFIAs, improving LAMP's utility outside of a laboratory.
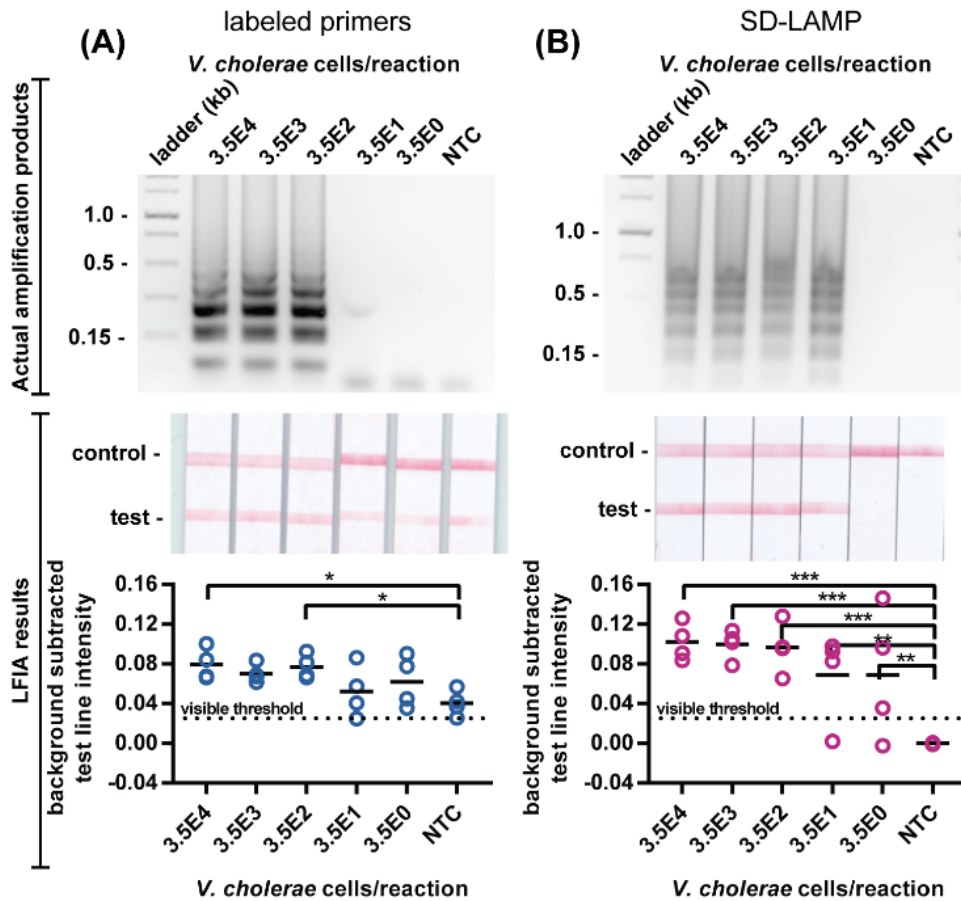
Figure 5.4 Detection of standard LAMP and SD-LAMP reactions in pure water.

Electrophoresis gels verifying amplification (top), LFIA test results (middle) and LFIA test line quantification (bottom). (A) Standard LAMP reaction products for *V. cholerae* labeled with primers yield false positive LFIA results in low concentration samples and no template control (NTC) reactions. (B) SD-LAMP reactions yield no false positive LFIA results for *V. cholerae*. n=4, replicates indicated by each circle. *** indicates $p \leq 0.001$; ** indicates $p \leq 0.01$; * indicates $p \leq 0.05$.

5.3.5. Verification of strand displacement probes' target specificity.

To demonstrate probes' specificity, a LAMP master mix (including F3, B3, FIP, BIP, and LB-biotin primers) optimized for *E. coli* was amplified with *E.coli* template and a probe designed for *V. cholerae*. Similarly, a LAMP master mix (inc. F3, B3, FIP, BIP, and LB-biotin primers) optimized for *V. cholerae* was amplified with *V. cholerae* template and a probe designed for *E. coli*. In both cases, despite successful amplification observed in agarose gel, no amplicons are captured on LFIA (Figure D.6A).

Next, to confirm specificity of primers and probes to their target, a LAMP master mix (including F3, B3, FIP, BIP, LB-Biotin primers and probe) optimized for *E.coli* was heated with *V. cholerae* template. Similarly, a LAMP master mix optimized for *V. cholerae* was heated with *E. coli* template. In neither case was non-specific amplification product observed in an agarose gel or in the respective LFIA strips (Figure D.6B).

5.3.6. SD-LAMP of Complex Sample Matrices

Both enteric pathogenic *V. cholerae* and *E. coli* have been found in environmental water sources and are significant public health concerns.[128,129] Furthermore, *E. coli* is a common cause of sepsis by infecting the blood stream of neonates and others with impaired immune systems.[130] The rapid, sensitive, and accurate detection of these pathogenic bacteria from complex matrices such as pond water and blood would aid in the control of waterborne and bloodborne infectious diseases. Given that complex matrices have been found to inhibit amplification assays such as PCR, I investigated whether pond water or human blood would similarly limit the utility of SD-LAMP visualization on LFIAs (Figure 5.5). I found LFIAs yielded positive test bands from SD-LAMP reactions performed with 50% pond water (the maximum possible ratio given that the reagents are pre-hydrated) and as few as 27,500 *E. coli* and 350 *V. cholerae* cells. LFIAs yielded positive test bands from SD-LAMP reactions performed with 10% human blood plasma and as few as 27,500 *E. coli* cells. The decrease in sensitivity caused by pond water and blood plasma is a result of a decrease in LAMP reaction efficiency in these matrices (as seen in Figure D.4 and also previously reported).[92] Because the LFIA results match the agarose gel outputs, I can confirm that these are not due to a decrease in the hybridization efficiency of the strand displacement probes or capture efficiency of the LFIAs. The positive test bands remained well above the 0.02 visible threshold intensity and the negative test bands remained well below the 0.013 threshold. This combined SD-LAMP and LFIA assay detects *E. coli* 100 times more sensitively than commercially available LFIA tests[78] that rely on surface antigen capture. Moreover, this combined SD-LAMP and LFIA assay can detect 1000 fewer *V. cholerae* cells than existing commercial dipstick tests (taking into account that the existing dipstick assay requires 200 µL of sample while SD-LAMP is a 25 µL reaction).[131]
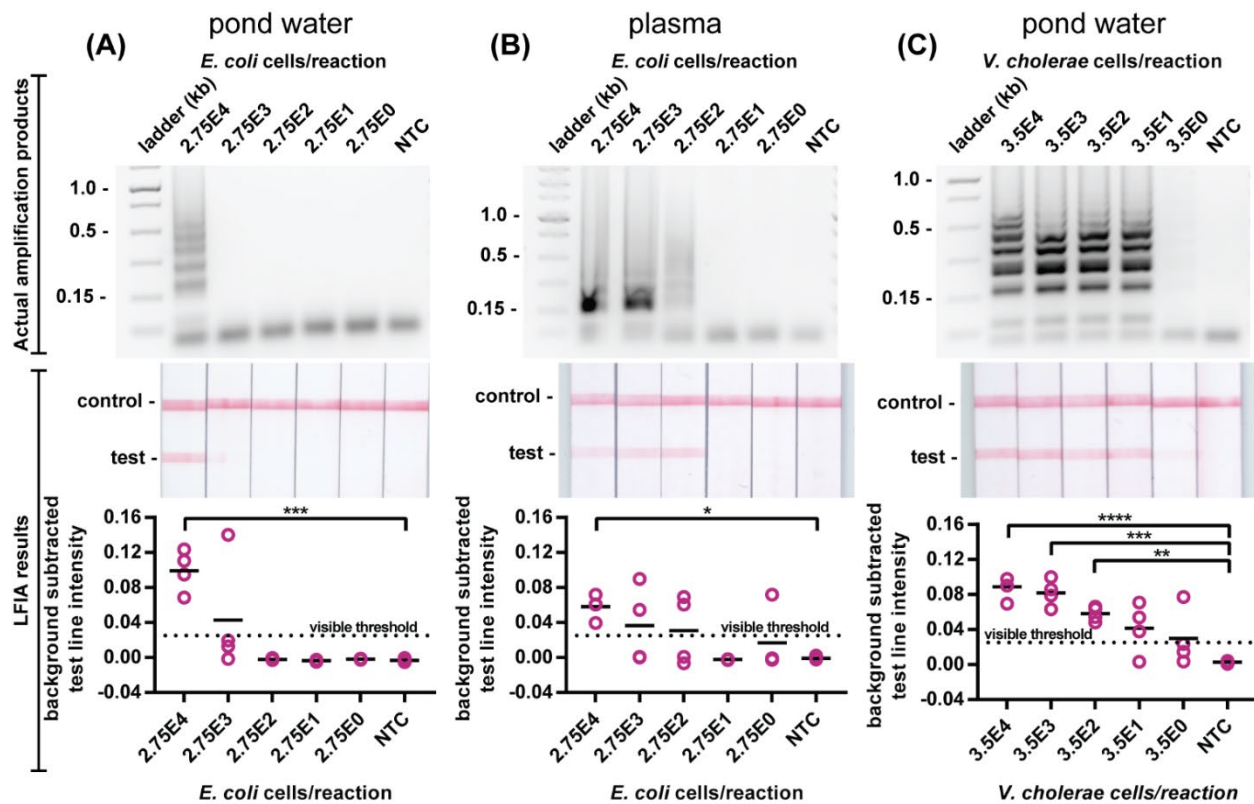
Figure 5.5 Detection of SD-LAMP reactions in complex matrices.

Electrophoresis gels verifying amplification (top), LFIA test results (middle) and LFIA test line quantification (bottom). SD- LAMP reactions yield no false positive LFIA results for *E. coli* diluted in (A) pond water and (B) human plasma. SD-LAMP reactions yield no false positive LFIA results for (C) *V. cholerae* diluted in pond water. n=4, replicates indicated by each circle. **** indicates p ≤ 0.0001; *** indicates p ≤ 0.001; ** indicates p ≤ 0.01; * indicates p ≤ 0.05.

5.4. Future Directions

In this chapter, I demonstrated how strand displacement probes can prevent capture of non-specific amplification products that yield false positive results. Rather than time-consumingly redesign and screen an entirely new primer set, one probe can be designed to replace one primer in the reaction. While this minimizes assay design iterations that typically require redesign of all 6 primers, it would be more efficient if candidate probes were included in design software that is used for selecting primers (e.g. PrimerExplorer). Future work could be to incorporate the design strategies of a strand displacement probe into a primer selection algorithm.

A shortcoming of these probes is, that by removing one of the primers from the reaction, amplification speed is reduced. In the future, a location other than the loop region of the gene sequence could be selected as the probe target. For shorter gene target sequences, there may be insufficient design space but for longer targets this could minimize reductions in sensitivity.

5.5. Conclusion

Until now, the utility of LAMP isothermal amplification outside of a laboratory has been restricted by the lack of signal transduction that is easy-to-use, low-cost, and specific. Strand displacement probes are a simple improvement to LAMP and provide instrument-free nucleic acid detection on low-cost LFIAs without requiring additional user steps. Future research will explore the combination of strand displacement probes with other isothermal amplification assays for instrument-free detection.

6. FUNCTIONALIZATION OF HYDROGELS WITH STRAND DISPLACEMENT PROBES FOR BIO-RESPONSIVE VALVING IN POROUS MEMBRANES

6.1. Rationale

Instrument-free detection of pathogens in patient and environmental samples is necessary to inform treatment and control infections at the point-of-need. With an electronic reader, LFIA results can provide a semi-quantitative output of sample concentration. Without an electronic reader, my studies in Chapter 5 indicate that varying intensity LFIAs are difficult to interpret qualitatively, much less quantitatively (Figure 5.3). This finding is in accordance with previous studies indicating that the traditional colorimetric readout, hue, is one of the most challenging visible changes to discern.[60] Many researchers have shifted from intensity and hue-based readouts to distance-based readouts such as the Henry group's metal[61] and glucose[62] sensors and the Yang group's hydrogel integrated glucose sensors.[63] Unfortunately, these methods can also require excessive reagents (i.e. the entire paper strip is coated with capture molecules or enzyme) and increase the ultimate cost of the device. To minimize reagents, I sought to create a bio-responsive valve that releases fluid in the presence of target DNA. By combining my understandings of valve-mediated flow control in paper membranes (Chapter 2) with intelligently designed DNA capture mechanisms (Chapter 5), I sought to modulate flow distance with a bio-responsive valve composed of a DNA-functionalized hydrogel. This distance-based readout could provide a more easily discernable signal of the presence or even concentration of target DNA than traditional colorimetric readouts.

In this chapter, I first describe the functionalization of multi-armed polyethylene glycol (PEG) with short strands of ssDNA (strands SA and SB) to form a hydrogel precursor. To form a hydrogel, the precursors can be crosslinked with the strand displacing probe designed in Chapter 5 (L strand). This step-growth polymerization technique can yield hydrogels with a homogenous porosity that, when embedded into a membrane test strip as a closed valve, block passage of visible nanoparticles or molecules by size exclusion. When the hydrogel valve is crosslinked via the SA-L-SB hybridization, the single-stranded region of the probe will remain an available toehold to initiate strand displacement with a complimentary sequence (R strand or a target LAMP amplification product), causing the hydrogel to dissolve. The passage of nanoparticles would

signal hydrogel dissolution and valve opening. In my preliminary work to synthesize the hydrogel precursors, I found there were several challenges to functionalizing PEG hydrogels with strand displacement probes and so discuss several strategies for future research.
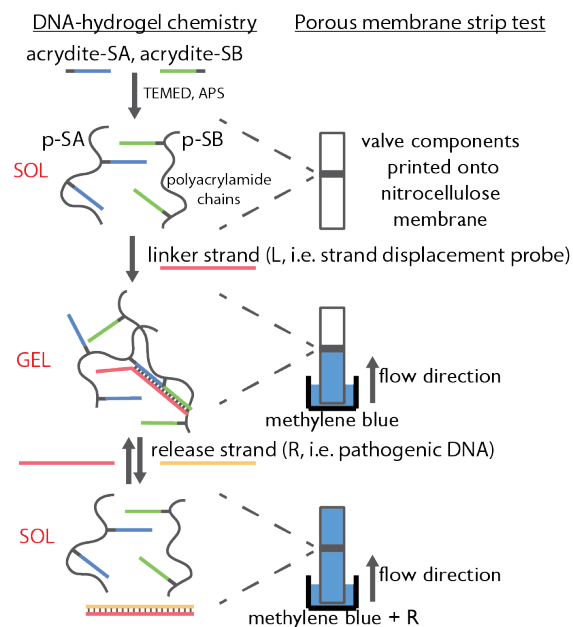
Figure 6.1 Schematic of DNA-hybrid hydrogel printed onto nitrocellulose membrane test strips.

I next describe an alternative hydrogel functionalization strategy by grafting ssDNA strands (SA and SB) to polyacrylamide backbones with free radical chemistry (i.e. chain growth polymerization). As with the PEG hydrogel strategy, when the hydrogel is crosslinked via the SA-L-SB hybridization, the toehold region of the L strand can trigger hydrogel dissolution in the presence of a target R strand (or LAMP amplification product) (Figure 6.1). Similar DNA-hybrid hydrogels have been investigated for their response to DNA and aptamer binding targets in tube-based reactions, but not when the hydrogel is embedded in other substrates such as paper membranes.[69,132–135] I found that the flow of a reporter molecule past the valve can be modulated by adjusting the hydrogel valve's density and location from the sample deposition area. As expected, the presence of a release strand triggers the dissolution of the valve and also modulates flow of the dye. A future challenge to implementing this hydrogel valve for DNA detection is to decouple the effect of the buffer composition and release strand concentration on reporter molecule migration.

6.2. Materials and Methods

6.2.1. Functionalization of PEG with DNA

To synthesize a hydrogel precursor, I grafted SA and SB oligonucleotides onto 4-arm polyethyene glycol (PEG) using amine reactive chemistry with NHS ester. The oligonucleotide sequences used are listed in Table 6.1 and were rehydrated to 10mM in sodium borate buffer, pH 8.5 (NaB). 4-arm PEG functionalized with succinimidyl carboxymethyl ester (SC) (2K – 20K MW, Creative PEGWorks, Chapel Hill, NC) was rehydrated to 10 mM in dimethyl sulfoxide (DMSO) (and stored at -20ºC until use) or stored lyophilized at -20ºC until use and rehydrated to 10 mM in NaB. To graft SA or SB to 4-arm PEG rehydrated in DMSO, solutions were incubated for 1 hour at room temperature on a vortexer. To graft SA or SB to 4-arm PEG rehydrated in NaB, solutions were vortexed briefly, spun down, and incubated at room temperature for 1 hour.

To confirm conjugation of SA to 4-arm PEG, solutions were loaded into a 3% agarose gel containing SYBR Gold and were run at 100V for 90 minutes. Gels were imaged on a gel reader with a 15 second exposure.

Table 6.1 Sequences of oligonucleotides to functionalize PEG hydrogels

Oligonucleotide	# of bases	Sequence (5' → 3')	Modification	T_m (°C)
SA	14	**TCTTGGCATAAGA**	5' amine	36.6
SB	12	*CCACCTGAAG*	5' amine	37.1
L	36	*CTTCAGGTGG***TCTTATGCC AAGA**GGACAGAGTG	None	65.4
R	36	GCCCTTCTCCCTTTGTAAC AACCTGTCATCGACCAG	None	65.4

6.2.2. Hydrogel formation with DNA and PEG

To crosslink DNA-hybrid hydrogels with a PEG backbone, hydrogel precursors prepared in **Section 6.2.1** were mixed together with oligonucleotide L rehydrated in Dulbecco's phosphate buffered saline (DPBS) (with calcium and magnesium, cat. no. 14040133, Gibco, Grand Island, NY), vortexed briefly, spun down, and incubated at room temperature for 1 hour. To visualize hydrogel formation, 500 µL of 0.1 mg/mL MB or 2% solutions of water-soluble colored dye

(McCormick, Sparks, MD) was deposited on top of the hydrogel and the tube was flicked to assess gel stability.

Alternatively, to form a hydrogel with only PEG as the crosslinker, 4-arm PEG-SC rehydrated in NaB was mixed with bifunctional PEG-amine (10K MW, Creative PEGWorks, Chapel Hill, NC) rehydrated in NaB. To form hydrogels with PEG and DNA as the crosslinker, equimolar solutions of SA, SB, and L were annealed at 95°C for 1 minute followed by 0.1°C/second cooling to room temperature. Then, 4-arm PEG-SC and bifunctional PEG-amine rehydrated in NaB was mixed with this complex, briefly vortexed, spun down, and incubated at room temperature for 1 hour. To visualize hydrogel formation, 500 µL of 0.1 mg/mL MB was deposited on top of the hydrogel and the tube was flicked to assess gel stability.

6.2.3. DNA-hybrid hydrogel formation with polyacrylamide

DNA-hybrid hydrogels were formed by crosslinking polyacrylamide with hybridized oligonucleotides. First, hydrogel precursor solutions were prepared by grafting two ssDNAs (SA and SB) with 5'-Acrydite^{TM} modifications onto a polyacrylamide backbone (pSA and pSB) by ammonium persulfate and TEMED catalysis (Figure 6.1, left) to a final concentration of 0.5 - 2% acrylamide. More specifically, oligonucleotides in Table 6.2 were rehydrated to 3 mM in Tris-EDTA buffer (TE). Hydrogel precursors were prepared by first mixing acrylamide (Sigma), Tris/Borate/EDTA buffer (TBE), and SA or SB and degassing the solution for 3 minutes. Ammonium persulfate (APS) was added to initiate gel polymerization followed by TEMED to catalyze polymerization. Finally, solutions were centrifuged for 15 seconds at 2,000 x g and degassed for 3 minutes to minimize un-reacted monomers. Final precursor solutions were incubated for 10 minutes at room temperature to complete polymerization and contained 1.44 mM SA or SB, 0.5 – 2% acrylamide, 1x TBE, 0.05% APS, and 0.50% TEMED. Equimolar solutions of precursors were then mixed with oligonucleotide L and incubated at 32°C (~5°C below the T_m of SA) for 1 hour to anneal the DNA strands and then at room temperature for 4 hours to fully crosslink the hydrogel.

Table 6.2 Sequences of oligonucleotides to cross-link DNA-hybrid hydrogels

Oligonucleotide	# of bases	Sequence (5' → 3')	Modification	T_m (°C)
SA	14	**CTTTGTAACAACCT**	5' Acrydite	37.2
SB	12	*GTCATCGACCAG*	5' Acrydite	39.4
L	36	*CTGGTCGATGAC***AGGTTGT TACAAAG**GGAGAAGGGC	None	66.1
R	36	GCCCTTCTCCCTTGTAAC AACCTGTCATCGACCAG	None	66.1

6.2.4. DNA-hybrid hydrogel kinetics

For initial characterization of hydrogel dissolution kinetics, 6.5 µL hydrogels were prepared as described previously. Hydrogels were incubated with either, A) 500 µL of 1 mg/mL of methylene blue (MB) in DPBS, or B) just DPBS to swell the hydrogels. Gels incubated with DPBS were dried for 8 hours at room temperature and then incubated overnight with 500 µL of 1mg/mL of MB in DPBS. Both preparations of MB absorbed hydrogels were washed four times in 500 µL of DPBS. 1.5 µL of 3 mM oligonucleotide R with 100 µL of TE buffer was deposited on top of the hydrogels. The absorbance (665 nm) of 2 µL samples of supernatant was measured on a Nanodrop at multiple timepoints between 0 and 24 hours.

To characterize the dissolution kinetics of hydrogels embedded in a porous membrane, I pipetted equimolar concentrations of the hydrogel components (2.5 µL of pSA, 2.5 µL of pSB, and 1.5 µL of L; 4.5 nmol of L) onto 0.1 micron pore sized PES membranes (Sterlitech, Kent, WA). The spotted membranes were incubated at 32°C for 1 hour and then at room temperature for 4 hours to crosslink the DNA-hybrid hydrogels. The spotted membranes were subsequently washed in DPBS overnight, dehydrated on a benchtop overnight at room temperature to air dry, and incubated overnight with 500 µL of 1 mg/mL MB in DPBS. The dyed membranes were washed four times in 500 µL DPBS before immersing the washed membranes in a 100 µL solution of 45 µM R in TE buffer (positive) or just TE buffer (negative). The immersed membranes were shaken on a rotating table to minimize the effect of reporter and dye diffusion. The absorbance (665 nm) of two microliters of solution was analyzed on a NanoDrop every 15 minutes to quantify MB release from the hydrogel.

6.2.5. Bio-responsive valve response characterization

Hydrogels were embedded into nitrocellulose membranes to test the effects of acrylamide and R concentration on MB dye migration in the membranes. Equimolar solutions of pSA and pSB were mixed and deposited as a band onto nitrocellulose membranes (FF120HP, GE Healthcare) with a micropipette (~0.5 µL per 0.25 mm wide strip) or with a Claremont Bio Reagent Dispenser (~9 µL of solution deposited at a rate of 30 µL/min over a 7 cm wide membrane strip 4x amounting to ~0.3 µL per 0.25 mm wide strip). Upon air drying, the solution of L was deposited over the top of the pSA and pSB line. Printed nitrocellulose membranes were incubated 32°C for 1 hour and then at room temperature for 4 hours to crosslink the DNA-hybrid hydrogels. Then, nitrocellulose membranes were washed in DPBS overnight to remove uncrosslinked components, dehydrated at room temperature, and cut into 0.25 x 2 cm strips with a 40W CO_2 laser cutter (power: 25%, speed: 100%, PPI: 500). Strips of absorbent Chr1 chromatography paper (GE Healthcare) were adhered to the end of the nitrocellulose membranes. The prepared test strips were dipped into 0.1 mg/mL MB solutions containing 0 – 75 µM of R and the MB's migration through the strips was observed.

6.2.6. Selection of reporter dye

Solutions of MB were utilized as a reporter dye to monitor flow past a bio-responsive valve. To determine whether the charge of a reporter dye influenced flow, the charges of available dyes were determined by migrating them in 1% agarose gel by electrophoresis. 10 µL of each dye (1x FastDNA ladder, 1x NEB purple loading dye, 1x Promega Blue/Orange dye, 1 mg/mL neutral red, 0.1 mg/mL MB, and 5 mg/mL of acridine orange in water) (concentrations were selected so that all would have a comparable visible color intensity) or FITC labeled dextran (4kDa, 40kDa, 70kDa, and 150kDa molecular weight diluted to 0.1 mg/mL in water) were loaded in an agarose gel and ran for 45 minutes at 100 V. The distance the dye front traveled was measured in ImageJ.

Next, nitrocellulose membranes with bio-responsive valves printed as described earlier were dipped in solutions of each dye listed above. The time it took for each dye to flow past the valve was recorded.

Finally, strips of native nitrocellulose membranes (no valve) were dipped into solutions of 0 – 37.5 µM oligonucleotide R, 0.625 – 1.25% TE, and 0.1 – 1 mg/mL of MB. The time it took for dye to flow 1.3 cm was recorded.

94

6.3. Results and Discussion

6.3.1. Functionalization of PEG with DNA

To create DNA-hybrid PEG hydrogels, I could either graft SA and SB to 4-arm PEG and then crosslink with oligonucleotide L (Figure 6.2A) or pre-anneal SA, SB, and L and conjugate the annealed product to 4-arm PEG (Figure 6.2B). Initially, I used the former strategy and conjugated SA and SB to 4-arm PEG (20kDa molecular weight). As expected, conjugation products (pSA and pSB) loaded to an agarose gel migrated much less than unconjugated SA and SB oligonucleotides (Figure 6.3). The high molecular weight of the PEG slowed the migration of the conjugated oligonucleotide. Several bands are observed at the top of the gel, indicating that some 4-arm PEG monomers were conjugated to 1, 2, 3, or 4 (maximum) molecules of SA or SB, depending on the efficiency of conjugation. The inefficiency of the conjugation is also evident by the vast quantity of unconjugated oligonucleotides at the bottom of the gel observed after using a size exclusion column to filter out unconjugated oligonucleotides (Figure 6.3A). Using Sephadex G-50 resin (product no. S5897, Sigma-Aldrich, Saint Louis, MO) in a 15 cm gravity column, I was able to better filter out unconjugated products (Figure 6.3B), however, after combining the purified fractions I was unable to quantify the product. Therefore, I was unsure how much oligonucleotide L to add to crosslink the precursors into a hydrogel. I attempted to quantify the efficiency of the conjugation by mass spectrometry (MALDI, Purdue University Core Facility) but there was too much background from the large 4-arm PEG (20kDa molecular weight, hydrated in DMSO) to discern conjugated products. Even when I attempted to quantify the efficiency of SA conjugated to a smaller 4-arm PEG (2kDa molecular weight, hydrated in NaB), the product was too "tacky" to be measured. The hygroscopic nature of low molecular weight PEG causes it retain moisture and not dry sufficiently during sample preparation for MALDI analysis. Quantification of conjugation efficiency was also not possible by spectrophotometry because hydrolyzed NHS absorbs at the same wavelength as DNA. Even when I subtracted out the absorption of just hydrolyzed 4-arm PEG-SC I was unable to discern a difference in conjugated product likely due to too much variation in conjugation efficiency between conjugation batches.
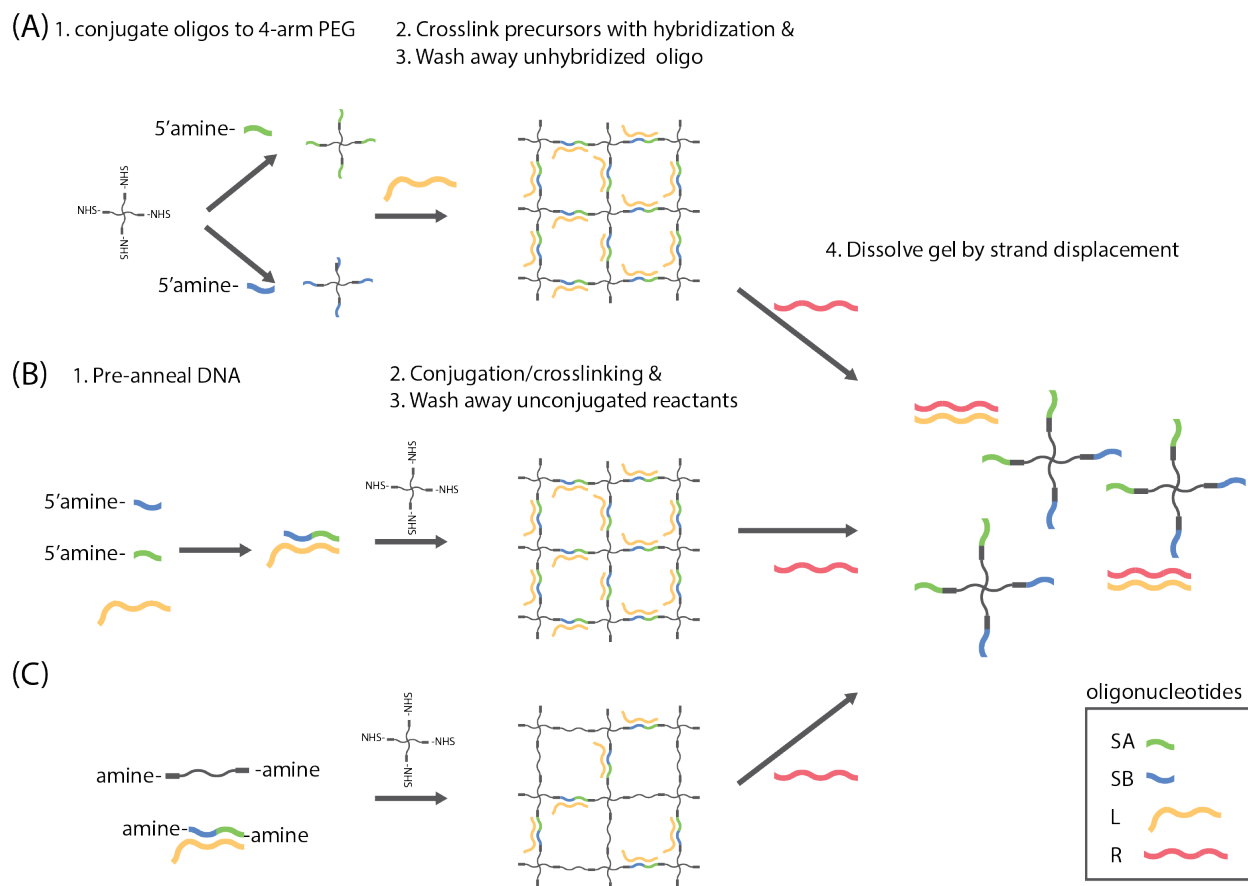
Figure 6.2 Schematic of DNA-hybrid PEG hydrogel formation.

(A) Amine-reactive oligos are conjugated to 4-arm PEG-SC and then crosslinked by hybridizing a third oligo. (B) Oligos are pre-annealed and then conjugated to the 4-arm PEG-SC to crosslink the hydrogel. (C) Pre-annealed oligos and a bifunctional PEG are conjugated to 4-arm PEG-SC to crosslink the hydrogel. In the presence of a release strand, strand displacement causes hydrogel dissolution.

6.3.2. Hydrogel formation with DNA and PEG

To create DNA-hybrid hydrogels using the strategy in (Figure 6.2B), I first evaluated the concentration of PEG required to form a stable hydrogel. Instead of using DNA to crosslink the hydrogel, I used 10kDa molecular weight bifunctional PEG. Given that SA and SB are each ~5kDa, I expected that this size bifunctional PEG would best mimic the crosslinking length of the DNA crosslinkers. I determined that only 4-arm PEG of 2 and 5kDa molecular weight could form a stable hydrogel with 10kDa molecular weight bifunctional PEG (Figure 6.4A&B). Conjugation products of 4-arm PEG of 10 and 20kDa molecular weight with 10kDa molecular weight bifunctional PEG dissolved when solutions of food dye or MB were deposited on top of the gel.

Likely, the polymers formed with these larger 4-arm PEGs had too long of crosslinks to absorb and structure the water (i.e. the hydrophobic block is too long[136]). Hydrogel formation was also dependent on the stoichiometric ratio of amine groups to NHS groups. Though the results in Figure 6.3 indicate that the amine-NHS conjugation was not 100% efficient, if the stoichiometric ratio deviated from 1:1, then a stable hydrogel would not form (Figure 6.4C). Other groups have similarly reported the importance of stoichiometric unity to form a hydrogel.[137] Similarly, if the weight/volume percentage of 4-arm PEG was too low, then a stable hydrogel would not form. The challenge, then, was to replace the bifunctional amine-PEG with pre-annealed SA-L-SB complex to crosslink the hydrogel with DNA and maintain a high enough w/v% and stoichiometric unity (Figure 6.2C). After annealing the SA-L-SB complex, the maximum concentration of reactive amines is 6.6 µM, much lower than the concentration of amines in the bifunctional PEG solutions (40 mM), (in the future, the annealed DNA could be concentrated by size exclusion to increase the amine concentration). Therefore, when substituting bifunctional PEG with the DNA complex, the weight/volume percentage of PEG decreased and a stable hydrogel could not be formed (Figure 6.4D). A stable hydrogel could only be formed when I used pre-annealed L-R (both with 5'-amine groups) (Figure 6.4E) which could be prepared to a higher reactive-amine concentration of 10 µM. I propose several strategies in **6.4 Future Directions** to create DNA-hybrid PEG hydrogels.
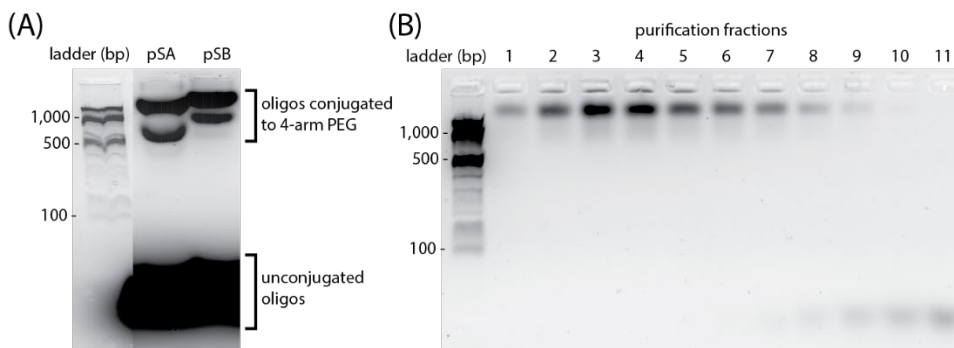

Figure 6.3 Purified products of oligonucleotides SA and SB conjugated to 4-arm PEG (20K MW) as visualized by 3% agarose gel electrophoresis with SyberGold staining.

Multiple bands at the top of each gel correspond to partially and fully conjugated 4-arm PEG. Bands at the bottom of the gels correspond to unconjugated oligos. (A) Conjugation products (pSA and PSB) were inadequately separated from unconjugated oligos using a 10K centrifuge filter. (B) G-50 Sephadex resin yielded a better separation of conjugated products (pSA) from unconjugated oligos.
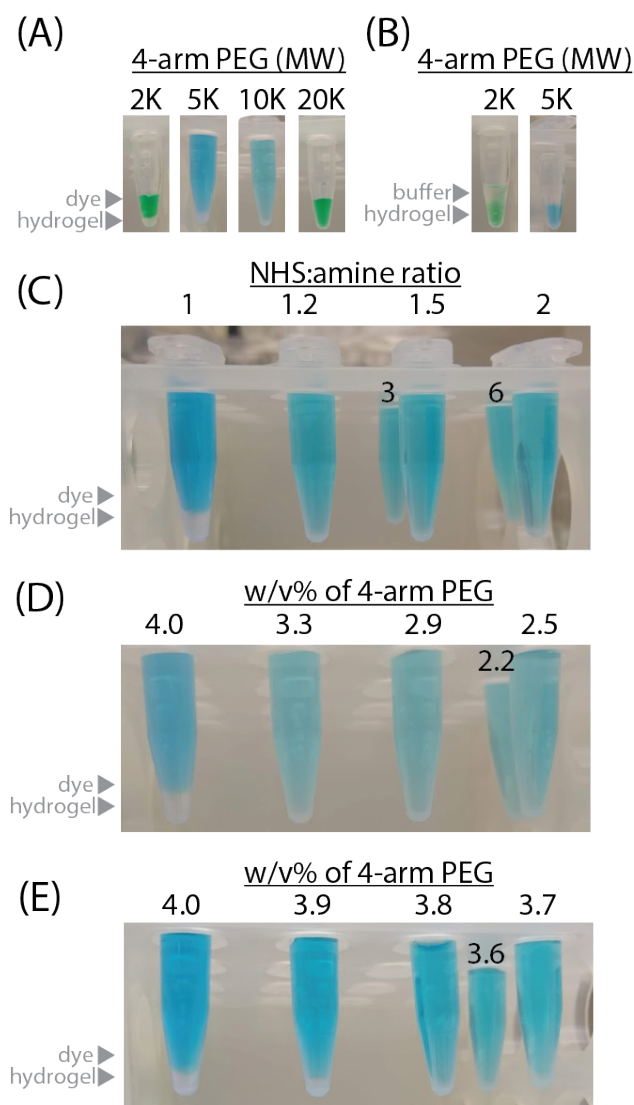
Figure 6.4 Effect of crosslinking length and density on PEG hydrogel formation.

(A) Only 4-arm PEGs with a molecular weight of 2 – 5K formed a stable hydrogel when crosslinked with 10K bifunctional PEG, as visualized by green food dye or methylene blue solution. (B) After an overnight incubation, the PEG hydrogels absorbed the dye. (C) Only when there was a ratio of 1:1 of NHS:amine reactive groups did a hydrogel form (D) Maintaining a 1:1 ratio of NHS:amine but replacing bifunctional PEG with pre-annealed SA/SB/L prevented a hydrogel from forming. Note that the 4 w/v% gel was only composed of 4-arm and bifunctional PEG. (E) Maintaining a 1:1 ratio of NHS:amine but replacing bifunctional PEG with pre-annealed L/R, a gel was formed only with 3.9 w/v%. Note that the 4 w/v% gel was only composed of 4-arm and bifunctional PEG.

6.3.3. DNA-hybrid hydrogel kinetics

To determine whether an oligonucleotide could trigger the dissolution of a DNA-hybrid hydrogel, I prepared hydrogels crosslinked with a 36 base pair linking strand (L). Notably, L is the same sequence as the FAM-labeled strand of the *E. coli* strand displacement probes discussed in **Chapter 4**. When hybridized to the strands SA & SB grafted to the polyacrylamide backbone of the hydrogel, L contains an unhybridized, 10 base pair toe-hold sequence. In the presence of a strand (R) complimentary to L, the toe-hold sequence was expected to trigger the dehybridization of L from the grafted strands and cause the hydrogel to dissolve. Prepared hydrogels were absorbed with a reporter dye, MB, to measure the kinetics of the dissolution and either mixed end-over-end on a rocking table or unmixed. As Figure 6.5 A and B demonstrate, when hydrogels were not dehydrated before absorption with reporter dye, the rate of release of dye from the hydrogel was unrelated to whether release strand was present or not. Unexpectedly, after 24 hours, more dye was release from the hydrate, mixed gels when R was not present than when R was present (Figure 6.5 A) which may be caused by batch testing inconsistencies (i.e. some of the gels may have been less hydrated than others and ultimately pre-sorbed more dye). However, when the hydrogel was dried and then absorbed with hydrogel, then there was a distinguishable difference (and consistent trend over 24 hours) in the rate of dye release in the presence vs absence of the R strand (Figure 6.5 C). Importantly, this response was not evident when the supernatant and gel were not mixed (Figure 6.5 D), likely because poor diffusion of the R strand into the hydrogel limited the strand displacement reaction.
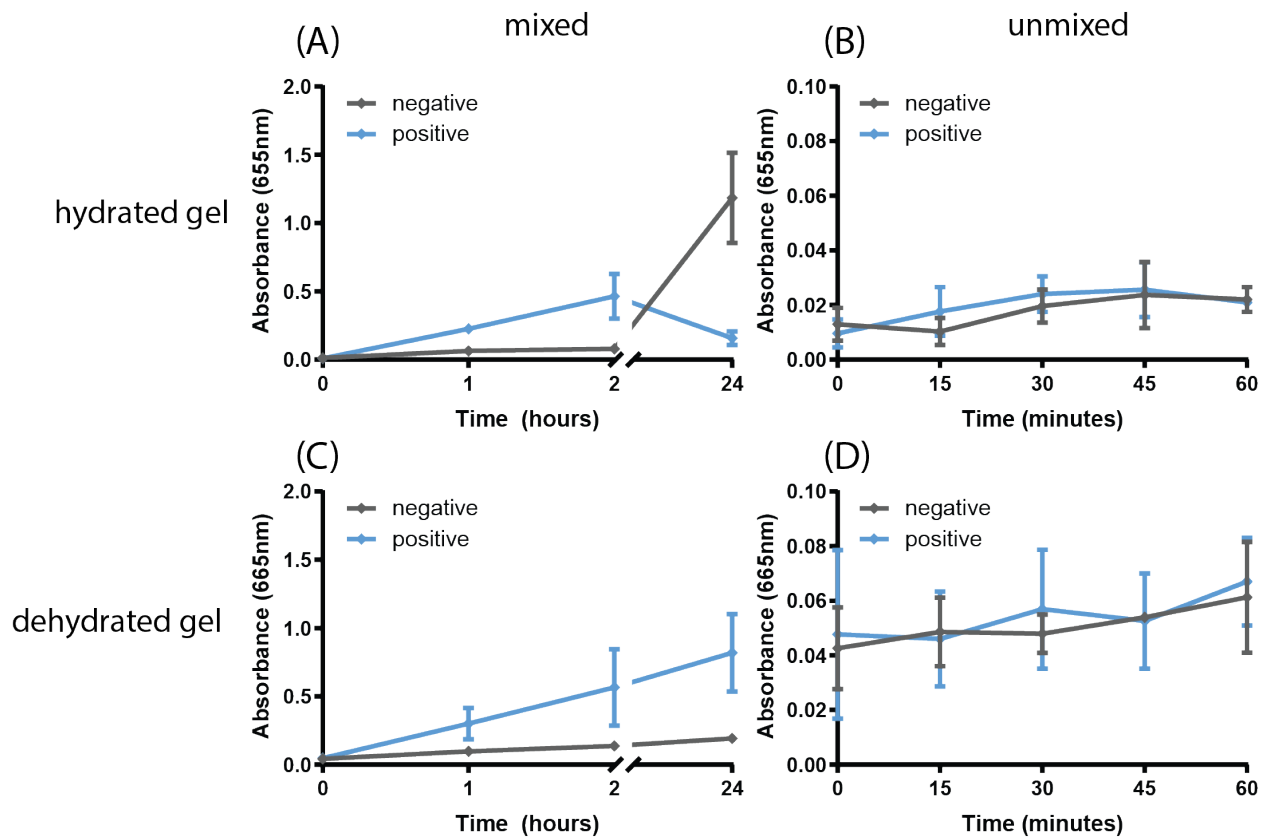
Figure 6.5 Release of dye from DNA-hybrid hydrogels absorbed with methylene blue in the presence of release strand (positive) or not (negative).

When methylene blue is absorbed into a fully hydrated hydrogel and the supernatant (A) mixed or (B) unmixed, then positive and negative results are indistinguishable. (C) When a hydrogel is dehydrated before being absorbing methylene blue and the supernatant is mixed, there is a discernable difference between a positive and a negative response. (D) When the supernatant is not mixed, there is no difference in dye release. n=2; error bars indicate standard error.

When hydrogel components were deposited onto PES, the hydrogel could similarly be absorbed with MB (Figure 6.6A). When the supernatant did not contain release strand, MB diffused from the hydrogel and was detectable in the supernatant. However, when the supernatant contained release strand and was mixed end-over-end on a rocking table for an hour, the release of MB was much faster, indicating that the hydrogel was dissolving. Notably, this release was differentiable from the diffusive release within 15 minutes (Figure 6.6B); this rapid release follows a similar time-scale of previously reported strand displacement reactions.[138]
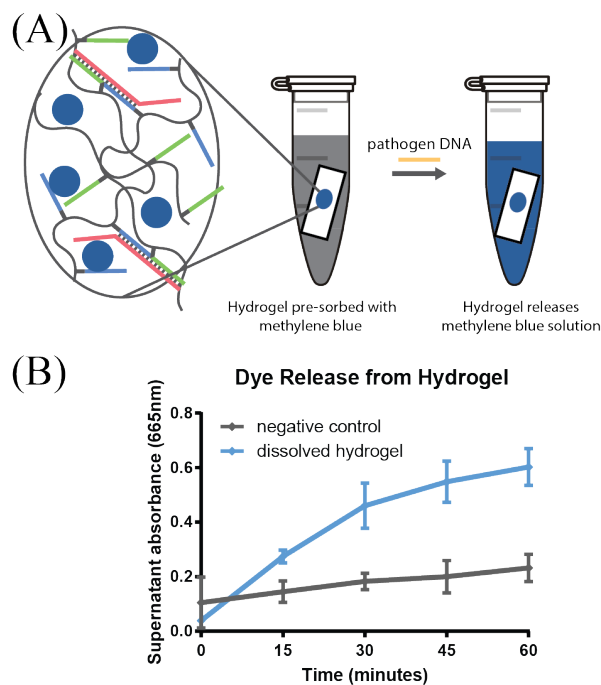

Figure 6.6 Release of dye from hydrogel embedded into membrane.

(A) Schematic of DNA hybrid hydrogel releasing dye in the presence of release strand. (B) Absorbance of supernatant upon addition of release strand indicates hydrogel detectably dissolves within 15 minutes. n=3; error bars indicate standard error

6.3.4. Bio-responsive valve response characterization

When hydrogel precursors, pSA and pSB, were deposited onto nitrocellulose membrane and dipped into a solution of MB, the dye flowed at a comparable rate as native nitrocellulose membrane. However, when oligonucleotide L was deposited on top of the precursors, a hydrogel was formed that blocks dye from migrating (Figure 6.7). Importantly, dye was only blocked when the valve was printed at least 0.8 cm from the beginning of the test strip. Because of the chromatographic separation of the dye solution, there was a clear liquid front that migrated faster than the dye front. When the valve was printed closer to the edge, there was insufficient time to hydrate the hydrogel and block the dye. As expected, the farther the valve was printed from the edge, the longer it took dye to flow past the valve when release strand was present. The flow rate of dye past the valve was also dependent on the density of the hydrogel (Figure 6.8). When hydrogels were prepared with 2% polyacrylamide, no matter the concentration of release strand, dye was unable to flow past the valve because of the high density and viscosity of the hydrogel. Conversely, when a hydrogel was prepared with too little acrylamide (e.g. 0.5%), the valve was unable to block dye from passing even when no release strand was present. These results indicate that there is a critical concentration of acrylamide in the hydrogel to maximize the difference between a positive and a negative result. Figure 6.8B illustrates that, for hydrogels prepared with 0.5% acrylamide, the time to flow 0.5 cm past a valve is dependent on the release concentration; at high concentrations of release strand, the dye flows faster than at low concentrations of hydrogel. Presumably, more release strand dissolves a greater proportion of the hydrogel and thus there is less resistance to flow. I expected that with a lower concentration of acrylamide, I would see a similar concentration dependence. However, no matter the concentration of acrylamide, the flow rate remained constant at each concentration of release strand. Only the reporter dye with no release strand flowed faster with lower concentrations of acrylamide. These results suggest that the release strand was interacting with the reporter dye.
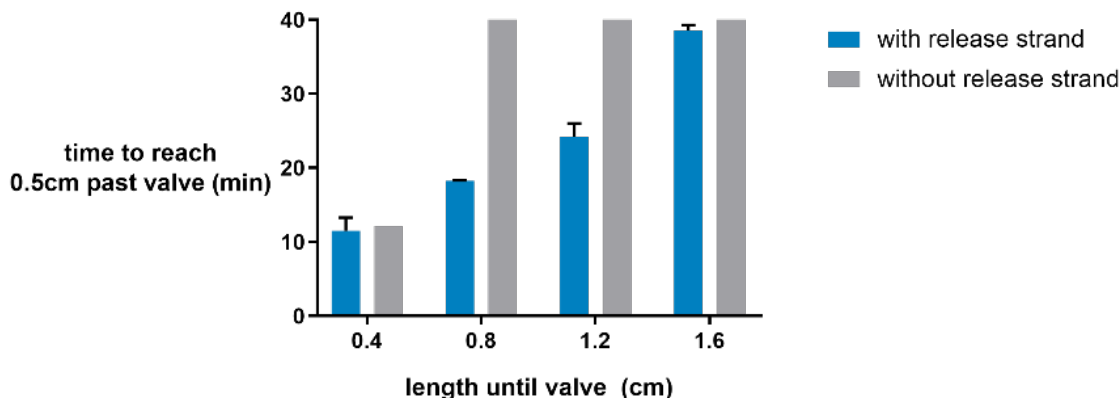
Figure 6.7 Effect of bio-responsive valve location on dye migration time.

The valve had to be printed at least 0.8 cm away from the beginning edge of the test strip to block dye from migrating past a closed valve. When release strand is present, the dye migrates past the valve. n=2; error bars indicate standard error.

(A)

(B)
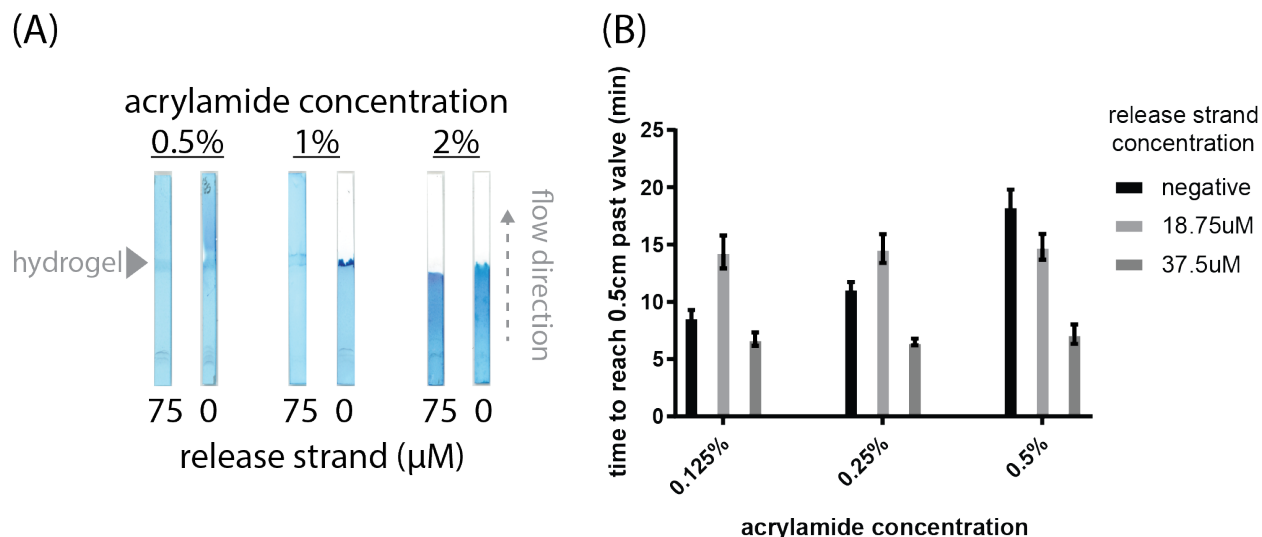
Figure 6.8 Effect of acrylamide concentration on dye migration past a valve.

(A) Low density hydrogels containing 0.5% acrylamide permit passage of dye within 30 minutes when no release strand is present but high density hydrogels containing 2% acrylamide block the passage of dye when release strand is present. (B) At 0.5% acrylamide concentration, the flow rate is dependent on release strand concentration but at lower density hydrogels there is no correlation. n=6, error bars indicate standard error

6.3.5. Selection of reporter dye

Given the negative charge of DNA and positive charge of MB, it is not surprising that there was interaction between the two species. To identify other candidate reporter dyes that may interact less with the valve and release strand, I first evaluated the charge of readily-available dyes. As Figure 6.9A illustrates, dyes identified to be anionic by gel electrophoresis were not blocked by the hydrogel valve even when a release strand was not present in the solution. Only cationic dyes were delayed by the hydrogel valve and only MB was blocked by the valve for at least 20 minutes (Figure 6.9C). Despite its anionic charge, FITC-dextran molecules were blocked by the valve for substantially longer than MB (Figure 6.9D). I estimate the crosslinking length of the hydrogel to be <9 nm (based on a 26 base-pair crosslength), which is likely smaller than the hydrodynamic diameter of the FITC-dextran molecules that were blocked (estimated to be 9 nm (40K MW), 12 nm (70K MW), and 17 nm (150K MW) based on Sigma-Aldrich data sheets). The hydrogel's swelling and porosity is also influenced by the charge of the sample, so the effective pore diameter is likely less than the 9 nm crosslink. One of the 4K MW (estimated to have a 4.6 nm diameter) replicates was partially blocked by the hydrogel, demonstrating that attributes such as the hydrodynamic radius and the swelling ratio should be characterized to better identify candidate molecules that could be blocked by the valve by size exclusion (discussed further in **6.4 Future Directions**). Moreover, another dye label would need to be used; FITC fluoresces at the same wavelength as nitrocellulose and so is indistinguishable from the background by fluorescence (this is a reported phenomenon but was verified by trying to image with the Cy3 channel of an imaging system (c400, Azure Biosystems, Dublin, CA)) and is only visible by eye when enough dye accumulates at the valve (i.e. after an overnight incubation).

Suspecting that the TE buffer, a chelator, was influencing MB's flow rate dependence, I evaluated the flow rate of MB with varying concentrations of TE buffer in native nitrocellulose membrane (no valve printed). As Figure 6.10A illustrates, when a strip of nitrocellulose membrane is dipped into a solution of 0.1 mg/mL MB, the dye flow front rate decreases with increasing TE buffer. Presumably, the TE buffer chelates the positively charged MB and the dye becomes hydrophobic. When the solution is maintained at a concentration of 1.25% TE and 37.5 μM, increasing concentrations of MB cause the flow front to migrate faster, supporting my conclusion that MB interacts with the nitrocellulose. To further support my findings in Figure 6.8B, when the concentration of the solution was kept at a constant 1.25% TE and 0.1 mg/mL (313 μM) MB,

increasing concentrations of release strand caused the dye front to migrate slower. However, this trend only held until the concentration of the release strand was 10 μM, when increasing concentration of release strand caused the dye front to flow faster. This critical point is not when MB and the release strand are in equimolar concentrations. Together, these results demonstrate the importance of selecting an appropriate substrate, buffer, and reporter dye. In order to correlate the concentration of a release strand to the flow rate past a valve, the effect of the release strand concentration on the dye migration rate must be decoupled.
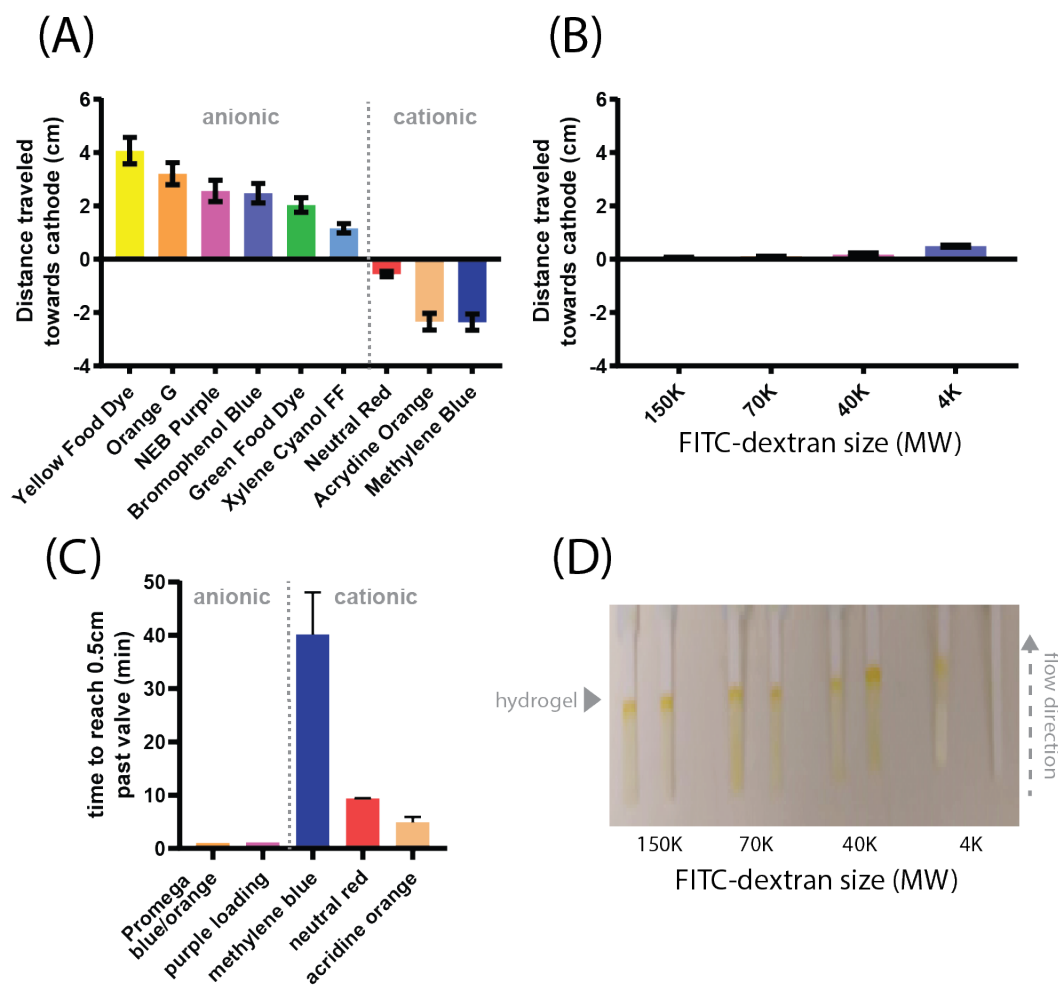

Figure 6.9 Effect of reporter dye charge and size on passage past valve.

(A) Readily-available dyes and (B) FITC labeled dextran molecules' migration through a 1% agarose gel at 100 V for 40 minutes. (C) Only cationic dyes are delayed by a hydrogel valve printed into nitrocellulose membrane. (D) All FITC-dextran molecules larger than 4K were blocked by hydrogel valves for 18 hours. n=2, error bars indicate standard error.
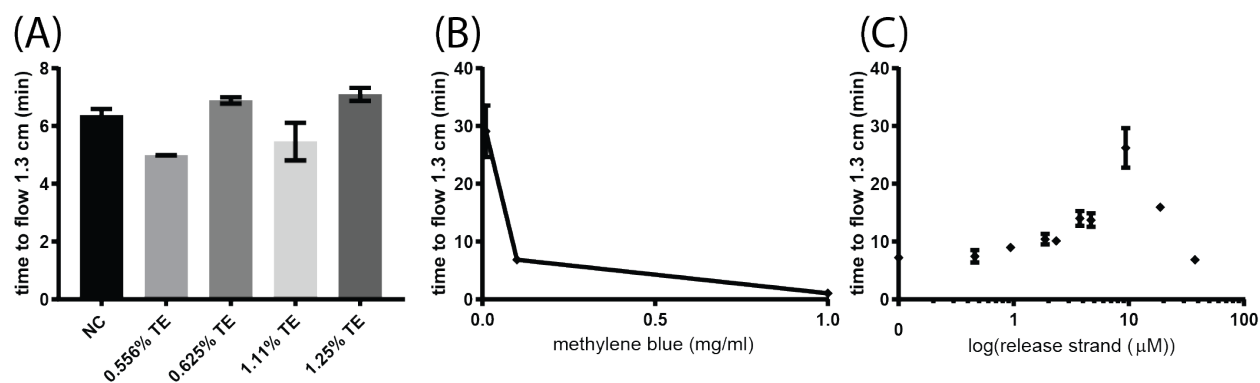
Figure 6.10 Effect of TE buffer, methylene blue, and release strand concentration on dye migration rate in native nitrocellulose membrane.

(A) Solutions with more TE buffer flow slower when methylene blue concentration is kept constant. (B) Solutions with increasing methylene blue concentration flow faster when TE buffer concentration is kept constant. (C) Solutions with increasing concentrations of release strand flow slower until the concentration is 10 μM and then solutions flow slower, when MB and TE is kept constant. n=2, error bars indicate standard error

6.4. Future Directions

6.4.1. DNA-hybrid PEG hydrogel formation

PEG has the added advantage over polyacrylamide of being neutrally charged and less likely to interact with reporter molecules. Moreover, by using a multi-armed PEG as the hydrogel backbone, a greater and controllable proportion of the crosslinks could be composed of DNA than in chain growth polymerization, thus permitting a more sensitive response to strand displacing DNA.

To form a more stable DNA-hybrid hydrogel with PEG, the hydrogel precursor (oligo A or B conjugated to multi-arm PEG) should be concentrated by size-exclusion. PEG monomers with more arms (i.e. 8-arms) would also allow for a more dense hydrogel (this would allow for stoichiometric unity of reactive groups but with a higher w/v% of PEG). To better quantify conjugation by primary amine chemistry with NHS ester, reagents such as TNBS (2,4,6-trinitrobenzene sulfonic acid) could be used to quantify the unreacted primary amines functionalized on oligos. Alternatively, a thiol-ene click reaction could be used to graft oligocluelotides to multi-armed PEG monomers. Also known as the thiol-Michael reaction, this click reaction is an efficient method to conjugate species to polymers[137,139] and has recently been

reported as a strategy to link oligonucleotides to multi-armed PEG to functionalize hydrogels.[140] UV-vis spectroscopy, NMR spectroscopy, and dynamic light scattering have all been used to verify and quantify the efficiency of conjugation.[137,141] Lastly, by including a photo-initiator during the grafting step and using a photomask, the hydrogel could be formed within a porous membrane strip. Photo-initiated hydrogel formation would be a low-cost alternative to printing deposition techniques and would allow for more control over the geometry of a hydrogel valve.

6.4.2. Valve characterization

Upon successful formation in a test membrane, the hydrogel's response (i.e. dissolution) to a target strand should be characterized. By embedding fluorescent nanoparticles into the hydrogel and monitoring their diffusion and Brownian motion in the presence of a target strand, the hydrogel's dissolution kinetics can be extracted.[134] Much like antigen-antibody binding kinetics inform lateral flow immunoassay design, this would help inform, for instance, the spatial location of the valve in a test strip.

A reporter molecule should be identified with a flow rate through a valve that can be decoupled from its interaction with the membrane, target strand, and buffer. A high salt buffer is likely needed to support DNA hybridization, so reporter molecules that are susceptible to aggregation (like gold nanoparticles) should not be used. A labeled molecule, such as dextran, with a hydrodynamic radius larger than the pore size of the hydrogel could be used. The porosity of the hydrogel can be evaluated by scanning electron microscopy and its swelling ratio in order to select the appropriately sized dextran. And while dextran is highly water-soluble and so should not interact with the hydrogel or porous membrane, the labeling may change its effective charge. Candidate labels can be evaluated by calculating the partition coefficient of the hydrogel in the presence of the labeled-dextran solution and selecting labeled-dextrans with an E=1.

Labeled molecules may have an effective charge that will cause an interaction with the nitrocellulose test membrane. To minimize interactions of the reporter dye with the test membrane, a blocking solution (e.g. BSA, casein, and PVP) should be added to the membrane as is done to minimize non-specific interactions in lateral flow immunoassays.[29]

6.5. Conclusion

In this chapter, I demonstrate two different strategies for forming a DNA-hybrid hydrogel: step-growth polymerization by grafting oligonucleotides to PEG and chain-growth polymerization by grafting oligonucleotides to polyacrylamide. While a PEG hydrogel offers greater pore size uniformity than acrylamide, its functionalization with oligonucleotides was more challenging to permit a stable hydrogel. There are several opportunities to overcome this challenge, such as selecting a more efficient conjugation method. Polyacrylamide, however, was easier to functionalize with oligonucleotides and could be crosslinked within a porous membrane. Initial studies indicated that DNA-hybrid hydrogels formed with polyacrylamide backbones dissolved in the presence of a target DNA strand that displaced the crosslinking DNA. Future work can correlate the DNA strand concentration to hydrogel dissolution by monitoring the flow rate of a reporter molecule past the hydrogel. Correlating target concentration with flow rate would provide a distance-based readout that could overcome the interpretation challenges inherent to intensity-based readouts. Ultimately, such a hydrogel could act as a bio-responsive valve and provide an instrument-free signal transduction of pathogenic DNA concentrations.

7. CONCLUSION

This thesis provided several strategies for more specifically detecting infectious pathogens outside of the laboratory on low-cost and instrument-free paper-fluidic diagnostic devices. Nucleic acid amplification assays offer greater detection sensitivity than more conventional immunoassays. However, the sustained incubation requirements of nucleic acid amplification have prevented its implementation in low-cost paper-fluidic formats. In this thesis, I described multiple valving techniques that permit complete fluid obstruction and controlled release within porous membranes. In Chapter 2, I described wax valves that can be readily printed into porous membranes to obstruct fluid and then locally heated to release fluid through discrete reaction zones. Both macro- and micro-analysis techniques were used to identify valve characteristics that can be modified to meet assay needs. For instance, the geometry of the valve influenced both the flow rate of liquid past the valve and the uniformity of flow. Computational simulations of valve heating described in Chapter 3 further illustrated external factors, such as ambient air flow, that impact the uniformity of valve opening. In Chapter 4, I described the utility of wax valves to facilitate multistep and autonomous detection assays. A standard single-step LFIA was transformed into a multi-step LFIA that delivered gold enhancement solution semi-automatically to a test band to more easily detect *E. coli*. Multiple wax valves were integrated into a μPAD to constrain a nucleic acid amplification assay within a porous membrane and then automatically release the amplification products to a downstream LFIA for detection of HIV viruses in whole blood.

In Chapter 5, I described toe-hold mediated strand displacement probes that improve the detection specificity of the isothermal nucleic acid amplification technique, LAMP, by LFIA. Finally, by combining the specificity of toe-hold mediated strand displacement with the flow control of paper-based valving, Chapter 6 described strategies for incorporating target-responsive valves into paper diagnostics. The molecular and fluidic strategies described in this thesis provide a framework for implementing more sensitive and specific assays into low-cost paper-based diagnostics. Ultimately, greater sensitivity of low-cost paper-based diagnostic platforms permits the more rapid identification of disease-causing pathogens, allowing patients to more readily receive appropriate treatment to overcome infectious diseases.

APPENDIX A.SUPPLEMENT TO CHAPTER 2
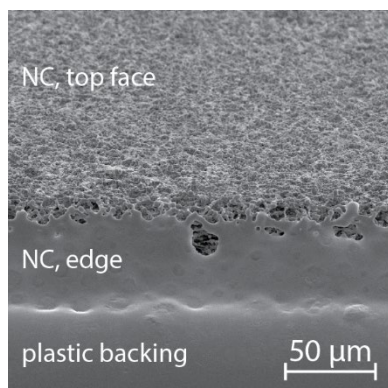
Figure A.1 SEM of laser cut nitrocellulose edge mounted at ~10º angle.

Laser cutting nitrocellulose bevels edge >10º and causes nitrocellulose and/or plastic backing to melt and close pores.
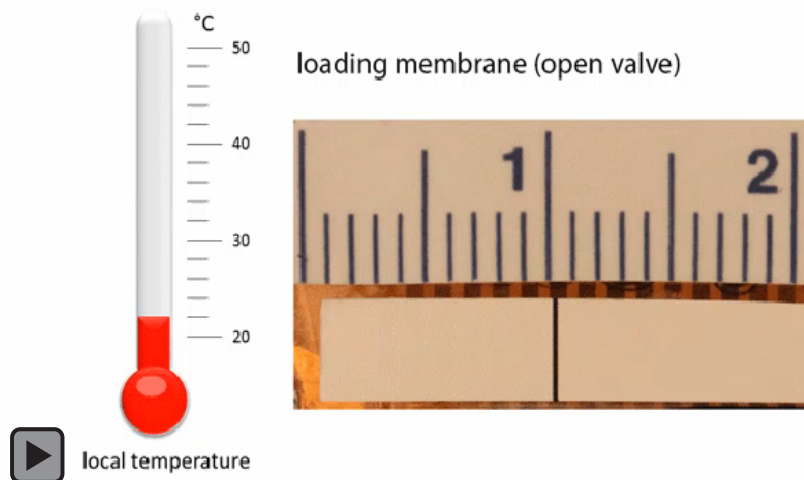

Figure A.2 Video of dye solution migrating through actuated valve in nitrocellulose membrane.
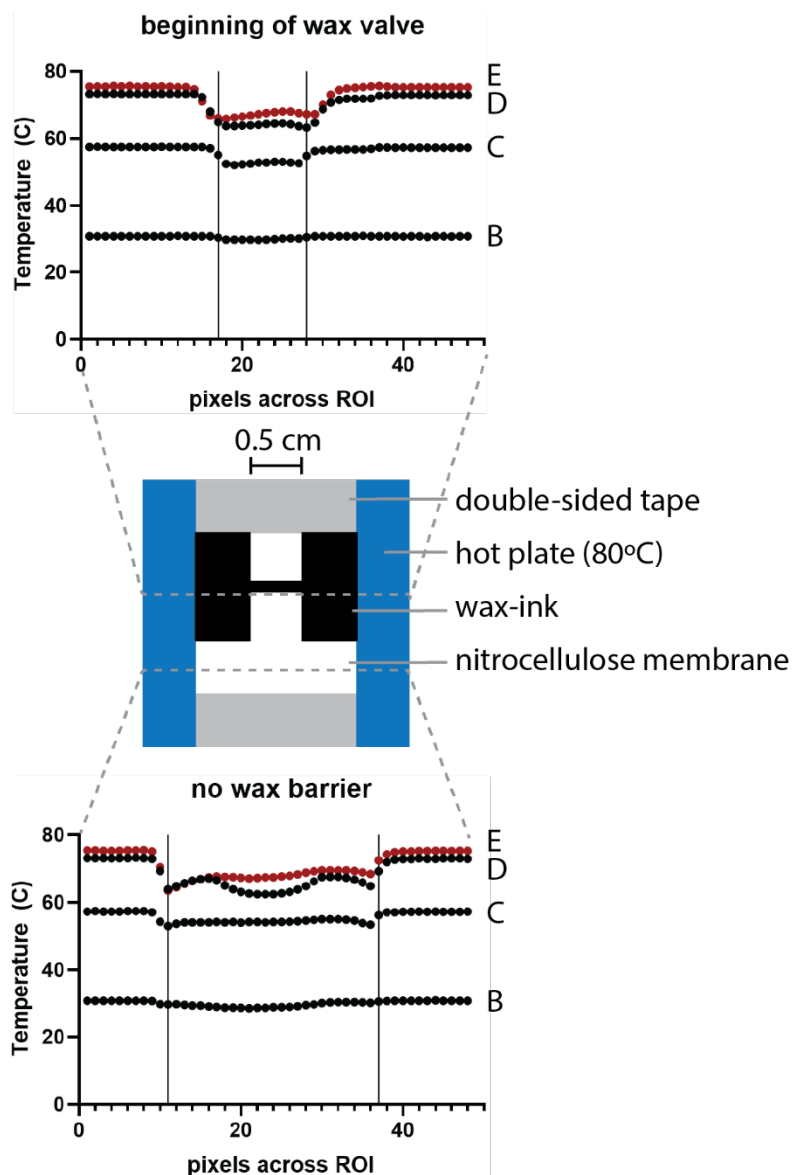
Figure B.1 The temperature profile of a wax-ink valve.

The temperature across the width of the valve immediately preceding the valve and where sample is deposited as extracted from the IR thermal plots in Figure 3.3 . The traces depict when (B) the water sample is constrained by strip edges and wax boundaries when initially deposited. (C) The water remains several degrees below the temperature of the wax even when the wax reaches ~ 56ºC and water is observed migrating along edges of membrane. (D) Water totally evaporated so more was applied to the center of sample region. (E) Water is observed to flow through one edge of the wax valve.

APPENDIX C. SUPPLEMENT TO CHAPTER 4
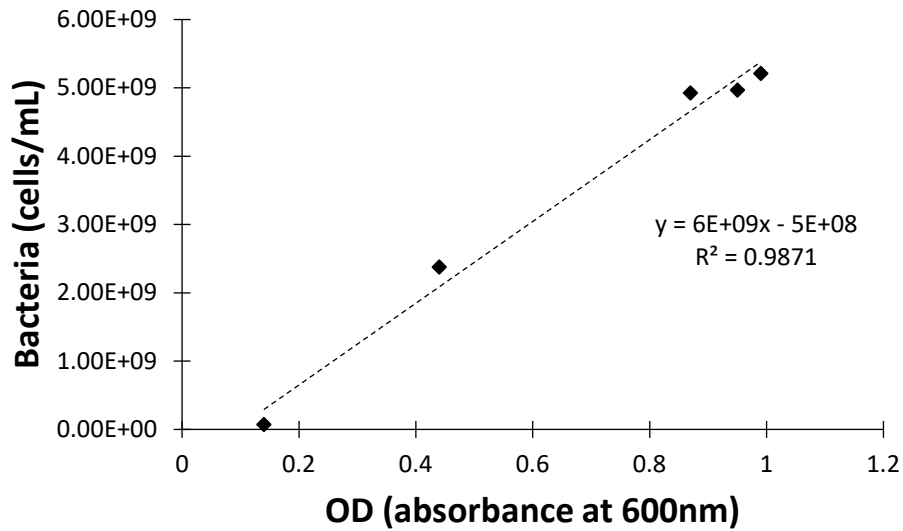
Figure C.1 The optical density of *E.coli* cultures.

E. coli cultures were diluted in LB media were stained with propidium iodide and SYTO9 and subsequently filtered through 0.2µm Isopore membranes (Millipore, Darmstadt, Germany). Cells were then fluorescently imaged and counted by ImageJ and plotted against optical density. The linear relation of Bacteria=6*10^9*Optical Density-5*10^8 with R^2=0.9871 was used for Figure 4.3.

Table C.1 Components and cost of the consumable components of microRAAD.

	Component	Manufacturer	Cost/Device
μPAD	Glass fiber	Millipore	$ 0.02
	MF1 blood separator	GE Life Sciences	<$0.01
	0.22 μm polyethersulfone (PES)	Millipore	$ 0.03
	Wax valve strips	Whatman & Xerox	<$ 0.01
	Cellulose L	Whatman	<$ 0.01
	polyethylene terephthalate (PET)	Apollo	<$ 0.01
	LFIA	USTAR	$ 1.80
	Laminate	Swingline SelfSeal	$ 0.05
	polystyrene gasket	Lohmann Precision Die Cutting	$ 0.01
	Double-sided adhesive	Silhouette	<$ 0.01
		Subtotal	*<$ 1.96*

	Component	Manufacturer	Cost/Device
RT-LAMP Reagents	Isothermal Buffer II	New England Biolabs	$ 0.03
	dNTPs	Agilent Technologies	$ 0.05
	Betaine	Millipore Sigma	$ 0.03
	Primers	Integrated DNA Technologies	$ 0.01
	Bst 3.0 Polymerase	New England Biolabs	$ 0.14
	Sucrose, Glycerol, TritonX-100, green dye, DEPC H2O	Various	$ 0.01
		Subtotal	*$ 0.27*
		Consumable Total	**$ 2.23**

Table C.2 Cut settings on VLS 3.50 Universal Laser Systems CO_2 Laser Cutter

Material	Power	Speed	PPI
FF120HP nitrocellulose	25%	100%	500
Chr1 cellulose	25	100	700
polyethersulfone	10	100	900
(Lohmann) LFIA backing	50	50	500
MF1 glass fiber	15	100	900
acrylic	100	11	1000
acrylic (score)	18.2	24	1000
SelfSeal laminate	25	100	500
SelfSeal laminate (score)	4.8	75	500

Isometric View   **Top View**

polystyrene (x2)
glass fiber
PET
laminate
LFIA

1.

2.   MF1

3.   wax valve 1
            wax valve 2

4.   PES

5.   PET with
   dried reagents
            laminate

10 cm
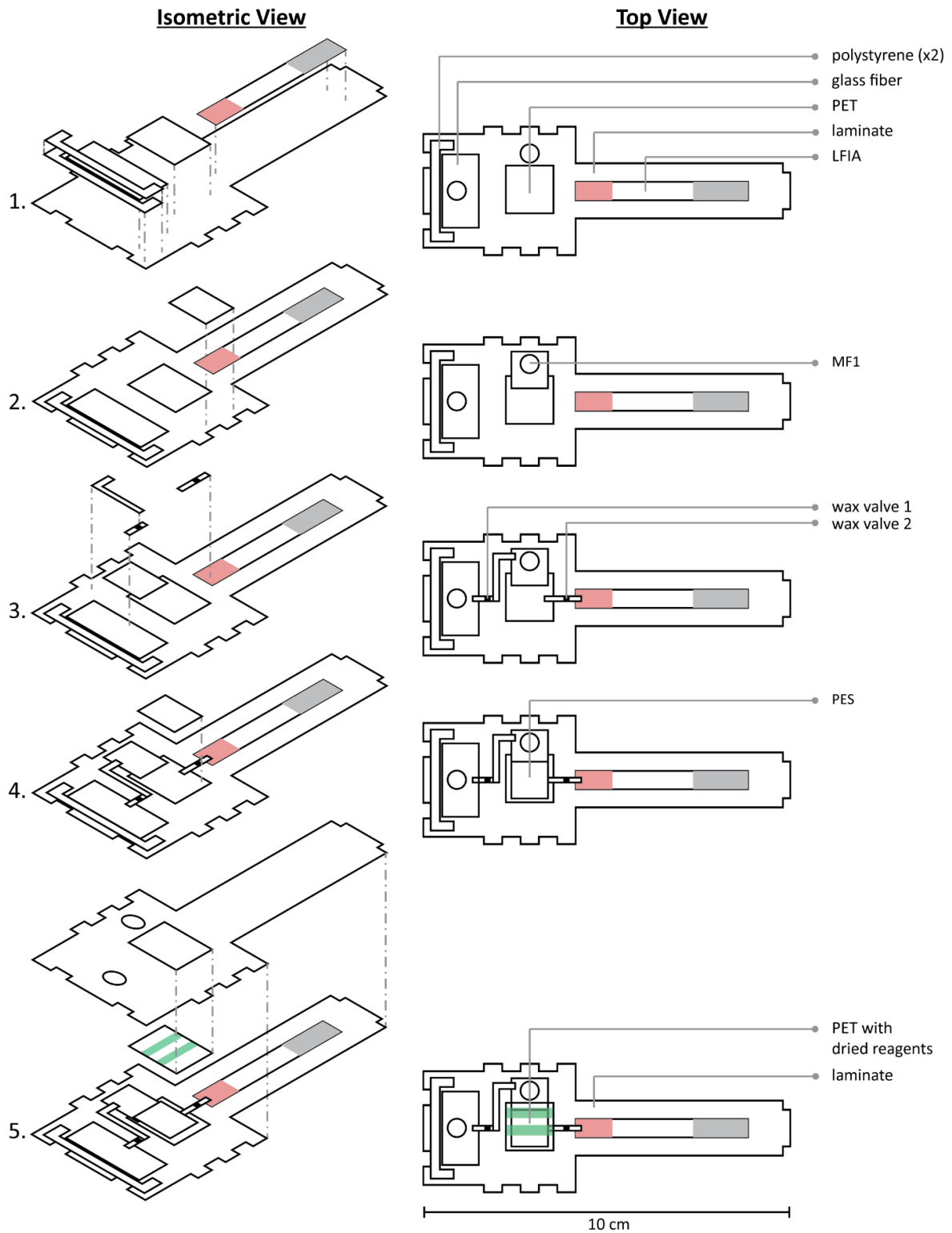
Figure C.2 Assembly of µPAD.

PES was sandwiched with squares of PET to prevent the laminate from inhibiting amplification.

114
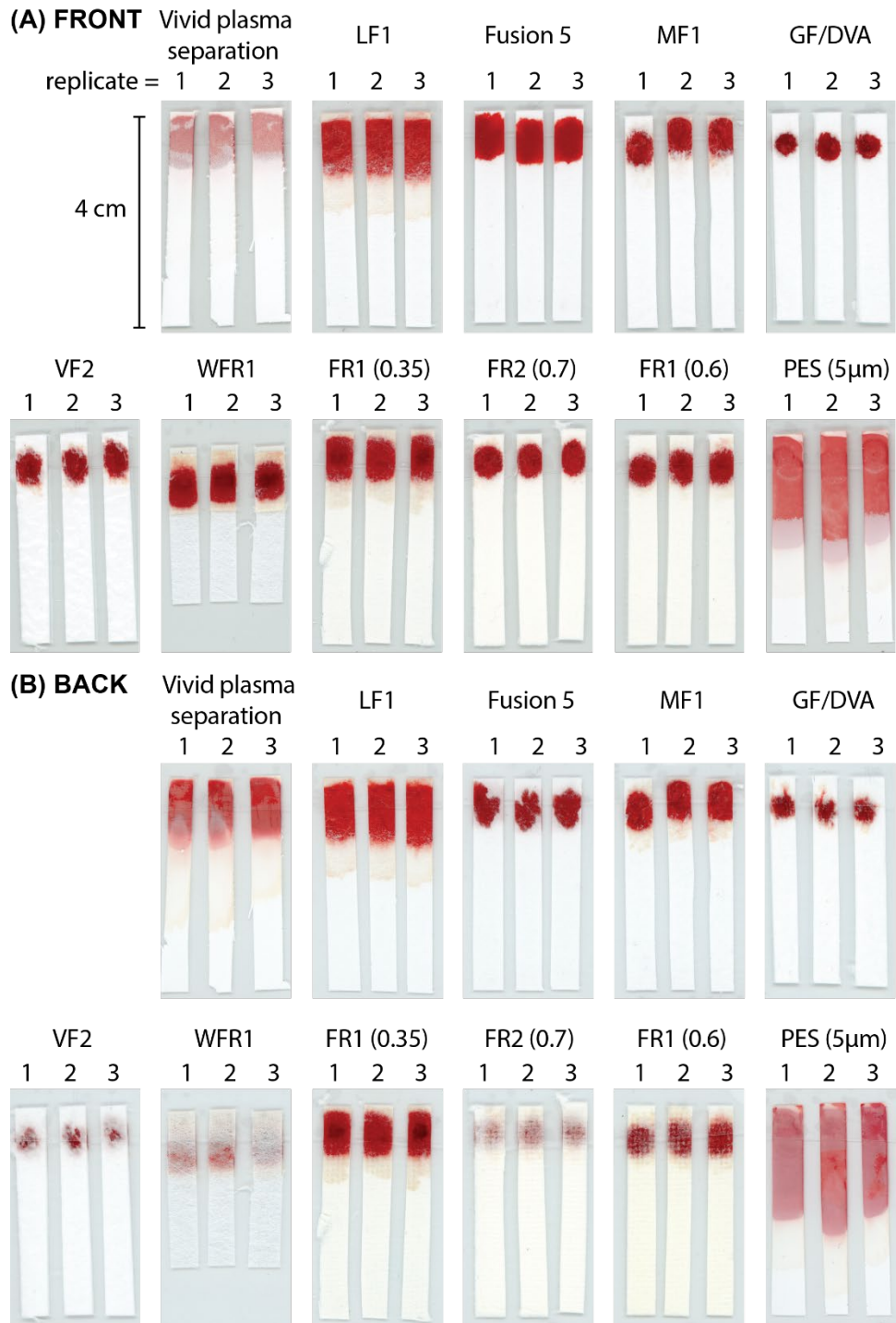
Figure C.3 Scans of blood filtered through commercial membranes.

15µL of blood (collected from 25 year old female donor in sodium citrate tube) was deposited on each 0.5 x 4 cm membrane. After 10 minutes, the (A) front and (B) back of each membrane was scanned
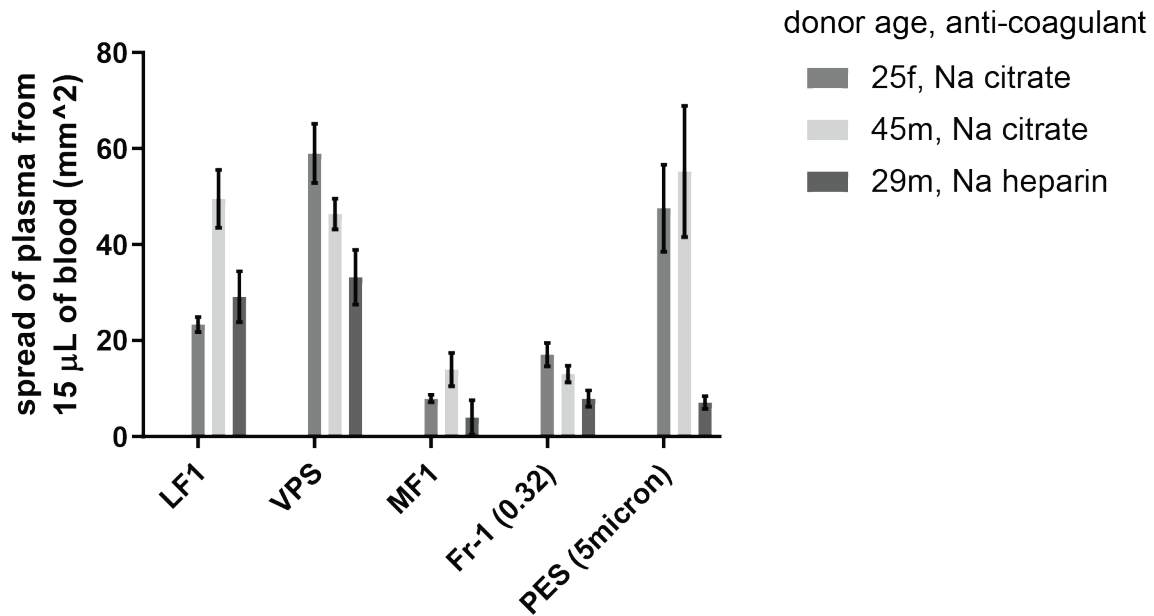
Figure C.4 Effect of blood separation membrane and donor blood on plasma spread.

15μL of blood (collected from 25 year old female and 45 year old male donors in sodium citrate tube and 29 year old male in sodium heparin tube) was deposited on each 0.5 x 4 cm membrane. After 10 minutes, the membrane was scanned and the area of plasma spread measured by ImageJ. n=3 and error bars indicate standard error of the mean.
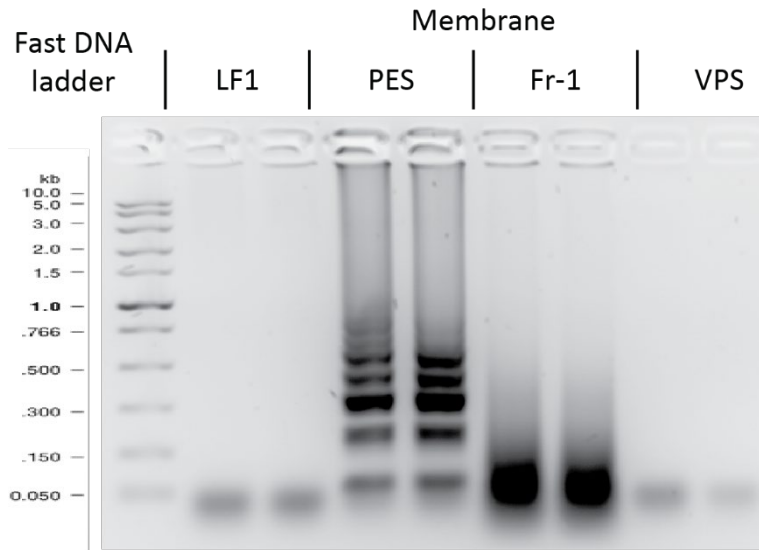

Figure C.5 Effect of blood separation membrane on LAMP.

25μL LAMP reactions with *E. coli* (OD_{600nm}=1) template and 20% blood plasma (collected from 25 year old female in sodium citrate tube) were performed on sealed LF1, PES (5 micron pore size), Fr-1, and VPS blood separation membranes for 1 hour at 65ºC. LAMP product was centrifuged out of the membrane and loaded to a 2% electrophoresis gel. Only amplification products from PES were observed, indicating that other membranes inhibit amplification.
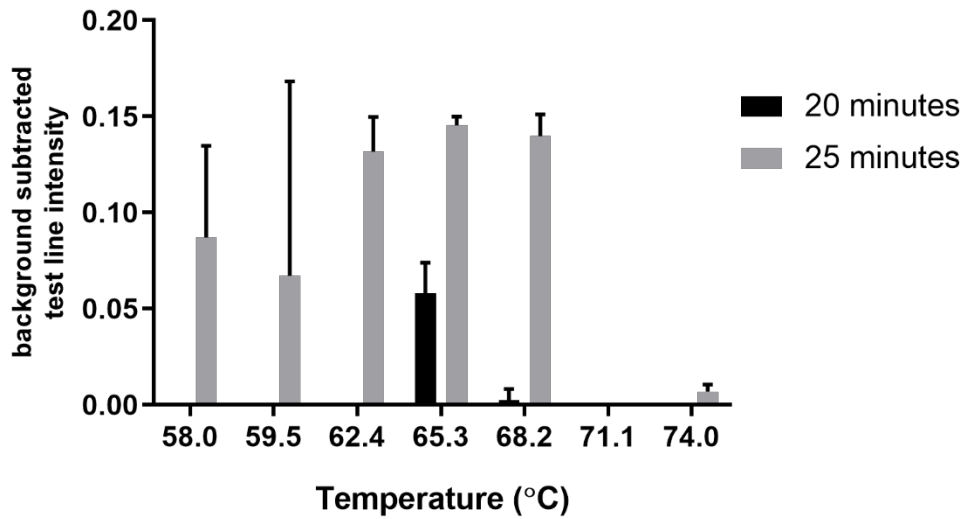
Figure C.6 RT-LAMP assay efficiency at various temperatures

Amplification products were analyzed by LFIA after 20 and 25 minutes of heating at temperatures ranging from 58 - 74 ºC. When heated for 20 minutes, only amplicons heated at 65 ºC were detectable on LFIAs, indicating HIV RT-LAMP is optimally efficient at 65 ºC. n=2
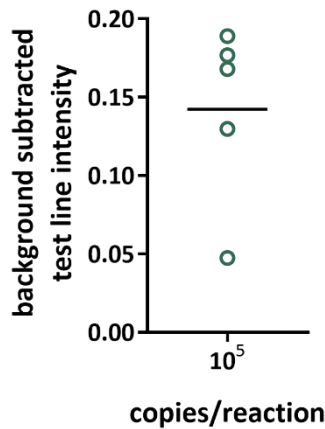

Figure C.7 Test band intensity of LFIAs when HIV virus was diluted in water and loaded with fresh RT-LAMP reagents into the microRAAD. n=5
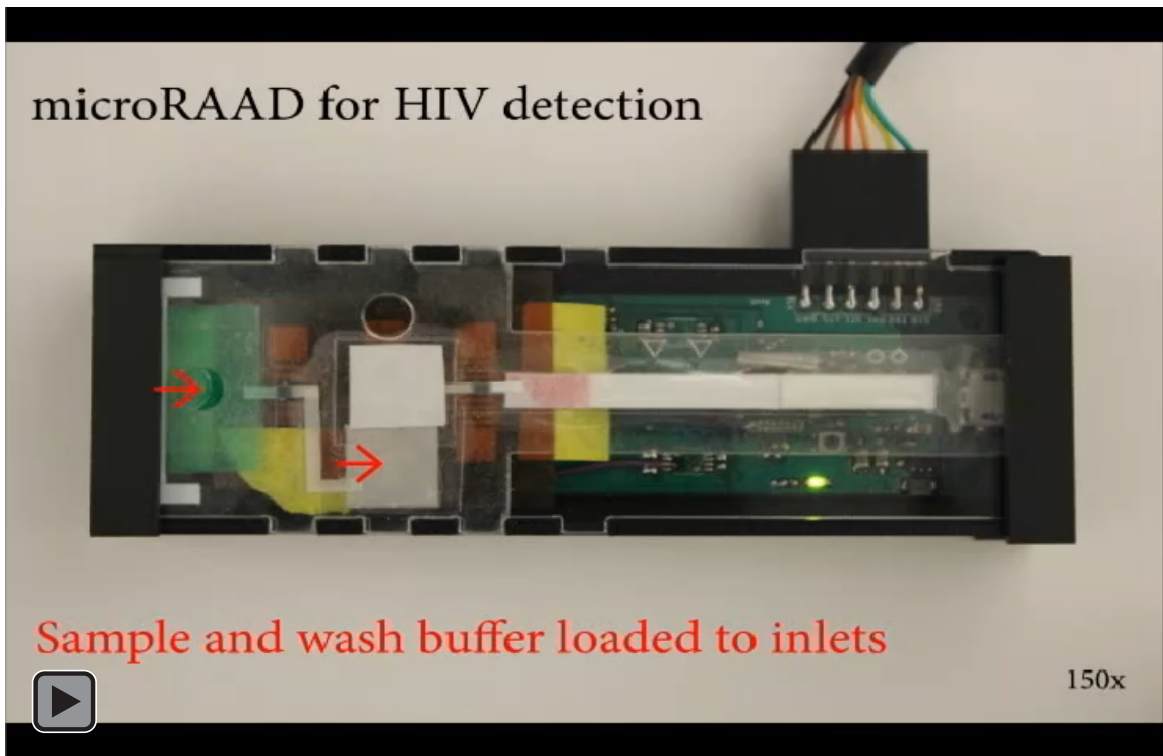
Figure C.8 Video of microRAAD for HIV detection

APPENDIX D. SUPPLEMENT TO CHAPTER 5

Table D.1 Gene target sequences.

Gene Name	Sequence (5'-3')
E. coli malB	GCCATCTCCTGATGACGCATAGTCAGCCCATCATGAATGTTGCTGTC GATGACAGGTTGTTACAAAGGGAGAAGGGCATGGCGAGCGTACAGC TGCAAAATGTAACGAAAGCCTGGGGCGAGGTCGTGGTATCGAAAGA TATCAATCTCGATATCCATGAAGGTGAATTCGTGGTGTTTGTCGGAC CGTCTGGCTGCGGTAAAT
V. cholerae ctxA	GTTTTGATCAATTATTTTTCTGTTAAACAAAGGGAGCATTATATGGT AAAGATAATATTTGTGTTTTTTATTTTCTTATCATCATTTTCATATGC AAATGATGATAAGTTATATCGGGCAGATTCTAGACCTCCTGATGAA ATAAAGCAGTCAGGTGGTCTTATGCCAAGAGGACAGAGTGAGTACT TTGACCGAGGTACTCAAATGAATATCAACCTTTATGATCATGCAAGA GGAACTCAGACGGGATTTGTTAGGCACGATGATGGATATGTTTCCAC CTCAATTAGTTTGAGAAGTGCCCACTTAGTGGGTCAAACTATATTGT CTGGTCATTCTACTTATTATATATATGTTATA

Table D.2 Oligonucleotide primers and probes' sequences.

|	Oligonucleotide	Sequence (5'-3')
E. coli	F3 primer	GCCATCTCCTGATGACGC
	B3 primer	ATTTACCGCAGCCAGACG
	Forward inner primer (FIP)	CATTTTGCAGCTGTACGCTCGCAGCCCATCA TGAATGTTGCT
	Backward inner primer (BIP)	CTGGGGCGAGGTCGTGGTATTCCGACAAAC ACCACGAATT
	Forward loop primer (LF-FAM)	/56-FAM/CTTTGTAACAACCTGTCATCGACA
	Forward loop primer (LF-Biotin)	/5Biosg/CTTTGTAACAACCTGTCATCGACA
	Backward loop primer (LB-FAM)	/56-FAM/ATCAATCTCGATATCCATGAAGGTG
	Backward loop primer (LB-Biotin)	/5Biosg/ATCAATCTCGATATCCATGAAGGTG
	Strand displacement probe	GTCGATGACAGGTTGTTACAAAGGGAGAAG GGCATGGCGA/36-FAM/
	Quencher (displaced) strand	/5IABkFQ/TCGCCATGCCCTTCTCCCTTTGTAA CAAC/3InvdT/
V. cholerae	F3 primer	TCGGGCAGATTCTAGACC
	B3 primer	GTGGGCACTTCTCAAACT
	Forward inner primer (FIP)	TTGAGTACCTCGGTCAAAGTACTTCCTGATG AAATAAAGCAGTCA
	Backward inner primer (BIP)	TCAACCTTTATGATCATGCAAGAGGGGAAA CATATCCATCATCGTG
	Forward loop primer (LF-FAM)	/56-FAM/CCTCTTGGCATAAGACCACC
	Backward loop primer (LB-Biotin)	/5Biosg/AACTCAGACGGGATTTGTTAGG
	Strand displacement probe	/56-FAM/CTGCAGGTGGTCTTATGCCAAGAG GACAGAGTG/3InvdT/
	Quencher (displaced) strand	TCTTGGCATAAGACCACCTGCAG/3IABkFQ/
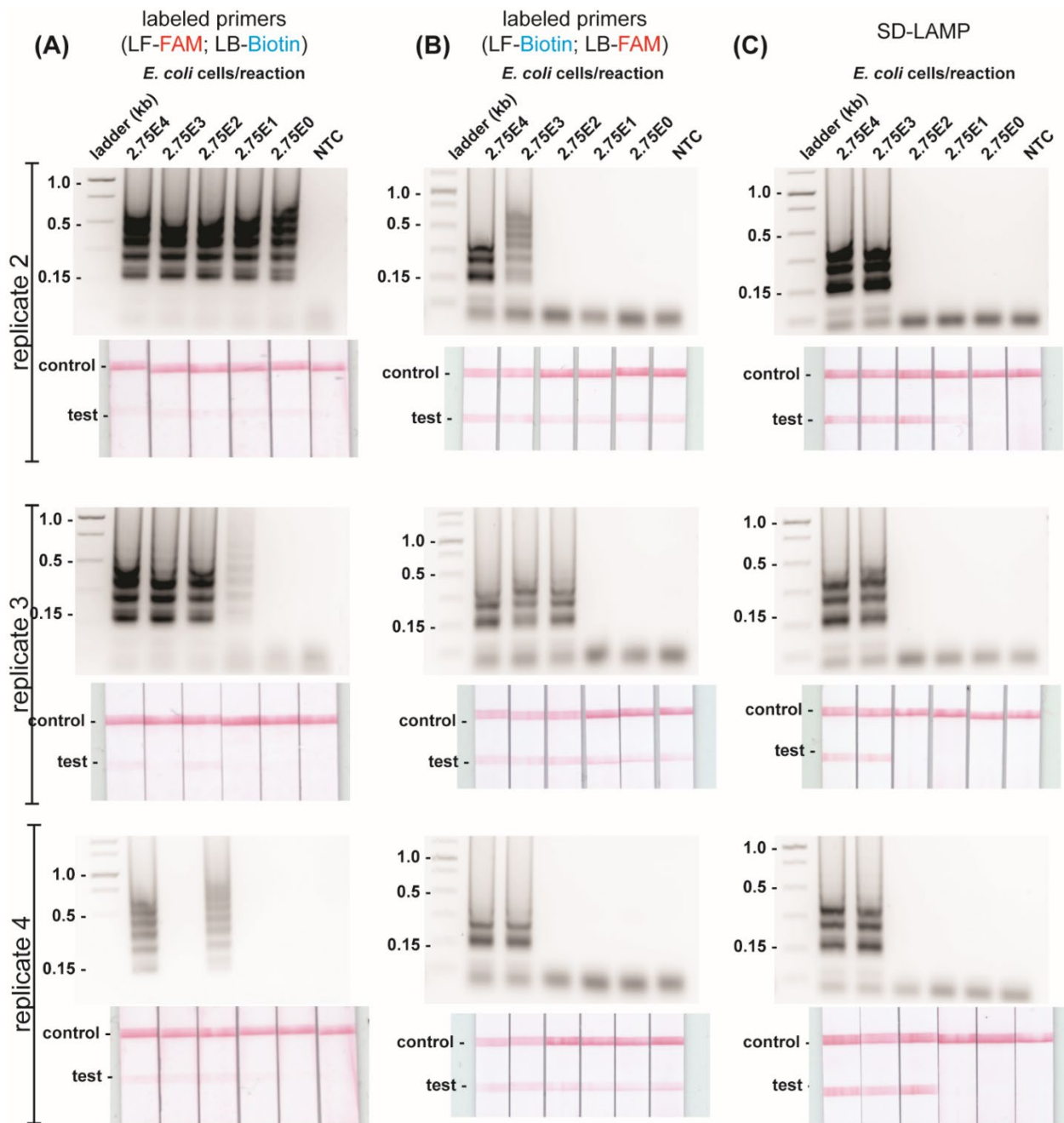
Figure D.1 *E. coli* LAMP amplicons detectable on lateral flow immunoassays (replicates of Figure 5.2)
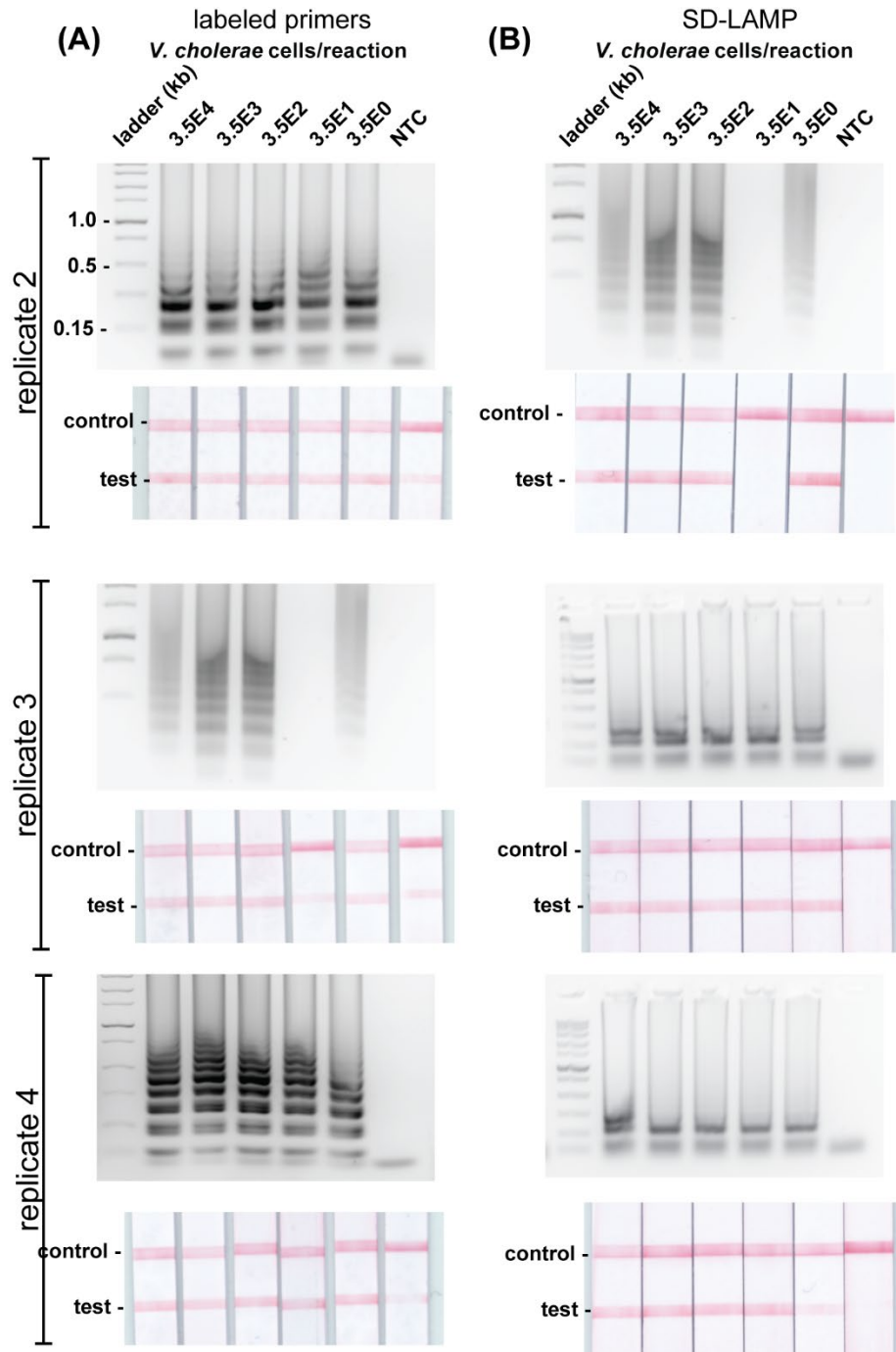
Figure D.2 *V. cholerae* **LAMP amplicons detectable on lateral flow immunoassays (replicates of Figure 5.4)**
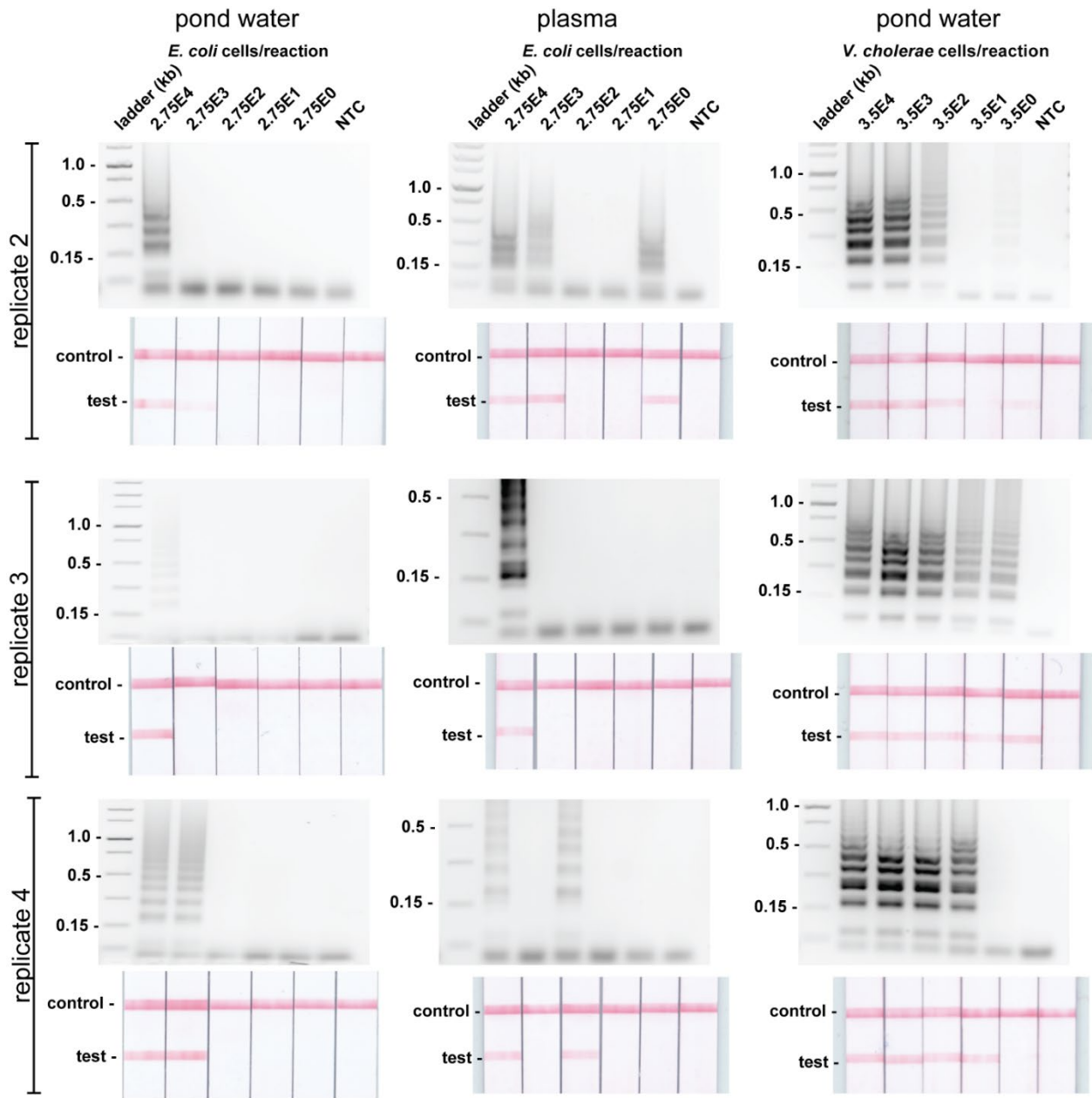
Figure D.3 Probed strand displaced LAMP amplicons detectable from complex matrices (replicates of Figure 5.5)
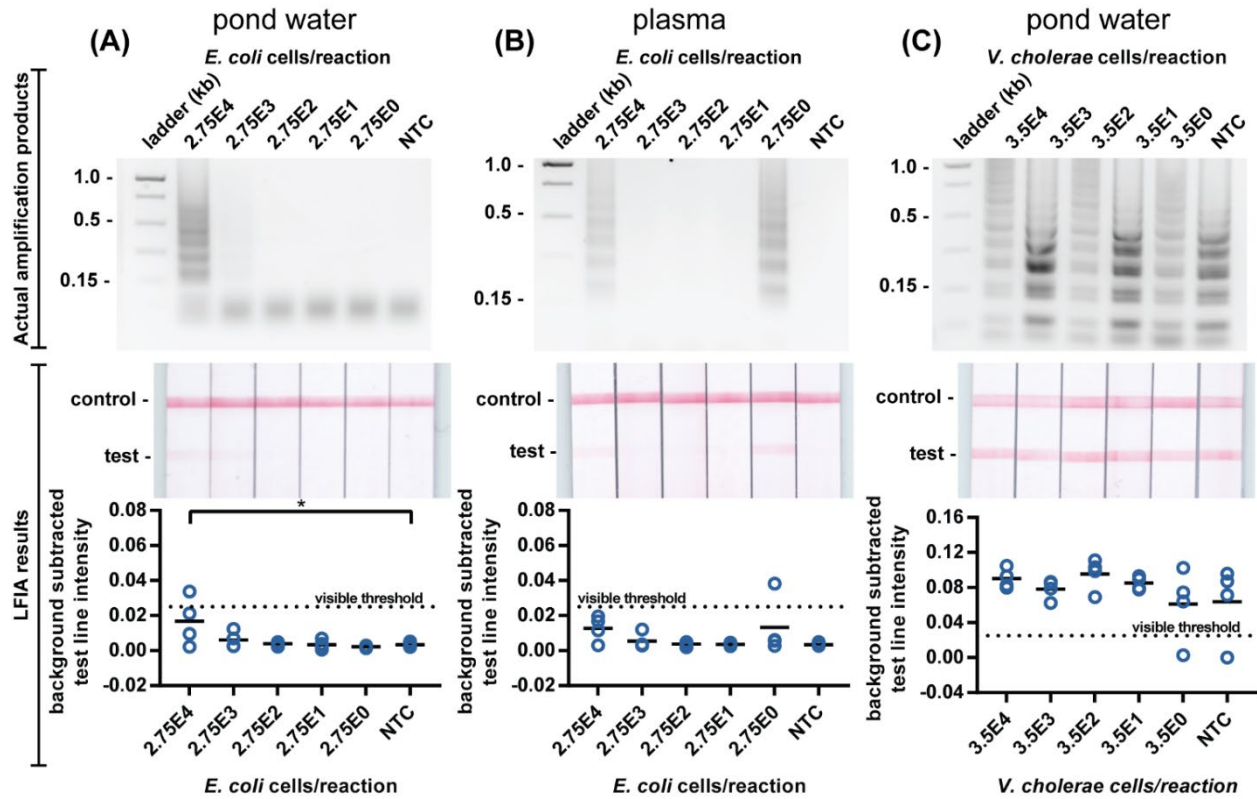
Figure D.4 Detection of standard LAMP reactions in complex matrices.

(top) Electrophoresis gels verifying amplification and indicating inhibited amplification in the presence of pond water and plasma. (middle) LFIA test results and (bottom) LFIA test line quantification. Standard LAMP reactions yield faint LFIA results for *E. coli* diluted in (A) pond water and (B) human plasma. Standard LAMP reactions yield false positive LFIA results for (C) *V. cholerae* diluted in pond water in no template control (NTC) reactions). n=4, replicates indicated by each circle. * indicates p-value ≤ 0.05.
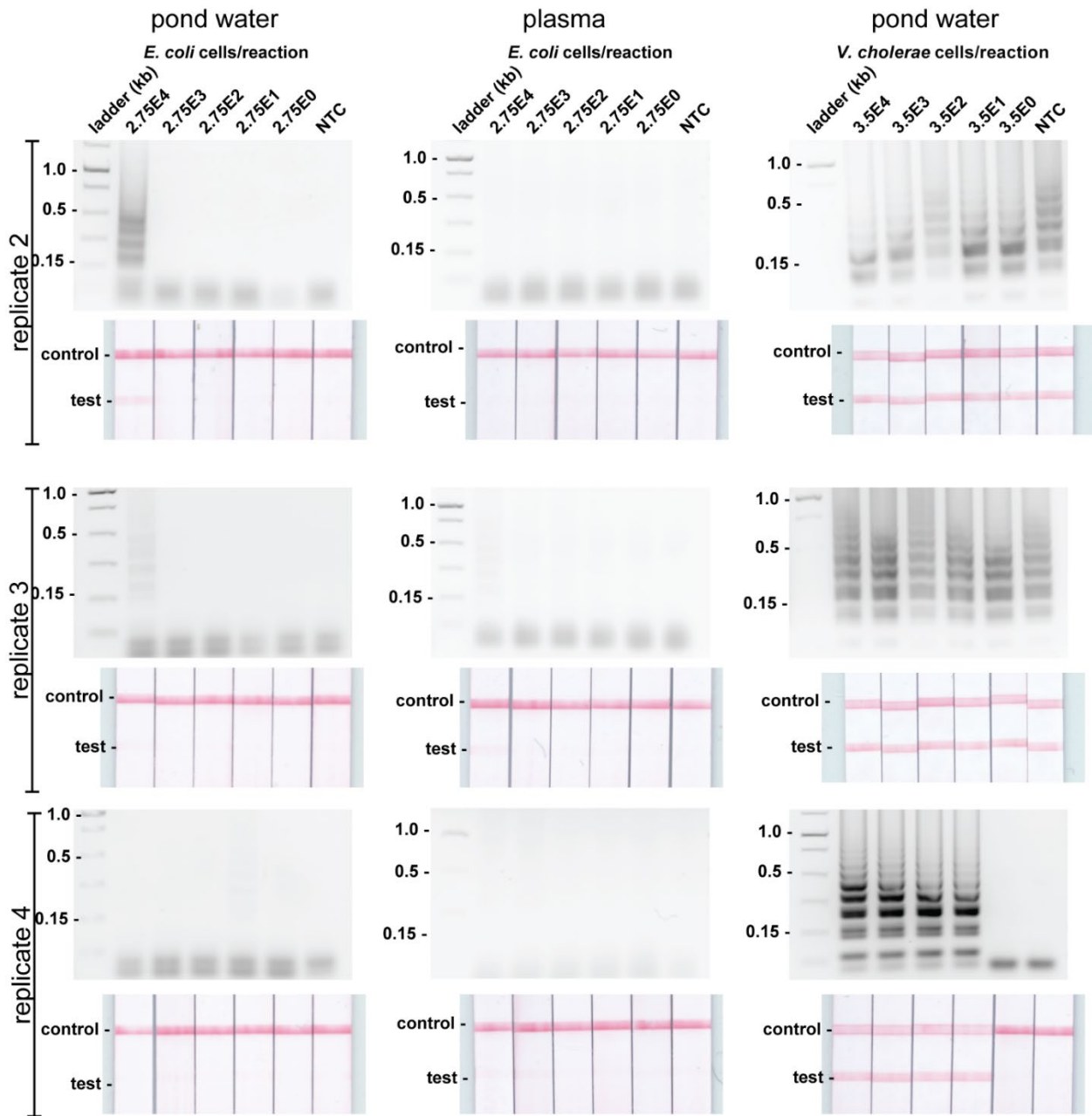
Figure D.5 Standard LAMP amplicons detectable from complex matrices (replicates of Figure D.4)
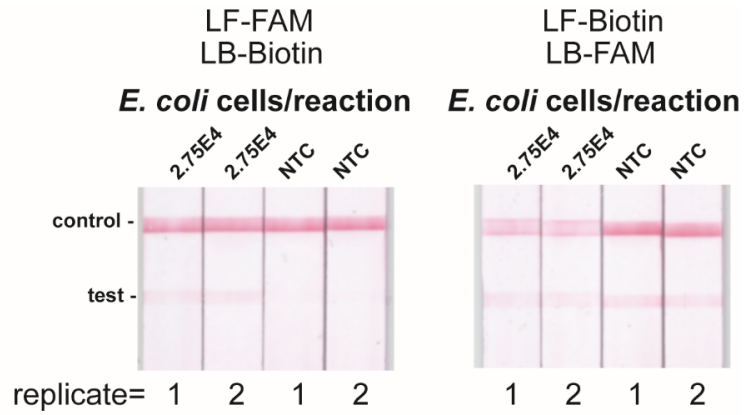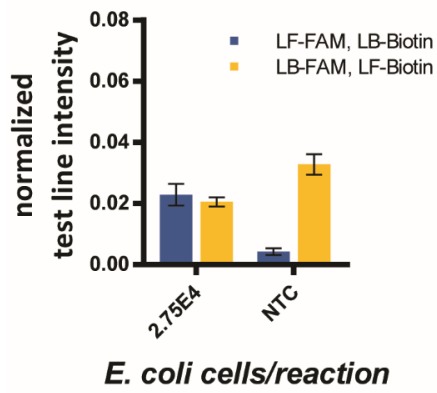
Figure D.6 *E. coli* LAMP with opposite primer tag configurations.
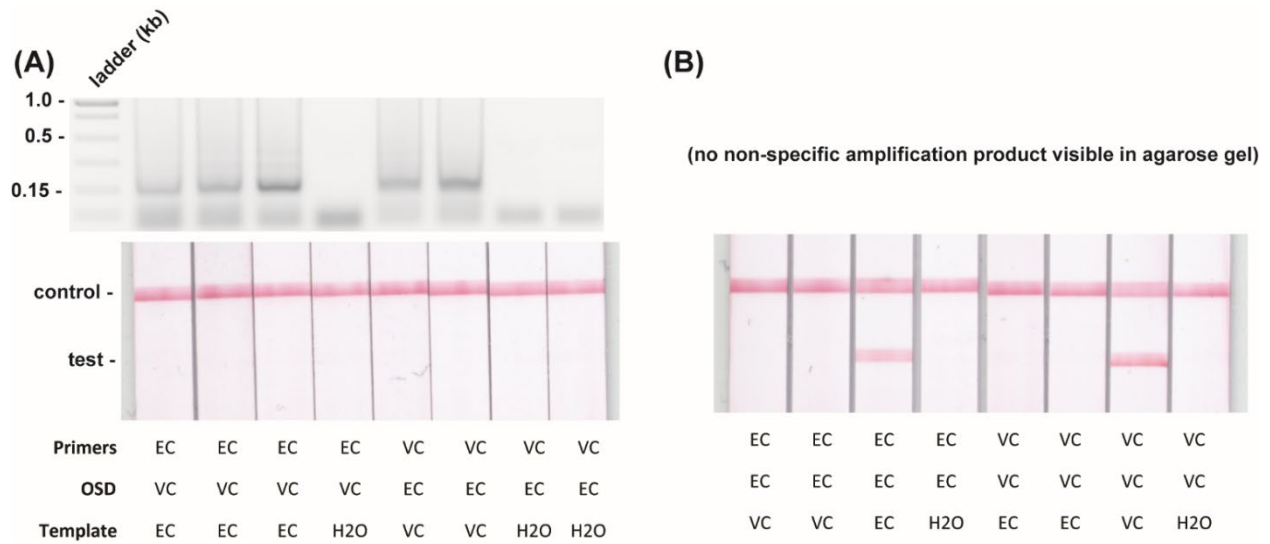
Figure D.7 Strand displacement probes' target specificity.
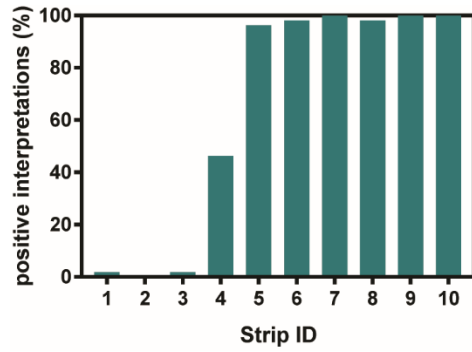
Figure D.8 The percentage of times a test strip was interpreted as positive.

Each strip was evaluated 54 times total (each strip was evaluated indoors, outdoors in the sun, and outdoors in the shade by all 18 participants). Only strips 7, 9, and 10 were interpreted positive all 54 times. Note that only participants with no previous instruction interpreted test strips 5, 6, and 8 as negative.

positive   negative   invalid
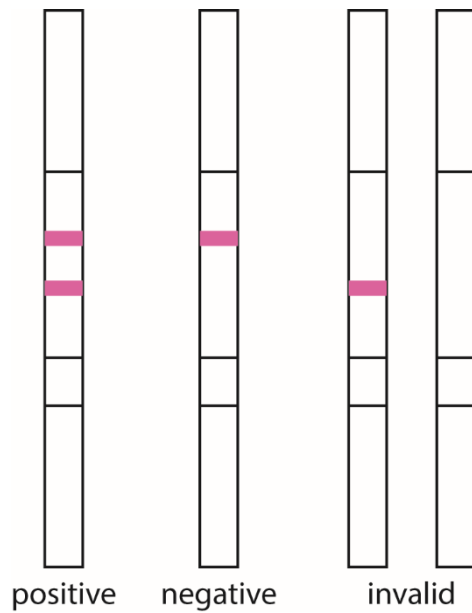
Figure D.9 Schematic provided to test subjects to guide their interpretation of lateral flow tests.
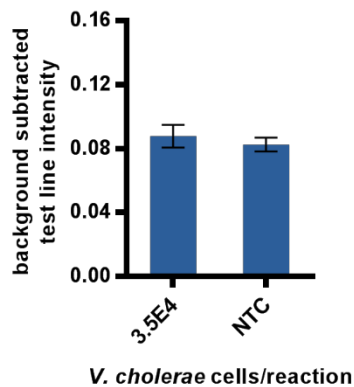
Figure D.10 Standard LAMP reaction of *V. cholerae* with labeled primers containing 0.2 µM each F3 and B3 primers, 1.6 µM each FIP, BIP, LB-biotin primers and 0.05µM LF-FAM primers (the same concentration as FAM tagged strand displacement probe in SD-LAMP reactions of Figure 5.4 in the main text).

When amplification products are loaded to the lateral flow strips, the test line intensity of negative control reactions remains indistinguishable from positive reactions containing template DNA (n=2). This confirms that the decrease in NTC signal observed in SD-LAMP reactions is due to the strand displacement mechanism and not because there is a lower concentration of FAM tagged oligonucleotide.

REFERENCES

1   *Global Health Estimates 2016: Deaths by Cause, Age, Sex, by Country and by Region, 2000-2016.*, World Health Organization, 2018.

2   *Analysis of the Bureau of Economic Analysis Health Care Satellite Account*, Kaiser Family Foundation, 2016.

3   S. Sharma, J. Zapatero-Rodríguez, P. Estrela and R. Kennedy, *Biosensors*, , DOI:10.3390/bios5030577.

4   M. Urdea, L. A. Penny, S. S. Olmsted, M. Y. Giovanni, P. Kaspar, A. Shepherd, P. Wilson, C. A. Dahl, S. Buchsbaum, G. Moeller and D. C. Hay Burgess, *Nature*, 2006, **444**, 73.

5   S. A. Byrnes and B. H. Weigl, *Expert Rev Mol Diagn*, 2018, **18**, 19–26.

6   I. S. Yang, C. Ryu, K. J. Cho, J. K. Kim, S. H. Ong, W. P. Mitchell, B. S. Kim, H.-B. Oh and K. H. Kim, *Nucleic Acids Res.*, 2008, **36**, D455–D460.

7   *Guidance for Clinicians on the Use of Rapid Influenza Diagnostic Tests*, Centers for Disease Control and Prevention.

8   M. A. Speranca, R. B. Suzuki, A. D. Cabral and A. M. dos Santos Carmo, in *Nucleic Acids - From Basic Aspects to Laboratory Tools*, INTECH, pp. 59–74.

9   A. P. of Care, Ed., 2014.

10   A. St John and C. P. Price, *Clin. Biochem. Rev.*, 2014, **35**, 155–167.

11   C. D. Chin, V. Linder and S. K. Sia, *Lab Chip*, 2012, **12**, 2118–2134.

12   J. Park, V. Sunkara, T.-H. Kim, H. Hwang and Y.-K. Cho, *Anal. Chem.*, 2012, **84**, 2133–2140.

13   S. Lai, S. Wang, J. Luo, L. J. Lee, S.-T. Yang and M. J. Madou, *Anal. Chem.*, 2004, **76**, 1832–1837.

14   D. C. Duffy, H. L. Gillis, J. Lin, N. F. Sheppard and G. J. Kellogg, *Anal. Chem.*, 1999, **71**, 4669–4678.

15   M. Focke, F. Stumpf, B. Faltin, P. Reith, D. Bamarni, S. Wadle, C. Muller, H. Reinecke, J. Schrenzel, P. Francois, D. Mark, G. Roth, R. Zengerle and F. von Stetten, *Lab Chip*, 2010, **10**, 2519–2526.

16   Y. Zhang and P. Ozdemir, *Anal Chim Acta*, 2009, **638**, 115–125.

17   E. T. Lagally, C. A. Emrich and R. A. Mathies, *Lab Chip*, 2001, **1**, 102–107.

18   M. J. Heller, *Annu Rev Biomed Eng*, 2002, **4**, 129–153.

19   J. Gao, X. F. Yin and Z. L. Fang, *Lab Chip*, 2004, **4**, 47–52.

20   S. Lindstrom and H. Andersson-Svahn, *Lab Chip*, 2010, **10**, 3363–3372.

21   J. Hu, S. Wang, L. Wang, F. Li, B. Pingguan-Murphy, T. J. Lu and F. Xu, *Biosens. Bioelectron.*, 2014, **54**, 585–597.

22   J. S. Ponti, in *Lateral Flow Immunoassay*, eds. R. Wong and H. Tse, Humana Press, Totowa, NJ, 2009, pp. 1–7.

23   S. Huang, K. Abe, S. Bennett, T. Liang, P. D. Ladd, L. Yokobe, C. E. Anderson, K. Shah, J. Bishop, M. Purfield, P. C. Kauffman, S. Paul, A. E. Welch, B. Strelitz, K. Follmer, K. Pullar, L. Sanchez-Erebia, E. Gerth-Guyette, G. Domingo, E. Klein, J. A. Englund, E. Fu and P. Yager, *Anal Chem*, 2017, **89**, 5776–5783.

24   N. M. Rodriguez, J. C. Linnes, A. Fan, C. K. Ellenson, N. R. Pollock and C. M. Klapperich, *Anal. Chem.*, 2015, **87**, 7872–7879.

25   R. Tang, H. Yang, Y. Gong, M. You, Z. Liu, J. R. Choi, T. Wen, Z. Qu, Q. Mei and F. Xu, *Lab Chip*, 2017, **17**, 1270–1279.

26   L. Lafleur, J. D. Bishop, E. K. Heiniger, R. P. Gallagher, M. D. Wheeler, P. C. Kauffman, X. Zhang, E. Kline, J. Buser, S. Ramachandran, S. Byrnes, N. Vermeulen, N. Scarr, Y. Belousov, W. Mahoney, B. J. Toley, P. D. Ladd, B. Lutz and P. Yager, *Lab Chip*, , DOI:10.1039/C6LC00677A.

27   *Paper Diagnostics Market Analysis By Product (Dipsticks, Lateral Flow Assays), By Device Type (Diagnostic, Monitoring), By Application (Clinical Diagnostics, Cancer, Infectious Diseases, Liver Disorders, Food Quality Testing, Environmental Monitoring), By*, Grand View Research, 2016.

28   B. O'Farrell, in *The Immunoassay Handbook (Fourth Edition)*, Elsevier, Oxford, 2013, pp. 89–107.

29   *Rapid Lateral Flow Test Strips Considerations for Product Development*, EMD Millipore, 2013.

30   S. Byrnes, G. Thiessen and E. Fu, *Bioanalysis*, 2013, **5**, 2821–2836.

31   C. Li, K. Vandenberg, S. Prabhulkar, X. Zhu, L. Schneper, K. Methee, C. J. Rosser and E. Almeide, *Biosens. Bioelectron.*, 2011, **26**, 4342–4348.

32   D. J. Gasperino, D. Leon, B. Lutz, D. M. Cate, K. P. Nichols, D. Bell and B. H. Weigl, *Anal. Chem.*, 2018, **90**, 6643–6650.

33   A. W. Martinez, S. T. Phillips, M. J. Butte and G. M. Whitesides, *Angew. Chemie Int. Ed.*, 2007, **46**, 1318–1320.

34   A. W. Martinez, S. T. Phillips, G. M. Whitesides and E. Carrilho, *Anal. Chem.*, 2010, **82**, 3–10.

35   E. Fu, T. Liang, P. Spicar-Mihalic, J. Houghtaling, S. Ramachandran and P. Yager, *Anal. Chem.*, 2012, **84**, 4574–4579.

36   E. Fu, B. Lutz, P. Kauffman and P. Yager, *Lab Chip*, 2010, **10**, 918–920.

37   A. W. Martinez, S. T. Phillips, Z. Nie, C.-M. Cheng, E. Carrilho, B. J. Wiley and G. M. Whitesides, *Lab Chip*, 2010, **10**, 2499–2504.

38   C. Renault, J. Koehne, A. J. Ricco and R. M. Crooks, *Langmuir*, 2014, **30**, 7030–7036.

39   D. A. Bruzewicz, M. Reches and G. M. Whitesides, *Anal. Chem.*, 2008, **80**, 3387–3392.

40   B. J. Toley, J. A. Wang, M. Gupta, J. R. Buser, L. K. Lafleur, B. R. Lutz, E. Fu and P. Yager, *Lab Chip*, 2015, **15**, 1432–1444.

41   L. Magro, C. Escadafal, P. Garneret, B. Jacquelin, A. Kwasiborski, J. C. Manuguerra, F. Monti, A. Sakuntabhai, J. Vanhomwegen, P. Lafaye and P. Tabeling, *Lab Chip*, 2017, **17**, 2347–2371.

42   A. Niemz, T. M. Ferguson and D. S. Boyle, *Trends Biotechnol.*, 2011, **29**, 240–250.

43   G. A. Posthuma-Trumpie, J. Korf and A. van Amerongen, *Anal. Bioanal. Chem.*, 2009, **393**, 569–582.

44   S. A. Nierzwicki-Bauer, J. S. Gebhardt, L. Linkkila and K. Walsh, *Biotechniques*, 1990, **9**, 472–478.

45   M. Jauset-Rubio, M. Svobodová, T. Mairal, C. McNeil, N. Keegan, A. Saeed, M. N. Abbas, M. S. El-Shahawi, A. S. Bashammakh, A. O. Alyoubi and C. K. O´Sullivan, *Sci. Rep.*, 2016, **6**, 37732.

46   M. A. Dineva, D. Candotti, F. Fletcher-Brown, J.-P. Allain and H. Lee, *J. Clin. Microbiol.*, 2005, **43**, 4015–4021.

47   W. Kiatpathomchai, W. Jaroenram, N. Arunrut, S. Jitrapakdee and T. W. Flegel, *J. Virol. Methods*, 2008, **153**, 214–217.

48   J. Singleton, J. L. Osborn, L. Lillis, K. Hawkins, D. Guelig, W. Price, R. Johns, K. Ebels, D. Boyle, B. Weigl and P. LaBarre, *PLoS One*, 2014, **9**, e113693.

49   C. S. Ball, Y. K. Light, C.-Y. Koh, S. S. Wheeler, L. L. Coffey and R. J. Meagher, *Anal. Chem.*, 2016, **88**, 3562–3568.

50   N. A. Tanner, Y. Zhang and T. C. Evans Jr., *Biotechniques*, 2012, **53**, 81–89.

51   Y. S. Jiang, S. Bhadra, B. Li, Y. R. Wu, J. N. Milligan and A. D. Ellington, *Anal Chem*, 2015, **87**, 3314–3320.

52   Y. Du, A. Pothukuchy, J. D. Gollihar, A. Nourani, B. Li and A. D. Ellington, *Angew. Chemie Int. Ed.*, 2017, **56**, 992–996.

53   K. Scida, B. Li, A. D. Ellington and R. M. Crooks, *Anal. Chem.*, 2013, **85**, 9713–9720.

54   P. B. Allen, S. A. Arshad, B. Li, X. Chen and A. D. Ellington, *Lab Chip*, 2012, **12**, 2951–2958.

55   P. Yin, H. M. T. Choi, C. R. Calvert and N. A. Pierce, *Nature*, 2008, **451**, 318–322.

56   K. Pardee, A. A. Green, T. Ferrante, D. E. Cameron, A. DaleyKeyser, P. Yin and J. J. Collins, *Cell*, 2016, **159**, 940–954.

57   K. Pardee, A. A. Green, M. K. Takahashi, D. Braff, G. Lambert, J. W. Lee, T. Ferrante, D. Ma, N. Donghia, M. Fan, N. M. Daringer, I. Bosch, D. M. Dudley, D. H. O'Connor, L. Gehrke and J. J. Collins, *Cell*, 2016, **165**, 1255–1266.

58   E. Fu, *Analyst*, 2014, **139**, 4750–4757.

59   S. Lathwal and H. D. Sikes, *Lab Chip*, 2016, **16**, 1374–1382.

60   A. A. Kumar, J. W. Hennek, B. S. Smith, S. Kumar, P. Beattie, S. Jain, J. P. Rolland, T. P. Stossel, C. Chunda-Liyoka and G. M. Whitesides, *Angew Chem Int Ed Engl*, 2015, **54**, 5836–5853.

61   D. M. Cate, S. D. Noblitt, J. Volckens and C. S. Henry, *Lab Chip*, 2015, **15**, 2808–2818.

62   D. M. Cate, W. Dungchai, J. C. Cunningham, J. Volckens and C. S. Henry, *Lab Chip*, 2013, **13**, 2397–2404.

63   X. Wei, T. Tian, S. Jia, Z. Zhu, Y. Ma, J. Sun, Z. Lin and C. J. Yang, *Anal. Chem.*, , DOI:10.1021/acs.analchem.5b04294.

64   T. Tian, J. Li, Y. Song, L. Zhou, Z. Zhu and C. J. Yang, *Lab Chip*, 2016, **16**, 1139–1151.

65   A. M. Caliendo, D. N. Gilbert, C. C. Ginocchio, K. E. Hanson, L. May, T. C. Quinn, F. C. Tenover, D. Alland, A. J. Blaschke, R. A. Bonomo, K. C. Carroll, M. J. Ferraro, L. R. Hirschhorn, W. P. Joseph, T. Karchmer, A. T. MacIntyre, L. B. Reller, A. F. Jackson and A. for the Infectious Diseases Society of, *Clin. Infect. Dis. An Off. Publ. Infect. Dis. Soc. Am.*, 2013, **57**, S139–S170.

66   T. Tian, Y. An, Y. Wu, Y. Song, Z. Zhu and C. Yang, *ACS Appl. Mater. Interfaces*, 2017, **9**, 30480–30487.

67   A. G. Wang, T. Dong, H. Mansour, G. Matamoros, A. L. Sanchez and F. Li, *ACS Sensors*, 2018, **3**, 205–210.

68   S. Roy, I. A. Rahman and M. U. Ahmed, *Anal. Methods*, 2016, **8**, 2391–2399.

69   X. Wei, T. Tian, S. Jia, Z. Zhu, Y. Ma, J. Sun, Z. Lin and C. J. Yang, *Anal. Chem.*, 2015, **87**, 4275–4282.

70   N. A. Tanner and T. C. Evans, in *Current Protocols in Molecular Biology*, John Wiley & Sons, Inc., vol. 105, pp. 1–14.

71   E. Carrilho, A. W. Martinez and G. M. Whitesides, *Anal. Chem.*, 2009, **81**, 7091–7095.

72   S. S. Modak, C. A. Barber, E. Geva, W. R. Abrams, D. Malamud and Y. S. Y. Ongagna, *Infect. Dis. (Auckl).*, 2016, **9**, 1–9.

73   P. Francois, M. Tangomo, J. Hibbs, E.-J. Bonetti, C. C. Boehme, T. Notomi, M. D. Perkins and J. Schrenzel, *FEMS Immunol. Med. Microbiol.*, 2011, **62**, 41–48.

74   I. Sotiriadou and P. Karanis, *Diagn. Microbiol. Infect. Dis.*, 2008, **62**, 357–365.

75   M. L. Previtera and N. A. Langrana, *J. Vis. Exp.*, 2014, 51323.

76   J. Li, L. Mo, C.-H. Lu, T. Fu, H.-H. Yang and W. Tan, *Chem. Soc. Rev.*, 2016, **45**, 1410–1431.

77   H. Yang, H. Liu, H. Kang and W. Tan, *J. Am. Chem. Soc.*, 2008, **130**, 6320–6321.

78   E. A. Phillips, R. Shen, S. Zhao and J. C. Linnes, *Lab Chip*, 2016, **16**, 4230–4236.

79   G. E. Fridley, H. Le and P. Yager, *Anal. Chem.*, 2014, **86**, 6447–6453.

80   E. Fu, P. Kauffman, B. Lutz and P. Yager, *Sensors Actuators B Chem.*, 2010, **149**, 325–328.

81   Y. Ouyang, S. Wang, J. Li, P. S. Riehl, M. Begley and J. P. Landers, *Lab Chip*, 2013, **13**, 1762–1771.

82   H. Noh and S. T. Phillips, *Anal. Chem.*, 2010, **82**, 8071–8078.

83   B. J. Toley, B. McKenzie, T. Liang, J. R. Buser, P. Yager and E. Fu, *Anal. Chem.*, 2013, **85**, 11545–11552.

84   J. Houghtaling, T. Liang, G. Thiessen and E. Fu, *Anal. Chem.*, 2013, **85**, 11201–11204.

85   B. Lutz, T. Liang, E. Fu, S. Ramachandran, P. Kauffman and P. Yager, *Lab Chip*, 2013, **13**, 2840–2847.

86   S. Jahanshahi-Anbuhi, A. Henry, V. Leung, C. Sicard, K. Pennings, R. Pelton, J. D. Brennan and C. D. M. Filipe, *Lab Chip*, 2014, **14**, 229–236.

87   H. Chen, J. Cogswell, C. Anagnostopoulos and M. Faghri, *Lab Chip*, 2012, **12**, 2909–2913.

88   X. Li, P. Zwanenburg and X. Liu, *Lab Chip*, 2013, **13**, 2609–2614.

89   S. Jahanshahi-Anbuhi, P. Chavan, C. Sicard, V. Leung, S. M. Hossain, R. Pelton, J. D. Brennan and C. D. Filipe, *Lab Chip*, 2012, **12**, 5079–5085.

90   N. M. Rodriguez, W. S. Wong, L. Liu, R. Dewar and C. M. Klapperich, *Lab Chip*, 2016, **16**, 753–763.

91   B. R. Lutz, P. Trinh, C. Ball, E. Fu and P. Yager, *Lab Chip*, 2011, **11**, 4274–4278.

92   J. T. Connelly, J. P. Rolland and G. M. Whitesides, *Anal Chem*, 2015, **87**, 7595–7601.

93   K. N. Han, J.-S. Choi and J. Kwon, *Sci. Rep.*, 2016, **6**, 25710.

94   C. K. Koo, F. He and S. R. Nugen, *Analyst*, 2013, **138**, 4998–5004.

95   G. E. Fridley, H. Q. Le, E. Fu and P. Yager, *Lab Chip*, 2012, **12**, 4321–4327.

96   C. Downs, A. Nejely and E. Fu, *Anal. Methods*, 2019, **11**, 5098–5107.

97   A. Pal, H. E. Cuellar, R. Kuang, H. F. N. Caurin, D. Goswami and R. V. Martinez, *Adv. Mater. Technol.*, 2017, **2**, 1700130.

98   J. Tirapu-Azpiroz, A. Fereira Silva, M. Esteves Ferreira, W. F. Lopez Candela, P. W. Bryant, M. Engel, R. L. Ohta and M. B. Steiner, in *Microfluidics, BioMEMS, and Medical Microsystems XVI*, eds. B. L. Gray and H. Becker, SPIE, 2018, vol. 10491, p. 4.

99   C. Castro, C. Rosillo and H. Tsutsui, *Microfluid. Nanofluidics*, 2017, **21**, 21.

100   S. Altundemir, A. K. Uguz and K. Ulgen, *Biomicrofluidics*, 2017, **11**, 041501.

101   T. Rosenfeld and M. Bercovici, *Lab Chip*, 2014, **14**, 4465–4474.

102   J. R. Buser, S. Diesburg, J. Singleton, D. Guelig, J. D. Bishop, C. Zentner, R. Burton, P. LaBarre, P. Yager and B. H. Weigl, *Lab Chip*, 2015, **15**, 4423–4432.

103   K. M. Byers, L.-K. Lin, T. J. Moehling, L. Stanciu and J. C. Linnes, *Analyst*, , DOI:10.1039/C9AN01546A.

104   Z. Chen, J. Wang, S. Qian and H. H. Bau, *Lab Chip*, 2005, **5**, 1277.

105   M. Mansfield, in *Lateral Flow Immunoassay*, Humana Press, New York, 2009, pp. 95–113.

106   *Evaporation in Porous Media with Large Evaporation Rates*, .

107   S. A. Lavrykov and B. V. Ramarao, *Dry. Technol.*, 2012, **30**, 297–311.

108   R. Li, University of Toronto, 2008.

109   COMSOL, *Coupled Flow Laws*, 2008.

110   E. A. Phillips, R. Shen, S. Zhao and J. C. Linnes, *Lab Chip*, 2016, **16**, 4230–4236.

111   E. A. Phillips, T. J. Moehling, K. F. K. Ejendal, O. S. Hoilett, K. M. Byers, L. A. Basing, L. A. Jankowski, J. B. Bennett, L.-K. Lin, L. A. Stanciu and J. C. Linnes, *Lab Chip*, 2019, **19**, 3375–3386.

112   J. D. Bishop, H. V. Hsieh, D. J. Gasperino and B. H. Weigl, *Lab Chip*, 2019, **19**, 2486–2499.

113   Y. FUCHIWAKI, K. GOYA and M. TANAKA, *Anal. Sci.*, 2018, **34**, 57–63.

114   V. G. Panferov, I. V. Safenkova, Y. A. Varitsev, N. V. Drenova, K. P. Kornev, A. V. Zherdev and B. B. Dzantiev, *Talanta*, 2016, **152**, 521–530.

115   Z. Chen, W. R. Abrams, E. Geva, C. J. de Dood, J. M. González, H. J. Tanke, R. S. Niedbala, P. Zhou, D. Malamud and P. L. A. M. Corstjens, *Biomed Res. Int.*, 2013, **2013**, 543294.

116   L. K. Lafleur, J. D. Bishop, E. K. Heiniger, R. P. Gallagher, M. D. Wheeler, P. Kauffman, X. Zhang, E. C. Kline, J. R. Buser, S. Kumar, S. A. Byrnes, N. M. J. Vermeulen, N. K. Scarr, Y. Belousov, W. Mahoney, B. J. Toley, P. D. Ladd, B. R. Lutz and P. Yager, *Lab Chip*, 2016, **16**, 3777–3787.

117   J. R. Choi, R. Tang, S. Wang, W. A. B. Wan Abas, B. Pingguan-Murphy and F. Xu, *Biosens. Bioelectron.*, 2015, **74**, 427–439.

118   J. C. Linnes, N. M. Rodriguez, L. Liu and C. M. Klapperich, *Biomed. Microdevices*, 2016, **18**, 30.

119   A. L. Horst, J. M. Rosenbohm, N. Kolluri, J. Hardick, C. A. Gaydos, M. Cabodi, C. M. Klapperich and J. C. Linnes, *Biomed. Microdevices*, 2018, **20**, 35.

120   C. Liu, E. Geva, M. Mauk, X. Qiu, W. R. Abrams, D. Malamud, K. Curtis, S. M. Owen and H. H. Bau, *Analyst*, 2011, **136**, 2069.

121   G. L. Damhorst, C. Duarte-Guevara, W. Chen, T. Ghonge, B. T. Cunningham and R. Bashir, *Eng. (Beijing, China)*, 2015, **1**, 324–335.

122   E. A. Phillips, T. J. Moehling, S. Bhadra, A. D. Ellington and J. C. Linnes, *Anal. Chem.*, 2018, **90**, 6580–6586.

123   C. A. Holstein, University of Washington, 2015.

124   J. Hill, S. Beriwal, I. Chandra, V. K. Paul, A. Kapil, T. Singh, R. M. Wadowsky, V. Singh, A. Goyal, T. Jahnukainen, J. R. Johnson, P. I. Tarr and A. Vats, *J. Clin. Microbiol.*, 2008, **46**, 2800–2804.

125   K. Okada, S. Chantaroj, T. Taniguchi, Y. Suzuki, A. Roobthaisong, O. Puiprom, T. Honda and P. Sawanpanyalert, *Diagn Microbiol Infect Dis*, 2010, **66**, 135–139.

126   N. Srinivas, T. E. Ouldridge, P. Šulc, J. M. Schaeffer, B. Yurke, A. A. Louis, J. P. K. Doye and E. Winfree, *Nucleic Acids Res.*, 2013, **41**, 10641–10658.

127   K. Nagamine, T. Hase and T. Notomi, *Mol Cell Probes*, 2002, **16**, 223–229.

128   J. Jang, H. G. Hur, M. J. Sadowsky, M. N. Byappanahalli, T. Yan and S. Ishii, *J. Appl. Microbiol.*, 2017, **123**, 570–581.

129   M. T. Alam, T. A. Weppelmann, C. D. Weber, J. A. Johnson, M. H. Rashid, C. S. Birch, B. A. Brumback, V. E. M. Beau de Rochars, J. Glenn and A. Ali, *Emerg. Infect. Dis.*, 2014, **20**, 356–363.

130   K. A. Simonsen, A. L. Anderson-Berry, S. F. Delair and H. D. Davies, *Clin. Microbiol. Rev.*, 2014, **27**, 21–47.

131   P. Mukherjee, S. Ghosh, T. Ramamurthy, M. K. Bhattacharya, R. K. Nandy, Y. Takeda, G. B. Nair and A. K. Mukhopadhyay, *Jpn J Infect Dis*, 2010, **63**, 234–238.

132   H. Yang, H. Liu, H. Kang and W. Tan, *J. Am. Chem. Soc.*, 2008, **130**, 6320–6321.

133   R. Liu, Y. Huang, Y. Ma, S. Jia, M. Gao, J. Li, H. Zhang, D. Xu, M. Wu, Y. Chen, Z. Zhu and C. Yang, *ACS Appl. Mater. Interfaces*, 2015, **7**, 6982–6990.

134   A. J. Simon, L. T. Walls-Smith, M. J. Freddi, F. Y. Fong, V. Gubala and K. W. Plaxco, *ACS Nano*, 2017, **11**, 461–468.

135   X. Xiong, C. Zhou, C. Wu, G. Zhu, Z. Chen and W. Tan, *Macromol. Rapid Commun.*, 2013, **34**, 1271–1283.

136   T. R. Hoare and D. S. Kohane, *Polymer (Guildf).*, 2008, **49**, 1993–2007.

137   H. Shih and C.-C. Lin, *Biomacromolecules*, 2012, **13**, 2003–2012.

138   D. Y. Zhang and E. Winfree, *J. Am. Chem. Soc.*, 2009, **131**, 17303–17314.

139   B. D. Fairbanks, D. M. Love and C. N. Bowman, *Macromol. Chem. Phys.*, 2017, **218**, 1700073.

140   M. A. English, L. R. Soenksen, R. V Gayet, H. de Puig, N. M. Angenent-Mari, A. S. Mao, P. Q. Nguyen and J. J. Collins, *Science*, 2019, **365**, 780–785.

141   A. B. Lowe, *Polym. Chem.*, 2014, **5**, 4820–4870.

PUBLICATIONS

E Phillips,‡ T Moehling,‡ K Ejendal, O Hoilett, K Byers, LA Basing, L Jankowski, J Bennett, LK Lin, L Stanciu, J Linnes. "Microfluidic rapid and autonomous analytical device (microRAAD) to detect HIV from whole blood samples." *Lab on a Chip*. October 2019. ‡ indicates co-first authors

E Phillips, A Young, N Albarran, J Butler, K Lujan, K Hamad-Schifferli, L Gehrke, J Gomez-Marquez. "Ampli: A Construction Set for Paperfluidic Systems." *Advanced Healthcare Materials*. May 2018.

S Byrnes, E Phillips, T Huynh, B Weigl, K Nichols. "Polydisperse emulsion digital assay to enhance time to detection and extend dynamic range in bacterial cultures enabled by a statistical framework." *Analyst*. May 2018.

E Phillips, T Moehling, S Bhadra, A Ellington, J Linnes. "Strand displacement probes combined with isothermal nucleic acid amplification for instrument-free detection from complex samples." *Analytical Chemistry*. April 2018.

I Bosch, et al. "Rapid Antigen Tests for Dengue Virus Serotypes and Zika Virus in Patient Serum." *Science Translational Medicine*. September 2017.

E Phillips, R Shen, S Zhao, J Linnes. "Thermally actuated wax valves for paper-fluidic diagnostics." *Lab on a Chip*. October 2016.